Contents

1

Introduction

1.1 EMERGING FIELD OF SPINTRONICS

Spintronics is a novel multidisciplinary field that is concerned with manipulation of spin degree of freedom of electrons in solid state devices. Up to the 1980's essentially all semiconductor technology was based on charge properties of electrons and holes in devices like transistors, microchips, photodetectors etc. However the discovery of Giant Magnetoresistance (GMR) effect by M. N. Baibich, A. Fert[1] and co-workers in 1988 is usually regarded as the beginning of spintronics. GMR effect is the modulation of resistance of a multilayer structure made of magnetic and non-magnetic materials under the application of magnetic field. Sensors based on GMR have been introduced in the past five years[2], while contemporary hard disk have read heads utilizing the same effect. Furthermore, magnetic RAM (MRAM) uses magnetic hysteresis to store data and magnetoresistance to read data. Memory units in MRAM are integrated on a circuit chip and are based on GMR or pseudospin valve effect. Advantages of the MRAM compared with silicon electrically erasable programmable read-only memory (EEPROM) and flash memory are 1000 times faster write times, no wearout with write cycling, and lower consumption for writing. This means that spintronics is not a field confined to laboratories and research facilities but has found application in everyday life. More intense research in the field of spintronics began when Datta and Das[3] proposed a spin transistor in 1990. In this type of transistor the gate voltage controls the magnitude of precession of electron spins while passing through a semiconductor layer placed between two ferromagnetic con-

tacts, thus modulating the resistance seen by the electrons in transit. Typical precession frequencies of spins in semiconductor structures are of the order of a few THz. For this kind of device to gain wide commercial application an obstacle that must be overcome is the realization of reliable injection of spins into semiconductors. The control over the direction of the spins injected into a material is thus very important. It is necessary that the time needed for spins to regain equilibrium after injection is sufficiently long so that useful manipulations can be realized. However, all commercially available devices based on spin degree of freedom are made of *metallic* ferromagnets, like Fe, Co and Ni. While in existing realizations like read heads it poses no obstacle, for wider applications and integration with existing semiconductor technology, like e.g. spin field effect transistor, semiconductor ferromagnetic materials are needed. The major reason is a considerable conductivity mismatch between metallic ferromagnets and a semiconductor. Therefore it would be desirable to have (ferro)magnetic semiconductors that can be easily integrated with existing semiconductor devices. One of the first discovered magnetic semiconductors encompasses europium and chromium chalcogenides (rock-salt type: EuSe, EuO and spinels: $CdCr_2S_4$, $CdCr_2Se_4$), which have a Curie temperature below 100K. Their ferromagnetic order arises from the exchange interaction between itinerant electrons and localized magnetic spins[4] (s-f and s-d exchange interactions). Another family of magnetic semiconductors are perovskite manganites $(La,Sr)MnO_3$ and related materials which show colossal magnetoresistance (CMR) whose studies have been particularly active over the recent years. Their ferromagnetic order, starting from around 350 K, originates from the double-exchange interaction. Properties of manganites and their epitaxial heterostructures are currently studied intensively (Coey[5, 6] *et al.*). Their compatibility to the existing electronic devices is questionable due to the difference in crystal structure.

However, significant breakthrough occurred with the discovery of Dilute Magnetic Semiconductors (DMS) in which transition or rare-earth metal atoms replace a fraction of the atoms in the semiconductor host. In the 1980's, research in DMS was focused mainly on II-VI semiconductors such as (Cd,Mn)Te and (Zn,Mn)Se. In the group IV of elemental semiconductors, they occupy mainly interstitial positions, whereas in III-V semiconductors the 3d transition metal impurities usually substitute cation (III) atoms. The metastability of the zinc blende phase of the DMS (III,Mn)V compounds and low solubility of manganese in these materials were the major obstacles for synthesis of this kind of dilute magnetic semiconductors [7]. The first successful non-equilibrium growth by molecular beam epitaxy of a III-V DMS was achieved [8] in 1989 by Munekata *et al.* resulting into (In,Mn)As films on GaAs substrates. Subsequent discovery[9] of the hole-induced ferromagnetic order in p-type (In,Mn)As encouraged researchers to search for new DMS which resulted in fabrication of various (III,Mn)V materials such as: (Ga,Mn)As, (Ga,Mn)P, (Ga,Mn)N etc. Among them (Ga,Mn)As is particularly interesting because of possible application in combination with available and existing semiconductor

industry made for GaAs. First serious breakthrough was made in 1997 when a research group at the University of Tohoku, Japan achieved a Curie temperature as high as $T_C = 110$K [10, 11]. Since then various experimental groups have tried to reach much higher temperature, and currently the record value is set (Ref. [12]) at 173K achieved by the experimental group at the University of Nottingham, United Kingdom. This value of T_C is attained in a thin (25 nm) annealed sample that contained 8% of manganese atoms, see Fig.1.1. The Curie temperature was measured both from the temperature-dependence of the remnant magnetization measured by SQUID (Superconducting Quantum Interference Device) and from anomalous Hall effect.

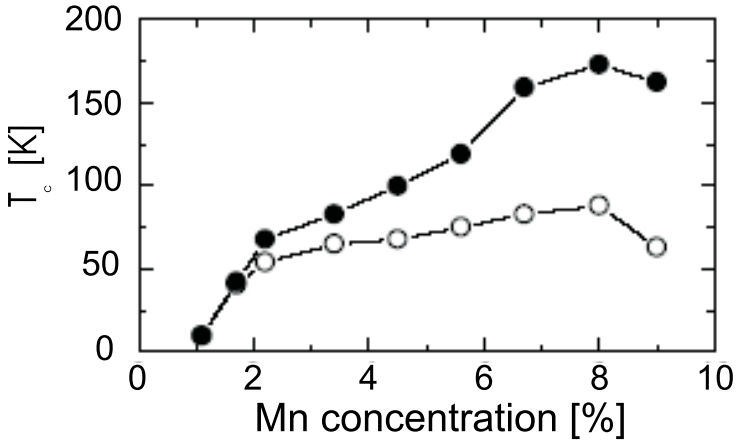

Fig. 1.1 Curie temperature as a function of manganese concentration: open circles correspond to as-grown samples, while closed for annealed samples. The highest value of $T_C = 173K$ is achieved for x(Mn)=8%. Adapted from Ref .[12].

Above room temperature ferromagnetism was observed in n-type[14] GaN, p-type[13] GaN and p-type GaP doped with Mn [15]. Manganese atoms in (Ga,Mn)As and (Ga,Mn)P act both as localized magnetic moments and as acceptors giving free holes to the alloy. Before going into more information about (Ga,Mn)As, I will present a general introduction about other DMS's, and growth of these novel materials will be given in the following sections.

1.2 II-VI DMS MATERIALS

In a II-VI semiconductor, the II element is substituted by an equivalent valence of magnetic transition metal atoms, and they provide only magnetic localized moments to the host. However, it is difficult to dope II-VI semi-

conductors, which is one of the major obstacles for the use of II-VI semiconductors as electronic materials. Another disadvantage is the dominance of antiferromagnetic superexchange among Mn spins, which yields to paramagnetic, antiferromagnetic or spin-glass order in these materials. On the other hand, in II-VI DMS, the optical characteristic such as Faraday effect are greatly modulated by magnetic fields due to the exchange interaction (sp-d interaction) between s and p orbitals of nonmagnetic atoms and the d orbitals of the magnetic atoms. This effect is notably pronounced in (Cd,Mn)Te in the case the energy of photons lies a little below the energy of free exciton. Although the effect is strongest at low temperatures, it is also significant at room temperature. (Cd,Mn)Te-based "Faraday rotators" can be used in optical telecomunications as "optical isolators" between the source of radiation (a strong laser) and the rest of the optical transmission line to avoid parasitic light reflected back to the laser and disturbing its operation. Furthermore, as a wide-gap semiconductor (Cd,Mn)Te may be used as a key ingredient in radiation detectors. Another example from the same family is (Zn,Mn)Se, which is used a spin-polarizer in heterostructures[16]. This material is non-magnetic in the absence of magnetic field while it shows a giant Zeeman splitting at low temperatures and in the presence of a magnetic field, which can reach 20 meV in the conduction band[16]. It is usually doped with Be to ensure there is enough carriers for polarization. In common experimental setups (Zn,Mn)Se layers are integrated with LED diode which is used to probe the spin-polarization, since during recombination there is a transfer of angular momentum to the photons, i.e. generation of circularly polarized light.

1.3 GROWTH OF III-V DMS MATERIALS

With the advent of Molecular Beam Epitaxy (MBE), it is possible to deposite layers of single crystals of high quality. However, under equilibrium conditions, solubility of manganese atoms, is very low, 0.1% and it was a serious obstacle to fabricate (Ga,Mn)As showing ferromagnetic order. Introduction of higher content of Mn results in phase separation and surface segregation. However, it is possible to produce (Ga,Mn)As with higher Mn concentration by performing MBE at lower temperatures, thus far from equilibrium. The phase diagram describing the relation between the major growth parameter - substrate temperature and Mn concentration and the chemical/physical properties of the material is shown in Fig.1.2. It can be seen that metallic (Ga,Mn)As having high hole concentration can be grown within a relatively small window in the diagram. For instance, if the growth temperature is too low, the roughening of the material takes place or even the layer become polycrystalline. Unfortunately, non-equilibrium growth produces inevitable defects such as As antisites and Mn interstitials that deteriorate both electronic and magnetic properties of (Ga,Mn)As.

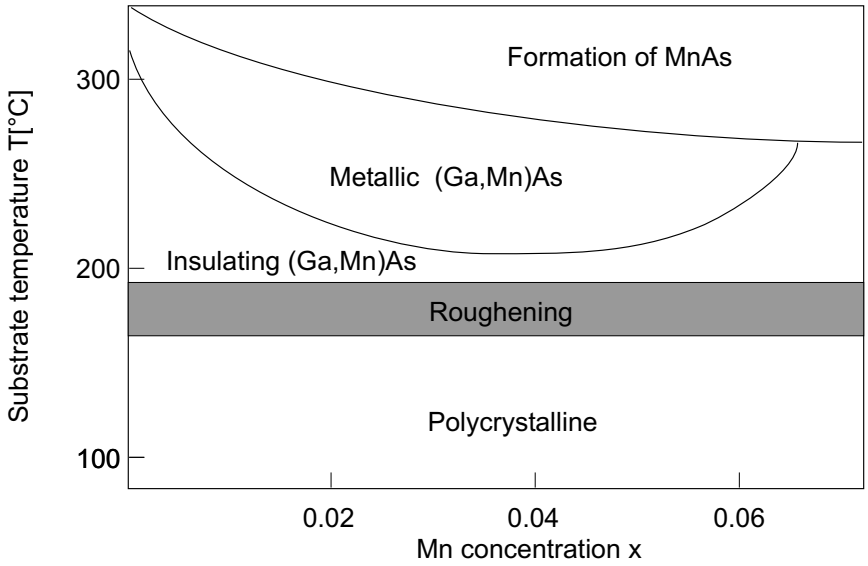

Fig. 1.2 Phase diagram of (Ga,Mn)As a function of substrate temperature and molar concentration of Mn (taken from Ref.[11])

1.3.1 Defects in (Ga,Mn)As

Common defects in crystal structure of (Ga,Mn)As grown by low temperature MBE are: As antisites and Mn interstitials. Both of them act as double donors and compensate two substitutional Mn_{Ga} acceptors, and as a result as-grown samples usually have hole density around 30% of manganese volume concentration at most. As antisites (As_{Ga}) are defects when an As occupies a Ga site. These defects are also present in GaAs grown by LT MBE, and were known before the advent of (Ga,Mn)As. The reason is low surface mobility of As_2 or As_4 molecules and reduced As desorption rate at low T_S. With the increase of the growth temperature the concentration $x_A(As_{Ga})$ rapidly decreases, for instance $x_A \approx 0.004$ at $T_S = 200°C$, and $x_A \approx 0.0003$ at $T_S = 260°C$ (x_A is given relative to the Ga concentration). On the other hand, these antisites increase the lattice constants as As atomic radius is larger than that of gallium. For instance, Mašek *et al.* [17] found, using density-functional calculation, the following relation $a(x) = a_0 + 0.69x_A[Å]$. The presence of As antisites and as well as Mn interstitials can, in part, be removed by post-growth annealing, i.e. by subjecting the (Ga,Mn)As to heat treatment (at $T_A > 350°C$). This is the subject of the next subsection. The second major defects are interstitial Mn_I. Their presence was determined using channeling Rutherford backscattering (RBS)[18]. It is estimated that their concentration can be as high as 15% of the total Mn, thus making them more important than

As_{Ga}. For instance, Mathieu has found the following empirical relation for the relative increase of the lattice constant $\delta a_{rel} = 0.4x_{I}$[Å]. Furthermore, the presence of Mn_{I} not only deteriorates the conductivity but also reduces the saturation magnetization and the Curie temperature. This is due to the fact that Mn_{I} are antiferromagnetically coupled to adjacent Mn_{Ga}, while isolated Mn_{I} have no contribution to the ferromagnetic state.

1.3.2 Annealing

Annealing is a post-growth procedure to improve the quality of a crystal by subjecting it to a heat-treatment. The first annealing procedure on (Ga,Mn)As was performed in 1997 by Van Esch[19], but the temperature was too high (above 350°C) which resulted in deterioration of the crystal. However, Hayashi[7] *et al.* achieved an improvement of both the conductivity σ and the Curie temperature T_C of (Ga,Mn)As samples when they were subjected by a post-growth heating for an hour closer to the growth temperature ($T_a = 260$°C). Even higher Curie temperature were obtained for longer annealing times[12, 20] (several hours) and lower temperatures[12] around 190°C. It was reported by many research groups that annealing removes point defects, As antisites and reduces the concentration of Mn_{I} that results into higher hole density by almost one order of magnitude and increases the saturation magnetization.

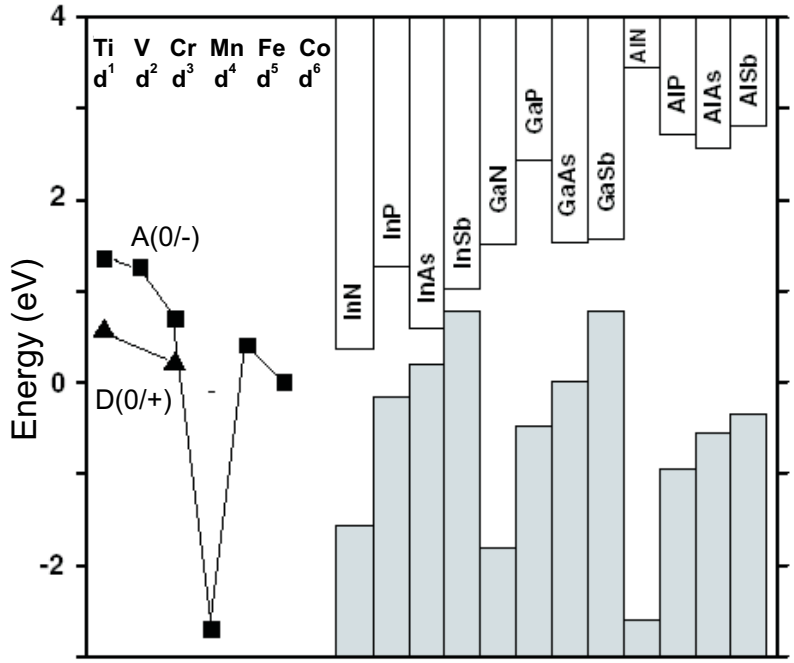

Fig. 1.3 Position of Mn acceptor/donor level in III-V materials (taken from Ref.[22]). Shaded bars represent the top of valence bands.

1.4 ELECTRONIC STRUCTURE OF MANGANESE ACCEPTOR IN DMS

A neutral manganese atom has the electronic structure $4s^2 3d^5$ in the outer shell, where spins of all 5 electrons in the d-shell are aligned according to Hund's rules. When introduced in III-V DMS it usually acts as an acceptor. According to the internal reference rule[21], the position of the acceptor level with respect to vacuum level do not vary across the entire family of the II-VI or III-V compounds. This also pertains to other transition metal impurities like Ti, V, Fe, Cr, etc. and the data for several impurities in II-VI and III-V DMS are presented on Fig. 1.3 (adapted from Ref.[22]). The symbols D(0/+) and A(0/-) denote the donor and acceptor levels derived from 3d shells of magnetic ions. In the case of II-VI DMS (left panel), these states correspond to the transformation of the doubly ionized magnetic ions Mn^{2+} into Mn^{3+} and into Mn^{1+} ions, in their ground states, respectively, that is to the lower and upper Hubbard bands. Similarly, in the case of III-V DMS (right panel) D(0/+) and A(0/-) denote the donor and acceptor states which, however,

in contrast to the situation in II-VI DMS, correspond to the transformation of the triply ionised magnetic ions Mn^{3+} into Mn^{4+} and into Mn^{2+} ions, respectively.

As can be seen from the figure the d level of Mn in III-V is relatively deep indicating high stability of Mn(d^5). This level gives rise to an acceptor level in the band gap through interaction with valence holes as it will be explained in the next chapter. The five electrons on the d shell retain their high-spin state even when Mn substitutes the cation Ga in these materials, thus forming localized moments of $S = 5/2$, with zero total angular momentum $L = 0$. On the other hand, the manganese atom has only two electrons (instead of three) in the s shell, so that the creation of a hole is expected. However due to teh presence of the half-filled d shell the electronic structure is not trivial, and theoretically there are three possible configurations: $A^0(d^4)$, $A^0(d^5 + h)$ and $A^-(d^5)$ (h denotes a hole). Notation A^0 corresponds to the neutral state of Mn with respect to the GaAs host environment, i.e Mn^{3+}, and this state has not observed experimentally. The state $A^0(d^5 + h)$ is a state where the hole is weakly bound to the manganese atom. The early investigation of the acceptor level of Mn in GaAs, were done on bulk (Ga,Mn)As grown by the Czochralski method[25, 27]. The Mn concentration was low $10^{17-18} cm^{-3}$, and Electron Paramagnetic Resonance (EPR) revealed that Mn has $A^0(d^5 + h)$ in this kind of samples, while the acceptor level was determined to be $E_{acc} = 113meV$[27]. In recent studies on both LT-MBE (Ga,Mn)As[28, 29] and samples grown using Czochralski method[28, 29] it was confirmed that Mn in GaAs can have only two configuration: $A^0(d^5+h)$ and $A^-(d^5)$, with the *absence of the neutral state*. The relatively deep acceptor level of order 100meV, indicates that a simple effective theory can not explain the electronic structure of the level. This is expected since the open d shell "behaves" non-trivially in the III-V environment, which is indicated by a peak in the density of states as revealed by first-principle studies[31] of the band structure. As far as (Ga,Mn)N is concerned the acceptor level lies even deeper[32] in the band gap $E_{acc} = 1.42eV$, so that localization of impurity wavefunction is stronger than that of in (Ga,Mn)As. More details about the nature of the Mn acceptor level are given in the first chapter of this thesis.

1.5 TRANSPORT MEASUREMENTS

Transport properties of DMS materials and particularly $Ga_{1-x}Mn_xAs$ are highly sensitive on the Mn concentration, growth temperature and post-growth treatment. This is due to the presence of defects As_{Ga} and Mn_I that act like scattering centers, that substantially reduce the mean-free path of the holes. Early investigation[19] of magnetotransport properties of $Ga_{1-x}Mn_xAs$ show that samples with $x(Mn) > 1.5\%$ show metallic type resistivity i.e. decrease of resistivity with T approaching zero. In figure Fig.1.4 are shown more

recent experimental data of the resistivity as a function of temperature. As can be seen, all curves have similiar shape with a pronounced cusp near T_C

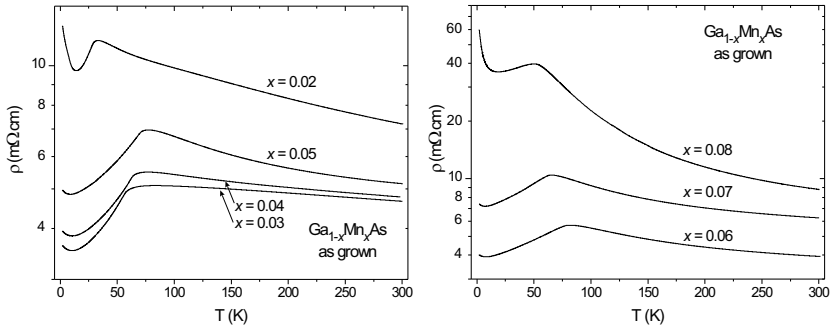

Fig. 1.4 Resistivity ρ as a function of temperature T of as-grown $Ga_{1-x}Mn_xAs$ films of thickness $d = 40nm$. (Taken from Ref. [26])

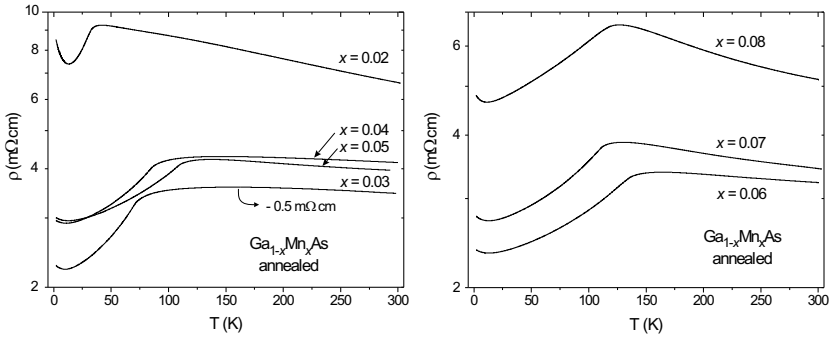

Fig. 1.5 Resistivity ρ as a function of temperature T of $Ga_{1-x}Mn_xAs$ films after a post-growth annealing. Left panel: $0.02 < x < 0.05$, right panel: $0.06 < x < 0.08$. (Taken from Ref. [26])

1.6 SPIN POLARIZATION AND SPIN-INJECTION

The first measurements and investigation[23] of spin-polarized transport date back to the sixties when anomalous transport phenomena in Eu-chalcogenide alloys were observed by Kasuya[24], and the seventies when Tedrow and Meservey[36, 37] measured tunneling current through Al(superconducting)/Al_2O_3/Ni heterostructure. Afterwards, Julliere measured tunneling conductance of F/I/F junctions in 1975, where the insulator was amorphous Ge. Following the anal-

ysis of conductance done by Tedrow and Meservey[36, 37], Julliere developed a model for the change of the conductance between the parallel and antiparallel orientation of magnetization in the two ferromagnetic regions FM1 and FM2 (See Fig.1.6).

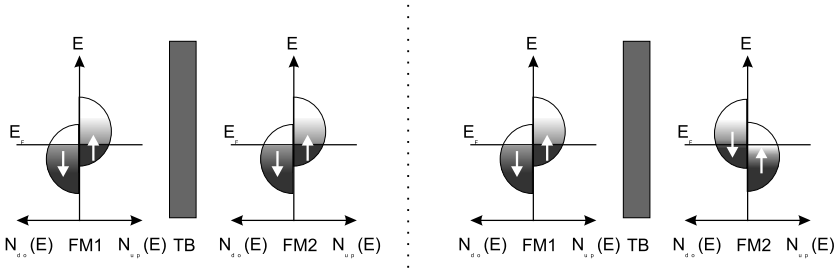

Fig. 1.6 Spin-dependant tunneling between two ferromagnetic metals for the two orientations of the magnetization. The difference in density of states for opposite orientation causes the change in resistivity.

If the magnetizations of the two ferromagnets are orientied parallel to each other then majority (minority) spin can tunnel to majority (minority) spin-subband. On the other hand if the two ferromagnets are oriented in the opposite direction majority spin electrons tunnel harder since there are less avaliable states in the another ferromagnet. Both situations are depicted on Fig.1.6. Thus one can expect different resistivity for the two cases, and Julliere observed 14% change in the resistivity for electron tunneling between Fe and Co separated by a Ge barrier. Furthermore, he derived a simple formula for the change of conductivity which depends only on the polarization and not on the barrier thickness:

$$\frac{\Delta R}{R} = \frac{2\Pi_1\Pi_2}{1+\Pi_1\Pi_2}, \Pi = \frac{N_{up}(E_F) - N_{do}(E_F)}{N_{up}(E_F) + N_{do}(E_F)} \tag{1.1}$$

Serious breakthrough happened when Baibich, A. Fert and co-workers at the University of Paris-Sud observed magnetoresistance of Fe/Cr superlattices asa high as 50%. The superlattices was grown using molecular beam epitaxy (MBE), and the effect is pronounced at low temperatures ($T = 4.2K$) which makes this material not useful for practical applications. Later on, Parkin and co-workers at IBM Almaden Research center tried numerous combinations of metals, and thicknesses of layers but now using sputtering method to grow superlattices in order to make a reliable sensor of magnetic field at room temperatures. Finally, after a year of research they achieved modest ratio of magnetoresistance of $2-3\%$ in Co/Ru and Co/Cr metallic superlattices. On the other hand, in the past five years there has been a growing interest in the generation of spin coherent transport and spin-injection from one (ferromagnetic) semiconductor to another one. In earlier experiments[39,

40] spin-polarized electrons were optically generated in n-type GaAs, and the decoherence time was found to be 100ns. Later on, the research continued on spin transfer across GaAs/ZnSe heterojunction where GaAs acts as a spin-resorvoir[42]. Approximately 10% of the electrons move across the interface due to built-in bias, but once they are in ZnSe the electrons begin to precess in opposite direction and decay at a rate characteristic for ZnSe. This kind of spin-injection is referred as a burst mode (see Fig.1.7. However, the spin transfer efficiency was a few percent, but using the electric field to drag[43, 44] electrons the efficiency can be enhanced by a factor of 40.

1.7 MAGNETIC INTERACTIONS

Transition metal impurities like Mn, Fe, Co have unfilled valence d shell, which is responsible for the magnetic interactions. As already mention the valence

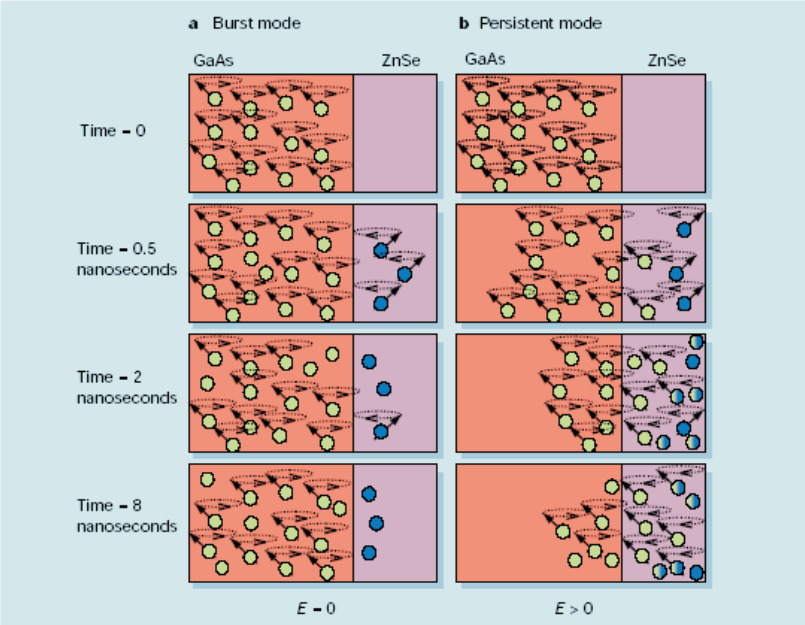

Fig. 1.7 Transfer of spin polarized electrons across GaAs/ZnSe heterojunction: a) Burst mode. Electron move due to built-in bias, but the efficiency of transfer is only 10%. The electron begin to precess at a rate typical for ZnSe (denoted by darker color) b) Persistent mode Upon application of an external electric field the efficiency is enhanced, and the spins that have just crossed the interface retain their information about the spin precession in the reservoir.

state of Mn in GaAs is Mn^{2+} and the d-shell is half-filled d^5. According to Hund's rule all five electrons are alligned parallel in order to minimize the Coulomb repulsion. These electrons give rise to ferro- or para- magnetism when in materials like GaAs or ZnSe. However, the type of magnetism and the magnitude of the critical temperature depends on the way how electrons on neighbouring Mn ions interact. There are several types of magnetic exchange

- *Direct exchange* is present when there is a direct overlap between the wave-functions of electrons locating on neighbouring Mn ions.
- *Superexchange* is an indirect exchange mechanism, in which the magnetic ions interact through overlap of the wavefunction with the same intermediate non-magnetic ion.
- *Indirect exchange* the interaction among magnetic ions is mediated by conduction or valence electrons in the host material.

1.7.1 Hole mediated ferromagnetism

Based on various experimental data it is believed that ferromagnetism in III-V DMS materials is hole mediated. For instance, the post-growth annealing enlarges the hole density p_h that enhances the Curie temperature T_C. Thus at fixed manganese concentration x, one can investigate the hole dependence of the Curie temperature T_C. The hole density can be changed by co-doping with another material such as Sn which leads to compensation of holes, i.e. the reduction of p_h. It is observed[48] that (Ga,Mn)As:Sn have a smaller T_C than "pure" (Ga,Mn)As. Furthermore, carbon co-doping[49] of (Ga,Mn)P:C leads also to the enhancement of the transition temperature T_C up to 270K, close to room temperature. On the other hand, recent theoretical studies[54] suggest also that T_C of (Ga,Mn)As can be raised using carbon co-doping. All these facts indicate that ferromagnetism in III-V DMS materials is hole mediated.

1.8 THEORETICAL MODELS

All proposed models of ferromagnetism in (Ga,Mn)As can be classified into two major groups: *ab initio* or first principle studies, and (semi)-phenomenological models that start from an effective Hamiltonian that incorporates the principal features of the material. First principle studies are based on heavy computer calculations since they start from the electronic properties of constituent atoms, and e.g. the band-structure is obtained. (Semi)phenomenological models are more interesting since the underlying physics is more transparent and open for further investigation since the starting Hamiltonian usually takes into account only interaction between two (neighbouring) impurities,

or one impurity and the environment. Sometimes the strength of this interaction is extracted from first principle calculations. Within this group one can single out phenomenological models based on mean field approaches, and models that start from microscopic Hamiltonian like RKKY exchange[10, 50], kinematic exchange[51], mean field Zener model[52], models based on Heisenberg[53] type of interaction etc. One of the first proposed model for ferromagnetism in III-V DMS was Ruderman-Kittel-Kasuya-Yosida model[10]. It is based on the long-range indirect exchange interaction that was developed to explain the ferromagnetism in rare-earth metals, where there is no direct overlap among the magnetic electrons.

1.8.1 RKKY interaction

The RKKY interaction was originally developed by M.A. Ruderman and Charles Kittel in the 1950's as a way to describe unusually broad nuclear spin resonance lines that had been observed in natural metallic silver. The initial model was based on second-order perturbation theory to describe an indirect exchange where the nuclear spin of one atom interacts with a conduction electron via the hyperfine interaction, and this conduction electron then interacts with another nuclear spin thus creating a correlation between the two nuclear spins. Later the model was extended by Kasuya and Yosida to explain ferromagnetism in rare-earth metals. When a magnetic impurity is placed in a metal, the free electrons tend to align their spin in such a way to screen the spin of the impurity. The polarization of the free electrons around the impurity has an oscillatory behavour similar to Friedel oscillations when a charged impurity is screened. The spin polarization of conduction electrons governs the indirect interaction of two neighbouring atoms which is characterized by the coefficient $J_{RKKY}(r_{ij})$ that appears in a simple effective Hamiltonian:

$$H = \sum_{ij} J_{RKKY}(r_{ij}) \mathbf{J}_i \cdot \mathbf{J}_j \tag{1.2}$$

The coupling strength $J_{RKKY}(r_{ij})$ depends crucially on the Bloch wavevector at the Fermi energy, i.e. Fermi wavevector k_F, and its form is

$$J_{RKKY}(r_{ij}) = \frac{2mk_F^4}{\pi h^2} J_{ex}^2 F(2k_F r_{ij}) \tag{1.3}$$

Here J_{ex} is the exchange coupling between the itenirant electrons and magnetic atom, and the function $F(x)$ is oscillatory whose expression is given by

$$F(x) = \frac{x\cos(x) - \sin(x)}{x^4} \tag{1.4}$$

The RKKY interaction as a mechanism to describe ferromagnetism in (Ga,Mn)As was first proposed by Matsukura *et al.*[10]. However, a further investigation by many authors[51, 55] revealed that this mechanism is not reliable for diluted magnetic semiconductors since the distance between the carriers is larger

than the average distance between two magnetic impurities. This is due to the self-compensation by Mn_I and As_{Ga} that makes the concentration of holes significantly smaller than Mn density as explained earlier.

1.8.2 Heisenberg model

Starting point of this model is the effective Hamiltonian proposed by Heisenberg[56]:

$$H = \sum_{i,j} J(r_{ij}) \mathbf{S}_i \cdot \mathbf{S}_j \tag{1.5}$$

The indices i, j run over the (random) positions of the magnetic atoms, Mn. The value of the exchange coupling constant $J(r_{ij})$ is either extracted from first principle studies[53], or from some band theory[59]. Some authors[59] assume that $J_(r_{ij})$ has a Gaussian shape:

$$J(r_{ij}) = \frac{J_{pd}}{(2\pi a_0^2)^{3/2}} e^{-\frac{r^2}{2a_0^2}} . \tag{1.6}$$

The Curie temperature is then usually evaluated through a mean-field approximation in the following manner: first one concentrates on a particular magnetic atom i and estimate the "effective field" $\mathbf{H_{eff}}$ (not to be confused with Hamiltonian H) it experiences

$$\mathbf{H_{eff}} = \frac{1}{g\mu_B} \sum_{i' \neq i} J_{ii'} \mathbf{S}_{i'} \tag{1.7}$$

where g is the gyroscopic ratio and μ_B is the Bohr magneton. In general, $\mathbf{H_{meff}}$ depends on the detailed configuration of all other spins at other sites. The idea of mean-field theory is to replace $\mathbf{H_{meff}}$ with its thermal equilibrium mean value, which can be estimated from the magnetization $\mathbf{M}$. Furthermore it is assumed that manganese (or other magnetic) atoms are placed uniformly, i.e. the *virtual crystal approximation* (VCA) is adopted. Thus the average value of the spin is

$$\langle \mathbf{S}_i \rangle = n \frac{\mathbf{M}}{g\mu_B} , \tag{1.8}$$

where n is the volume concentration of magnetic atoms. Thus one can define constant of proportionality, say λ, between the effective field and magnetization $\mathbf{M}$ $\mathbf{H_{meff}} = \lambda \mathbf{M}$. On the other hand, the value of magnetization M is some function[60] of the ratio of H_{meff}/T

$$M = M_0 \left(\frac{H_{eff}}{T} \right) = M_0 \left(\frac{\lambda M}{T} \right) . \tag{1.9}$$

Here M_0 stands for the magnetization in the absence of magnetic interactions, i.e. it is expressed by the Brilloiun function $B_S(x)$:

$$M_0 = ng\mu_B S B_S(g\mu_B SH/(k_B T)) , \tag{1.10}$$

and

$$B_S(x) = \frac{2S+1}{2S} coth\, \frac{2S+1}{2S} - \frac{1}{2S} coth\, \frac{1}{2S}\,. \tag{1.11}$$

The equation Eq.(1.8.2)can be written as a pair of equations: $M(T) = M_0(x)$ $M(T) = T \cdot x/\lambda$, which has a solution if the slope of the straight line is less than the slope of $M_0(x)$ at the origin M_0'. Therefore, by differentiating Eq. (1.8.2) one finally arrives at the expression for the Curie temperature

$$k_B T_C = \frac{S(S+1)}{3} \sum_{i' \neq i} J_{ii'}\,. \tag{1.12}$$

Above only the simple Heisenberg model was shown, within the virtual crystal approximation. This treatment is rather rough and usually yields an overestimation of the transitional temperature. To overcome this the authors of Ref. [53, 57] used a Green's function method to extend the model to materials without translational symmetry. This approach treats the positional disorder in the spin system numerically exactly except that a uniform magnetization is assumed. The influence of magnons, i.e. of low-energy quantum excitations was also included. In order to make the theory more plausible the exchange constant J_{ij} is obtained from first principle studies. The predictions of T_C in Ref.[53] is in good agreement with experiment.

1.8.3 Mean-field theories

The main ideas of the mean field (MF) approach has already been given in the last subsection. Here, the extension of the mean field approach will be briefly presented as developed by Jungwirth, Konig, McDonald and other authors[61–63]. It is well known that simple MF theory usually overestimates the Curie temperatures, since it neglects correlations effects, disorders etc. By noting that the derivative of the magnetization with respect to H_m is actually the susceptibility χ_f, the expression for T_C as given in Eq. (1.8.2) can be rewritten as

$$k_B T_C = \frac{nS(S+1)}{3} \frac{J_{pd}^2 \chi_f}{(g\mu_B)^2}\,. \tag{1.13}$$

This kind of form is convenient since we can single out the contribution of the kinetic (χ_f) and exchange energy (χ_{ex}) to the susceptibility, which in the single band approximation has the form

$$\chi_f = (g\mu_B)^2 \frac{m^* k_F}{4\pi^2\hbar^2}, \qquad \chi_{ex} = (g\mu_B)^2 \frac{e^2 m^{*2}}{16\pi^4\hbar^4\epsilon} \tag{1.14}$$

In realistic calculation, one should take into account more precise details about the band structure, for instance by employing 6×6 $\mathbf{k}\cdot\mathbf{p}$ theory[62]. One of the successes of the mean field theories is the prediction of the dependance of T_C

on the hole density p_h for small concentration of Mn, which is roughly given by $T_C \approx p_h^{1/3}$. It is usually governed by χ_f, since the exchange energy weakly depends on the hole density. However, this simple consideration leads to a huge overestimate of T_C. Only by taking into account the Mn-Mn interaction one can expect a better agreement with the experimental data.

1.8.4 Mean field Zener model

Mean field Zener model, as proposed by Dietl *et al.* [52] is one of the most accepted model for ferromagnetism in (Ga,Mn)As and related DMS materials. It is based on the Zener model[64] for ferromagnetism in transition metals like Fe, Ni, and Co. In the original model[64, 65], important parameters are obtained through minimization of the free energy that consists of three parts: direct exchange between d shells, the exchange coupling between conduction electrons and d shells and kinetic energy of the conduction electrons. The contribution of free electrons to entropy is considered to be negligible so that their concentration is varied as to minimize the free energy F. In order to take into account the complicated nature of Mn acceptor state in (Ga,Mn)As, Dietl and co-workers developed a "two-fluid model" of holes that consists of free holes, and weakly bound holes as there are two possible states Mn(d^5) and Mn(d^5+h). Their contribution to the free energy F was computed within the six band Luttinger-Kohn model (i.e. $\mathbf{k}\cdot\mathbf{p}$ theory). Now the free energy is treated as a Ginzburg-Landau like functional of the magnetization $F[M(r)]$, and the equilibrium magnetization and the Curie temperature are obtained by minimizing F with respect to the magnetization M. It is assumed that both localized spins and holes are distributed randomly i.e. virtual crystal approximation is adopted. It turns out that T_C is proportional to the thermodynamic spin density of states ρ_s , which, in turn, is proportional to the spin susceptibility of the carrier liquid, χ_s. A simplification of the calculation leads to $T_C \propto x p_h^{1/3}$ which is similar to the result obtained by conventional mean field theory. The prediction of the theory is that the transition temperature of (Ga,Mn)As can reach room temperature if $x = 0.1$ under condition that there is no self-compensation.

2

Origin of ferromagnetism in III-V DMS

2.1 INTRODUCTION

Although ferromagnetic order in III-V materials was first observed in (In,Mn)As as early as in 1992, there is no clear consensus over the origin of ferromagnetism in III-V DMS up to the present day. The list of proposed models in the literature is rather long, and encompasses phenomenological, semi-phenomenological and microscopic approaches. In this thesis a microscopic model is proposed based on the Anderson model for two magnetic impurities in metals, but modified to the case of DMS. It will be shown that the presence of a band-gap, in combination with impurity states introduce new interesting features in the model. It is well known that the transition metal (TM) ions may introduce deep impurity levels in the forbidden energy gap. Among them the manganese impurity in GaAs and some other semiconductors exhibit peculiar features. According to its position in the series of the TM elements, a neutral impurity Mn^{3+} at the Ga-site is expected to have the $3d^4$ configuration. However, the Mn ion retains its fifth electron in its $3d$ shell, because of an exceptional stability of the high-spin half-filled $3d^5$ state resulting from the strong intra-atomic Hund interaction. The manganese impurities not only introduce magnetic moments in the p-type (III,Mn)V compounds but also give holes to the compound, i.e. act as acceptors. Therefore, the neutral substitution impurity state is $A^0(3d^5 + h)$, where h stands for the loosely bound hole, and the manganese provides both holes and magnetic moments to the host, A is the spectroscopic notation indicating the irreducible representation describing this state (more about these notations can be found in Ref. [66]).

Existence of the complex Mn($d^5 + h$) in lightly doped bulk GaAs is detected by electron spin resonance measurements [67] and by infrared spectroscopy [68]. These studies discovered an acceptor level inside the energy gap around 110 meV above the top of the valence band. This value is substantially higher than 30 meV resulting from conventional effective mass theory[67], which already implies that treatment of the manganese impurities in III-V compounds requires a more refined theory. On the other hand, the presence of ionized complexes $A^-(3d^5)$ is detected in (Ga,Mn)As epilayers grown by low temperature molecular beam epitaxy[69], which indicates that both mobile and localized holes exist in ferromagnetic (Ga,Mn)As. The coexistence of weakly and strongly localized states is also in accordance with AC conductivity experiments [70].

2.2 INDIRECT EXCHANGE INTERACTION BETWEEN TWO MAGNETIC IMPURITIES

According to the general principles of the theory of isolated TM in semiconductors, [66, 71] the electronic spectrum of these impurities in III-V semiconductors is predetermined by the structure of chemical bonds (hybridization) between the $3d$-orbitals of impurity ions and the p-orbitals of the valence band electrons, whereas their magnetic state is governed by the Coulomb and exchange interactions within the $3d$-atomic shell (intra-atomic electron-electron correlations), modified by hybridization with the electron states of the crystalline environment.

The localized TM impurity d-states possess t_2 and e symmetry of the crystal point symmetry group T_d as revealed in the theoretical studies of electronic properties of isolated TM impurities in semiconductors carried out in the 70's and 80's (see, e.g. Refs. [72, 74–77]). The e states are practically nonbonding d-states of an impurity $3d$ shell, whereas the t_2 states form bonding and antibonding configurations with the p-states of the valence band. The two latter types of states are classified as the crystal field resonances (CFR), in which the d-component dominates, and the dangling bond hybrids (DBH) with predominantly p-type contribution of the valence band states. Crucially important is that the absolute positions of CFR levels are relatively weakly dependent on the band structure of the host semiconductor material. The CFR levels are pinned mainly to the vacuum energy, and this pinning is modulated by the counterbalanced interactions with valence and conduction band states[66, 78]. The DBH states are more intimately connected with the peak in the density of states of the heavy hole (hh) band, which dominates the pd-hybridization. The variety of electronic and magnetic properties of Mn and other TM ions in different III-V host semiconductors stems from these universal chemical trends.

Due to a large mismatch between positions of the valence bands in GaAs, GaP on the one side and in GaN on the other side, the Mn(d^5/d^4) CFR level falls deep in the valence band in GaAs, GaP and appears within the forbidden energy gap of GaN. The CFR nature of Mn (d^5/d^4) t_2-level near the middle of the gap for (Ga,Mn)N is confirmed experimentally[32] and follows also from numerical calculations[79]. This t_2-level is *empty* in the neutral state $Mn^{3+}(d^4)$ of the substitution impurity. It becomes magnetically active only in n doped materials, e.g. in (Ga,Mn)N, where part of the Mn impurities capture donor electrons and transform into charged ions $Mn^{2+}(d^5)$. A similar behavior[66, 71, 74] is characteristic of all other light TM ions in all III-V compounds including GaAs and GaP.

Since the position of the valence band in GaAs and GaP is substantially higher in the absolute energy scale (with the vacuum energy as the reference point) than those in GaN, the CFR t_2 level (d^5/d^4) in the (Ga,Mn)As and (Ga,Mn)P DMS's falls below the center of gravity of the valence band. Therefore, this CFR level is always occupied, Mn ions retain their fifth electron in the $3d$-shell, and the neutral substitution impurity state is $(3d^5 + h)$, where h is a loosely bound hole occupying the relatively shallow acceptor level in the forbidden energy gap of GaAs and GaP.

Both of the above mentioned situations may be described within the resonance scattering model of the TM impurity states in semiconductors based on the Anderson single impurity Hamiltonian, proposed originally for TM impurities in metals, [80] and later modified for semiconductors in Refs. [75, 77, 78, 81, 82]. An extension of the Anderson model to two TM impurities in metals was proposed in Ref. [83] resulting in a ferromagnetic coupling in TM doped metals. Here we discuss a model describing interaction between Mn (and other TM) impurities in a semiconductor host. In accordance with Hund's rule for the electron occupation in Mn ions in a tetrahedral environment, [66, 71, 84] two competing states Mn(d^4) and Mn(d^5), involved in the double exchange in DMS, have the $d^4(e^2t^2)$ and $d^5(e^2t^3)$ configuration, respectively. The next charged state $d^6(e^3t^3)$ has a much higher energy due to the strong intra-ionic Anderson-Hubbard repulsion. Therefore, the 'passive' nonbonding e-electrons may be excluded from our consideration. The indirect exchange between magnetic moments is mediated by virtual transitions of t_2 electrons into unoccupied valence band states.

The Hamiltonian of two TM impurities in a III-V semiconductor has the form:

$$H = H_h + H_d + H_{hd}, \tag{2.1}$$

where the term that corresponds to holes

$$H_h = \sum_{\mathbf{p},\sigma} \varepsilon^h_{\mathbf{p}} c^\dagger_{\mathbf{p}h\sigma} c_{\mathbf{p}h\sigma} \tag{2.2}$$

includes only the heavy hole band (*hh)*. Here $c^\dagger_{\mathbf{p}h\sigma}(c_{\mathbf{p}h\sigma})$ is the creation (annihilation) operator of a hole with momentum $\mathbf{p}$ and spin orientation σ in

the hh band of the semiconductor with energy dispersion $\varepsilon^h_{\mathbf{p}}$. The heavy hole band gives the dominant contribution to the formation of the impurity states, [66, 71] and governs the onset of ferromagnetic order. The second term in the Hamiltonian (2.1) describes the electrons within the Mn atoms with a possible account of the crystal field of the surrounding atoms. In principle, we have to write down a multielectron Hamiltonian describing the degenerate states of the d shell, and including Coulomb and exchange interactions. However, as we show below it is usually sufficient to consider the non-degenerate version of this Hamiltonian

$$H_d = \sum_{i\sigma} \left(E_d \hat{n}_i^\sigma + \frac{U}{2} \hat{n}_{i\sigma} \hat{n}_{i-\sigma} \right), \tag{2.3}$$

which simplifies the calculation considerably. Here E_d is the atomic energy level of the localized Mn t_2-electrons and U is the Anderson-Hubbard repulsive parameter; $\hat{n}_i^\sigma = d^\dagger_{i\sigma} d_{i\sigma}$ is the occupation operator for the manganese t_2 - electrons on the impurities, labeled $i = 1, 2$ in (III,Mn)V DMS. The situation when the degeneracy of the t_2 states is important and the exchange interaction in the multielectron atom starts playing an essential part will be outlined and the appropriate corrections will be introduced, when necessary.

The last term in Eq. (2.1) describes the scattering of the hh electrons by the impurities

$$H_{hd} = H^{(r)}_{hd} + H^{(p)}_{hd}, \tag{2.4}$$

$$\begin{aligned} H^{(r)}_{hd} &= \sum_{\mathbf{p},\ \sigma,j} \left(V_{\mathbf{p}d} c^\dagger_{\mathbf{p}h\sigma} d_{i\sigma} e^{i\frac{\mathbf{p}}{\hbar}\mathbf{R}_j} + h.c. \right), \\ H^{(p)}_{hd} &= \sum_{\mathbf{p}\mathbf{p}',\ \sigma,j} W_{\mathbf{p}\mathbf{p}'} c^\dagger_{\mathbf{p}h\sigma} c_{\mathbf{p}'h\sigma} e^{i\frac{\mathbf{p}-\mathbf{p}'}{\hbar}\mathbf{R}_j}. \end{aligned}$$

Here $V_{\mathbf{p}d}$ is the p-d hybridization matrix element, and $W_{\mathbf{p}\mathbf{p}'}$ is the scattering matrix element due to the difference of the pseudopotentials of the host and the substituted atoms. The direct overlaps between the d-electron wave functions of the neighboring impurities in the DMS and the Coulomb interaction between them are neglected.

As mentioned above, the orbital degeneracy of the t_2 states is not taken into account in this simplified model. In reality, the orbital quantum numbers are important at least in three respects. First, the half-filled d^5 subshell of Mn is occupied by e and t_2 electrons with parallel spins in accordance with Hund's rule[73], so the sixth electron can be captured in the d^6 configuration only with the opposite spin. The energy cost of this capture is $\sim U + J$, where $J \ll U$ is the exchange energy. This feature of the impurity is preserved in the above simplified Hamiltonian: (2.3) the reaction $d^5 + e \to d^6$ is changed into $d^1 + e \to d^2$, with the spin of the second electron opposite to the first one.

The energy cost of this reaction is U, and the principal features of the ion, important for the formation of the localized magnetic moment, are practically the same as in the original atom.

Second, it is Hund's rule that requires that the total angular moments of the Mn atoms be parallel to allow the indirect inter-impurity interaction between the high-spin d^5 states via the hh valence band states. We will take Hund's rule explicitly into account, when calculating T_C, and it will be shown below, that the energy gain due to this indirect interaction, carried out by hybridization, leads eventually to the ferromagnetic ordering in DMS's.

Third, the three-fold degeneracy of t_2 electrons is also manifested in the statistics of the localized states, and therefore it influences the position of the Fermi energy in the energy gap. These statistics are described in the Appendix. The degeneracy introduces also numerical factors in the effective exchange constants. These factors are also calculated in the Appendix.

Having all this in mind, we proceed with the derivation of the indirect inter-impurity exchange within the framework of the non-degenerate Alexander-Anderson model, whereas the corresponding corrections for the real orbital structure of the Mn ion will be made when necessary. To calculate the energy of the exchange interaction between two magnetic impurities, one should find the electronic spectrum of the semiconductor in the presence of two impurities. Each impurity perturbs the host electron spectrum within a radius r_b. Inter-impurity interaction arises, provided the distance between the impurities R_{ij} is comparable with r_b. General equations for the two-impurity states and the corresponding contribution to the exchange energy are derived in Appendix. Here we present only the final equations, which will be used in the derivation of the effective exchange coupling and the Curie temperatures for the specific DMS's.

The quantity, which we actually need here is the impurity related correction to the energy of the system, which can be evaluated if the change of the density of states due to introduction of manganese atoms, $\Delta\rho$, is known:

$$E^{magn} = \int_{-\infty}^{\infty} \epsilon \cdot \Delta\rho_{\epsilon}(\epsilon) d\epsilon \tag{2.5}$$

The problem can be solved by Green's method function[82], where the density of states is given as the imaginary part of the Green's function trace

$$\Delta\rho_{\epsilon}(\epsilon) = \frac{1}{\pi}\mathrm{Im}\Delta TrG \tag{2.6}$$

$$E^{magn} = \frac{1}{\pi}\mathrm{Im}\int_{-\infty}^{\infty} \varepsilon \cdot \mathrm{Tr}\Delta G[\varepsilon - i\delta\mathrm{sign}(\varepsilon - E_F)]d\varepsilon - \sum_i U n_{di\uparrow} n_{di\downarrow}, \tag{2.7}$$

where E_F is the Fermi energy and $\Delta\mathsf{G} = \mathsf{G}(\varepsilon) - \mathsf{g}^0(\varepsilon)$ is the two impurity correction to the total one-particle Green function $\mathsf{G}(\varepsilon) = (\varepsilon - \mathsf{H})^{-1}$. The

last term is necessary because the Hubbard interaction is summed twice in the integral.

Here G is defined as a matrix in (h,d) space, and g^0 is the same matrix in the absence of impurity scattering, see Eq. (6.6). The Green function is calculated in the self-consistent Hartree-Fock approximation for the inter-impurity electron-electron repulsion U, which is sufficient for a description of magnetic correlations in TM impurities in semiconductors. This solution is described in the Appendix. Then the part of the two-impurity energy (2.7) responsible for the inter-impurity magnetic interaction may be found (see Eqs. (6.16) and (6.17)). As shown in Refs. [77, 81], resonance scattering alone may result in the creation of CFR and DBH levels split off from the valence band, provided the scattering potential is comparable with the bandwidth. However, in the case of shallow DBH states potential scattering is dominant in their formation. Like in the well-known Koster-Slater impurity model, the potential scattering in our model is described by a short-range momentum independent coupling constant, $W_{\mathbf{pp}'} \approx W$, and the same approximation is adopted for the resonance scattering parameter, $V_{\mathbf{p}d} \approx V$.

Then (2.7) acquires the compact form

$$\Delta E = -\frac{1}{\pi}\mathrm{Im}\int_{\varepsilon_{hb}}^{\varepsilon_F} d\varepsilon\,[\ln \mathsf{R}^\sigma(\varepsilon) + \ln \mathsf{Q}^\sigma(\varepsilon)] + E_{loc}(\varepsilon < \mu). \qquad (2.8)$$

Here the first term (R) in the r.h.s. describes the band contribution to the exchange energy, and the integration is carried out from the bottom of the hh band (E_{hb}) to the Fermi level (E_F). In this integral the kinetic energy gain of the band electrons due to scattering with the ferromagnetically aligned impurities is incorporated. The contributions of resonance and potential scattering are given by the first and second term in this integral, respectively. The last term ΔE_{loc} is the contribution of the occupied localized CFR and/or DBH states. These states are described by zeros of the functions $\mathsf{R}^\sigma(\varepsilon)$ and $\mathsf{Q}^\sigma(\varepsilon)$ in the discrete part of the energy spectrum (see Eqs. (6.9) and (6.7), respectively).

In all cases the energy gain results from the indirect spin-dependent inter-impurity overlap, and the mechanism of effective exchange interaction may be qualified as kinematic exchange. In general, double exchange favors a FM order, because the splitting of the energy levels belonging to two adjacent impurities occurs due to electron hopping via unoccupied band or impurity-related states *without spin reversal*. This is the consequence of the fact that $p-d$ hybridization with band holes is carried out with spin conservation. The level splitting results in an energy decrease provided that not all of the available band and impurity levels are occupied. One should note that this kinematic exchange cannot be reduced to any conventional double exchange mechanism because of an actual interplay between three contributions to the magnetic energy, namely, the scattered valence band electrons, the CFR states and the DBH states. We start with the analysis of the band contribution $\Delta E_{b,ex}$.

Since in all the cases we deal with nearly filled hh bands, it is convenient to calculate the energy in the hole representation.

By means of a simple transformation, as described in the Appendix, the leading term in the basic equation (2.8) may be transformed into

$$\Delta E_{b,ex} = \frac{1}{\pi}\mathrm{Im}\int_{\varepsilon_F}^{\varepsilon_{ht}} d\varepsilon \ln \frac{\mathsf{R}^{\sigma}(\varepsilon)}{\mathsf{R}_0^{\sigma}(\varepsilon)}, \tag{2.9}$$

where ε_{ht} stands for the top of the valence band. This equation is obtained from the more general equation (6.20) by neglecting the potential scattering in the band continuum. Then, inserting Eq. (6.9) for the matrix $\mathsf{R}^{\sigma}(\varepsilon)$ we obtain

$$\Delta E_{b,ex} = E_{b,ex} - E_{b,ex}(L_{12}=0) =$$
$$-\frac{1}{\pi}\mathrm{Im}\int_{\varepsilon_F}^{\varepsilon_{ht}} d\varepsilon \ln\left\{\frac{[g_d^{-1}(\varepsilon-i\delta)-V^2L_{11}(\varepsilon-i\delta)]^2 - V^4L_{12}^2(\varepsilon-i\delta)}{[g_d^{-1}(\varepsilon-i\delta)-V^2L_{11}(\varepsilon-i\delta)]^2}\right\}. \tag{2.10}$$

Here

$$L_{ij}(\varepsilon-i\delta) \equiv P_{ij}(\varepsilon) + \frac{i}{2}\Gamma_{ij}(\varepsilon) \tag{2.11}$$

are the standard lattice Green functions of the continuous argument ε:

$$L_{12}(\varepsilon-i\delta) = \sum_k \frac{e^{-i\mathbf{kR}}}{\varepsilon-\varepsilon_k-i\delta} = \sum_k \frac{e^{-\mathbf{kR}}}{\varepsilon-\varepsilon_k} + i\delta\pi\sum_k \delta(\varepsilon-\varepsilon_k)e^{-i\mathbf{kR}} \tag{2.12}$$

The real part of the lattice Green's function, P_{12} is evaluated by representing momentum $\mathbf{k}$ in spherical coordinates:

$$P_{12} = \sum_k \frac{e^{-i\mathbf{kR}}}{\varepsilon-\varepsilon_k} = \frac{\Omega_0}{(2\pi)^3}\int_0^{\infty}\frac{k^2dk}{\varepsilon-\varepsilon_k}\int_0^{\pi} e^{-kR\cos\nu}\sin\nu d\nu\int_0^{2\pi} d\phi$$
$$= \frac{\Omega}{(2\pi)^3}\int_0^{\infty}\frac{k^2dk}{\varepsilon-\varepsilon_k}2\pi\int_{\pi}^{0} e^{-ikR\cos\nu}d(\cos\nu) = ... = \sum_k \frac{1}{\varepsilon-\varepsilon_k}\frac{\sin(kR)}{kR} \tag{2.13}$$

where Ω_0 stands for the volume of unit cell. Now, remembering that the density of states can be written as a series of Dirac delta functions: $\rho = \sum_k \delta(\varepsilon-\varepsilon_k)$, the last line of Eq. (2.2) may be rewritten in a form suitable for numerical calculations

$$P_{12}(\varepsilon) = \int \frac{\rho(\omega)}{\varepsilon-\omega}\frac{\sin k(\omega)R}{k(\omega)R}d\omega \tag{2.14}$$

The imaginary part is evaluated in a similar fashion:

$$\Gamma_{12}(\varepsilon) = 2\pi\sum_k \delta(\varepsilon-\varepsilon_k)e^{-i\mathbf{kR}} \approx 2\pi\rho(\varepsilon)\frac{\sin(k(\omega)R)}{k(\omega)R} \tag{2.15}$$

Retaining only the leading (quadratic) terms in L_{12} in Eq. (2.10), the exchange energy becomes

$$\Delta E_{b,ex} = -\frac{V^4}{\pi}\int_{\varepsilon_F}^{\varepsilon_{ht}} d\varepsilon \frac{P_{12}(\varepsilon)\Gamma_{12}(\varepsilon)}{[\varepsilon - E_d - V^2 P_{11}(\varepsilon)]^2 + \frac{V^4}{4}\Gamma_{11}^2(\varepsilon)}. \tag{2.16}$$

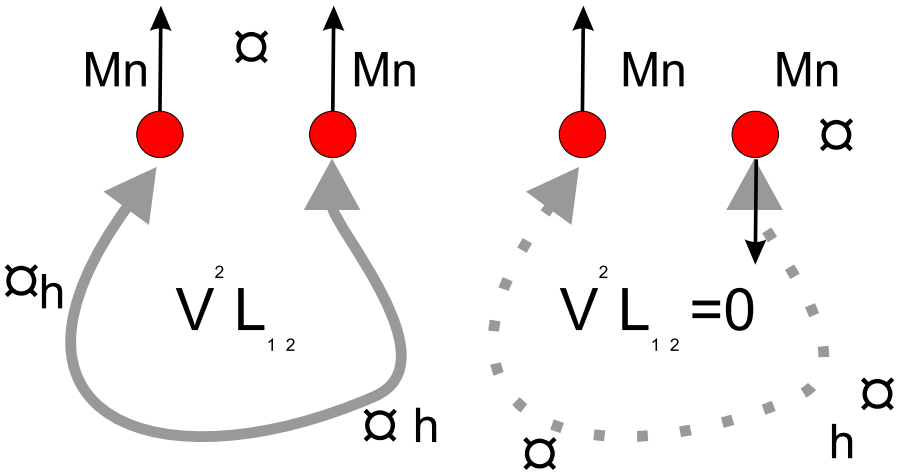

Fig. 2.1 Illustration of the exchange between two neighboring manganese impurities. The exchange, characterized by the lattice Green's function L_{12}, is hole mediated and can be carried out if the spins of the two Mn's are parallel.

Eq. (2.10) with $L_{12}(\varepsilon) \neq 0$ holds only if the impurity angular moments are parallel to each other (ferromagnetic case), since the electron hopping between the impurities via the *hh* band takes place without spin-flips. In other words impurities with non-parallel angular moments cannot exchange their electrons, which effectively means that for them $L_{12} = L_{21} = 0$. Thus, Eq. (2.16) is the energy decrease due to the kinematic indirect exchange between a pair of magnetic impurities with parallel angular moments. If the moments are not parallel the corresponding energy decrease is zero. In figure 2.1 is shown an illustration of the proposed mechanism, where it is indicated that the distance between holes are larger than distances between two neighboring Mn atoms.

Another contribution to the magnetic energy ΔE (Eq. (2.8)) originates from the inter-impurity hopping via empty localized states, if available. As was mentioned above, there are two types of such states, namely CFR and DBH-type levels. For the CFR states, one may, to a good approximation, neglect the potential impurity scattering. To take properly into account the Coulomb blockade effect on the impurity site, one has to calculate the Green

function in a self-consistent way, known as "Hubbard I" approximation (see Eqs. (6.9), (6.15) in the Appendix).

As was pointed out above, the energy gain results from the inter-impurity level splitting. The latter is derived in the Appendix (Eqs. (6.21) and (6.22)). The result is

$$\delta E_{CFR\pm} = \pm\Delta + \frac{9K^2}{2}\frac{V^4}{[1-KV^2P'_{11}]^2}\frac{dP_{12}^2}{d\varepsilon}, \tag{2.17}$$

where the splitting of the levels of the isolated impurities is

$$\Delta(\mathbf{R}) = \frac{KV^2P_{12}(\mathbf{R})}{1-KV^2P'_{11}}. \tag{2.18}$$

The second term in Eq. (2.17) results from the repulsion of the two-impurity levels from the band continuum. All the functions P_{ij} and their derivatives P'_{ij} are taken at $\varepsilon = E^0_{CFR}$, i.e. at their positions for the isolated impurities (6.21).

Considering the contribution of the DBH states we may apply the procedure outlined in the Appendix and to find the kinematic exchange due to the DBH states lying above the top of the valence band

$$\Delta E_{DBH,ex} = \frac{KV^2P_{12}^2}{(E^0_{DBH} - E_d - V^2P_{11})P'_{11}}. \tag{2.19}$$

Now all the functions in Eq. (2.19) should be calculated at the DBH level ($\varepsilon = E^0_{DBH}$). This part of the kinematic exchange favors the ferromagnetic ordering, since $P'_{11}(E^0_{DBH}) < 0$. If the DBH levels lie not too far from the top of the valence band their contribution may be comparable with that of the hole pockets and should be properly taken into account when calculating the Curie temperature. At high enough Mn content the splitting of the DBH level may result in the formation of an impurity band and its merging with the *hh* band. This case is discussed in the next section.

Thus one sees that the contribution, ΔE_{loc}, of the localized states to the kinematic exchange *is not universal*. It depends on the type of conductivity and should be considered separately for *p*- and *n*-type materials. In *p*-type samples one should take into account the empty shallow Mn-related levels, which are present in *p*-(Ga,Mn)As and *p*-(Ga,Mn)P and apparently absent in *p*-(Ga,Mn)N. In *n*-type (Ga,Mn)N, the localized states are due to the deep Mn CFR levels, and hopping over these levels alone determines the exchange mechanism. The double exchange mechanisms in these two cases are obviously different.

To calculate the Curie temperature T_C for the *p*- and *n*-type materials one should extend the two-impurity calculations for dilute materials with small Mn concentration x and take into account the corresponding transformations in the magnetic energy. This program is realized in the two next sections.

2.3 FERROMAGNETIC ORDER IN P-TYPE DMS

Here we discuss the formation of ferromagnetic order in Mn-doped III-V p-type semiconductors. (Ga,Mn)As together with (Ga,Mn)P are the most studied among them. As mentioned above, the CFR level of the fifth d electron lies in these systems below the heavy hole band. A DBH level is also formed above the top of the valence band. At high enough concentrations these DBH levels start broadening into an impurity band, and may merge with the valence band. The band structure of this system is shown schematically in Fig. 2.2.

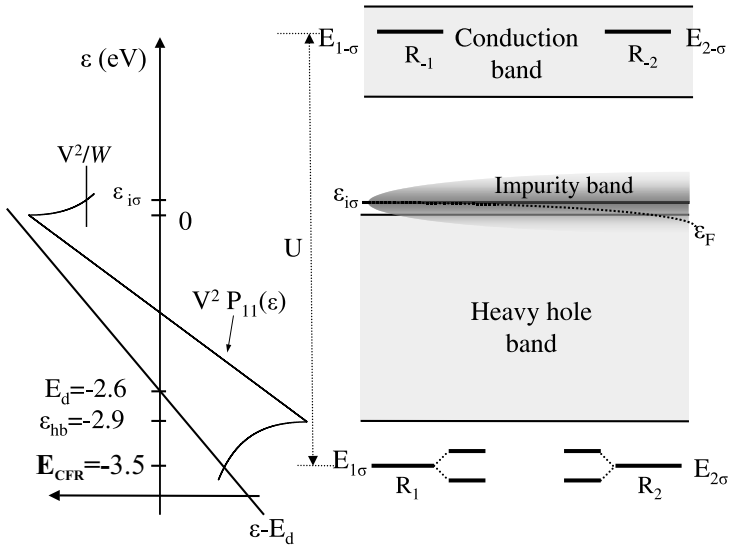

Fig. 2.2 Left panel: graphical solution of Eq. (2.23) for the bonding CFR and Eq. (2.20) for the antibonding DBH levels. Right panel: energy levels in (Ga,Mn)As. The CFR d-levels d^5/d^4(denoted by $\mathrm{R}_{1(2)}$) of each impurity, lie below the hh band. The DBH levels (energies $\varepsilon_{1\sigma}$, $\varepsilon_{2\sigma}$) form acceptor levels in the energy gap. The CFR levels d^6/d^5 $\mathrm{R}_{-1(-2)}$ lie high in the conduction band. The impurity band is shown by the shaded area.

The empty localized levels lying above the Fermi energy appear due to the combined action of both potential (W) and resonance (V) scattering mechanisms. Formally they can be found as zeros of the determinant $\mathsf{R}(\varepsilon)$ (see Eq. (6.9)). Neglecting small corrections due to resonance scattering, the energy of an isolated DBH level, $E^0_{DBH} \equiv \varepsilon_i$, corresponds to a zero of the function

$$q(\varepsilon_i) = 1 - WP_{11}(\varepsilon_i) = 0, \tag{2.20}$$

like in the Koster-Slater one-impurity problem (see the graphic solution on the left panel of Fig. 2.2). The calculations below will be carried out assuming

a model semi-elliptic density of states for the *hh* band

$$\rho(\varepsilon) = \frac{2}{w^2\pi}\sqrt{w^2 - 4\varepsilon^2},$$

where w is the *hh* bandwidth. This kind of approximation is usually taken in Hubbard, Anderson[82] and $t-J$ models. It accurately describes $\sqrt{\epsilon}$ behavior near the band edges, and is appropriate for narrow bands which is justified for heavy hole band $w = 2.9eV$[85]. Then the position of the acceptor DBH level can be found explicitly

$$\varepsilon_i = E^0_{DBH} = W\left(1 - \frac{w}{4W}\right)^2.$$

Using a realistic value for $w = 2.9eV$ [85] and taking the matrix element of the potential scattering $W \approx 1.0$ eV, one obtains the acceptor level position $\varepsilon_i = 85meV$ for (Ga,Mn)As. The lower value of the acceptor position can be explained by the Coloumb screening[86] for heavier doping. It should be noted that often cited value for acceptor level ($\approx 110meV$) is determined on low-doped (Ga,Mn)As ($x(Mn) \approx 0.01$). The influence of resonance scattering on the positions of the shallow DBH levels of the two interacting impurities may be usually neglected since the *pd*-hybridization does not affect noticeably both the position of the DBH-level (see Ref. [77] for a detailed description of the interplay between resonance and potential impurity scattering).

At sufficiently high impurity content, x, an impurity band is formed since the DBH levels are split due to the indirect interaction within the impurity pairs. We neglect the *pd*-hybridization V, keep only the contribution of the potential scattering (W) and obtain

$$\delta\varepsilon_\pm = -\frac{1}{WP'_{11}(\varepsilon_i)}\mathsf{q}_\pm, \tag{2.21}$$

where $\mathsf{q}_\pm$ are the two solutions of Eq. (6.26).

Then Eqs. (2.21) and (6.26) result in

$$\Delta_{DBH}(\mathbf{R}) \equiv \frac{1}{2}(\delta\varepsilon_+ - \delta\varepsilon_-) = -\frac{P_{12}(\mathbf{R})}{P'_{11}}$$

calculated at $\varepsilon = \varepsilon_i$. The half-width of the impurity band can be roughly estimated as $z\Delta_{DBH}(\overline{R})$ where $\overline{R}$ is the typical distance between the impurities, which depends on the impurity content x. The z value characterizes the number of neighboring impurities participating in the interaction with any given impurity. Its value is typically between 3 and 4. If the half-width $z\Delta_{DBH}(x)$ of the impurity band exceeds the energy ε_i (counted from the top of the valence band), the impurity band merges with the valence band and they both form a unified continuum of states. For the above mentioned values of the model parameters this merging occurs even at $x < 0.01$.

Eventually, the magnetic order in Mn doped III-V semiconductors is due to the exchange interaction between the occupied CFR levels. These levels correspond to the states d^5/d^4 of the Mn ions below the *hh* band, whereas the empty d^6/d^5 CFR levels are pushed up to the conduction band by the Anderson-Hubbard repulsion U (Fig. 2.2).

The left panel of this figure depicts a graphical solution of the equation

$$\mathsf{R}(\varepsilon) = 0, \tag{2.22}$$

with $\mathsf{R}(\varepsilon)$ defined in Eq. (6.9). Neglecting the interaction between the impurities, $L_{12} = 0$ (and, hence $M_{12}(R) = 0$), Eq. (2.22) takes the form

$$E_{CFR} = E_d + V^2 L_{ii}(E_{CFR}), \tag{2.23}$$

and describes the formation of the deep impurity states E_{CFR} from the atomic d-levels E_d below the *hh* valence band. The values of the parameters used in the graphical solution presented in Fig. 2.2 will be discussed below.

For a finite distance between the impurities, the overlap of impurity wave functions due to the nonzero $L_{12}(R)$ leads to a level splitting as shown in the right panel of Fig. 2.2. Each of the two impurity levels is singly occupied due to the Anderson-Hubbard on-site repulsion. The inter-impurity overlap arises due to the *pd*-hybridization, which does not involve spin-flips, hence it occurs only for the parallel impurity angular moments. There is no level splitting for the non-parallel impurity angular moments, unless one takes into account indirect interaction via empty d^6 states.

FM ordering arises, provided the state with the parallel impurity angular moments is energetically preferable in comparison to that with the non-parallel ones. It is obvious that the splitting *per se* cannot give an energy gain, when both states are occupied. One should take into account all the changes in the energy spectrum, namely, the reconstruction of the *partially filled* merged impurity and *hh* band. The indirect interaction involving empty states near the top of the *hh* band is in fact *a novel type* of the double FM exchange, which resembles the well known Zener exchange [87] but differs from it in many important aspects (see below).

The contribution favoring the FM order can be obtained from Eq. (2.16) with the addition of the part due to the impurity band merged with the valence band,

$$\Delta E_{FM} = -\frac{V^4}{\pi} \int_{\varepsilon_F(x)}^{\varepsilon_i + z\Delta_{DBH}(x)} d\varepsilon \frac{\Gamma_{12}(\varepsilon) P_{12}(\varepsilon)}{[\varepsilon - E_d - V^2 P_{11}(\varepsilon)]^2 + \frac{V^4}{4}\Gamma_{11}^2(\varepsilon)}, \tag{2.24}$$

(the reference energy in this equation is taken at the top of the *hh* band). In the FM-aligned spin configuration only the *majority* spin subband contributes to ΔE_{FM}, therefore the spin index is omitted for the sake of brevity.

We use in our numerical estimates the following approximate relations,

$$\begin{aligned} P_{11}(\varepsilon) &= P_{22}(\varepsilon) = \int d\omega \frac{\rho(\omega)}{\varepsilon - \omega}, \quad P_{12}(\varepsilon) = \int d\omega \frac{\sin k\,(\omega)\, R}{k\,(\omega)\, R} \frac{\rho(\omega)}{\varepsilon - \omega}, \\ \Gamma_{12}(\varepsilon) &\approx 2\pi\rho(\varepsilon) \sin k\,(\varepsilon)\, R/k\,(\varepsilon)\, R, \quad \Gamma_{11}(\varepsilon) \approx \pi\rho(\varepsilon) = \Gamma_{22}(\varepsilon). \end{aligned} \tag{2.25}$$

(here R is the inter-impurity distance). The value of the wave-vector k is found from the equation $\varepsilon = \varepsilon_{hh}(k)$, where $\varepsilon_{hh}(k)$ is the hh energy dispersion. In our model calculations the impurity band merges with the top of the valence band of (Ga,Mn)As at the concentration $x_{crit} = 0.0065$ with the renormalized 3d-wave-function enveloping 5 to 6 unit cells. Earlier transport measurements for low T_C samples indicate merging even at $x = 0.002$. All this justifies the approximation adopted for the hole state in Eq. (2.24). This equation is our working formula, from which we obtain T_C.

The mechanism outlined above competes with the antiferromagnetic (AFM) Anderson-type superexchange [83] involving the empty d^6 states. The energy gain in the latter case is estimated as

$$\Delta E_{AFM} \approx -V^4 L_{12}^2 / U\ . \tag{2.26}$$

It should be compared with the above Zener-type mechanisms. We assume that

$$P_{ij} \sim w^{-1}, \quad \Gamma_{ij} \sim \varepsilon_F^{1/2} w^{-3/2}, \quad \varepsilon_F - E_d - V^2 P_{11}(\varepsilon_F) = 4\alpha V^2 / w\ ,$$

with $\alpha < 1$ (see left panel of Fig. 2.2). Then one finds from Eqs. (2.24) and (2.26) that $|\Delta E_{AFM}| \sim V^4 a^2 \exp\left(-2\kappa_b R_{12}\right) / (U w^2 R_{12}^2)$, with $\kappa_b = \sqrt{2m\left(\varepsilon_{b_h} - E_{d\sigma}\right)}/\hbar$, $|\Delta E_{FM}| \sim 2\varepsilon_F \left(\varepsilon_F / w\right)^{1/2} / \left[(4\alpha)^2 + \varepsilon_F / (4w)\right]$ and FM coupling is realized provided $|\Delta E_{FM}| > |\Delta E_{AFM}|$, which normally takes place since the parameter U is large. Numerical estimates are given below.

Now the difference between the double exchange mechanism in DMS and the Zener double exchange in transition metal oxides becomes clear. The conventional Zener double exchange mechanism was proposed for (La, A^{2+})MnO_3 [87]. In this case Mn ions are in different valence states (Mn^{3+} and Mn^{4+}). In our case it would have meant that one of the two levels $E_{CFR\uparrow}$ was empty. It is seen from Fig. 2.2 that in (Ga,Mn)As both these states are occupied, and the Zener mechanism in its original form is not applicable. Actually, the FM order in the p-type DMS arises due to kinematic exchange between the two Mn(d^5) ions via the empty states near the top of the valence band.

In order to calculate the exchange energy Eq. (2.24), the dependence of the Fermi level on the Mn content $\varepsilon_F(x)$ should be known. It is governed by the equation

$$x_s = 2 \int\limits_{\varepsilon_F(x)}^{\delta w(x)} \rho\,(\varepsilon)\, d\varepsilon, \tag{2.27}$$

$\delta w(x) = \varepsilon_i + z\Delta(x)$, and the hh density of states is approximated as

$$\rho(\varepsilon) = 8/\left[\pi\left(w + \delta w(x)\right)^2\right]\sqrt{\left[\delta w(x) - \varepsilon\right](\varepsilon + w)}\theta\left[\delta w(x) - \varepsilon\right]\theta(\varepsilon + w).$$

(z is the coordination number in the impurity band). The hole concentration per site x_s is proportional to the hole density p_h; $x_s = a^3 p_h/8$ in the zinc-blende structure. Equations (2.24) and (2.27) allows one to determine the pair exchange energy as a function of Mn concentration x and connect it with the experimental data for given hole concentrations $p_h(x)$ which are taken from the measurements [88].

The Curie temperature T_C was calculated in the molecular field approximation. According to this approach the spin Hamiltonian reads

$$H_{MF} = \frac{1}{2}\sum_i \Delta E_{FM}(\mathbf{R}_{ij})\mathbf{J}_i \cdot \langle \mathbf{J} \rangle \ ,. \tag{2.28}$$

where summation runs over all positions of the Mn impurities with an angular moment operator $\mathbf{J}_i$. Here the factor $1/2$ accounts for the fact that a pair of parallel spins has the energy $\Delta E_{FM}(\mathbf{R}_{ij})$, whereas the energy of two antiparallel spins is zero, rather than $-\Delta E_{FM}(\mathbf{R}_{ij})$. Then the Curie temperature can be readily found,

$$T_C = -\frac{\Delta E_{FM}(x)}{k_B}\frac{\overline{z}J(J+1)}{6}. \tag{2.29}$$

where $\overline{z}$ is, similarly to z, a measure of the neighboring atoms participating in the exchange interaction. It is certainly close to z, although it does not necessarily coincide with it.

In (Ga,Mn)As the total angular moment of a complex Mn($3d^5\overline{p}$) is unity [68]: $J = 1$, since it is formed by the moment $j = 3/2$ of the loosely bound hole AFM-coupled to the Mn center with the spin $S = 5/2$. Then the numerical factor in Eq. (2.29) is close to unity. The results of our calculations are presented in Fig. 2.3.

In order to find $T_C(x)$, the calculated value of $\varepsilon_F(x = 0.053) = -50$meV is used in Eqs. (2.29) and (2.24). Other parameters characterizing the impurity d-state are $U \approx 4.5$ eV, $V = 1.22$eV. The latter was obtained from Eq. (2.23) with $E_i = -3.6$eV ($E_i^{\rm exp} = -3.4$eV [90]). The value of $\varepsilon_i = 85$ meV was taken for the energy of the shallow acceptor level. [71]) The value of magnetic coordination number $\bar{z}$ was fitted to achieve the best possible agreement with experimental data. For as-grown samples its value is $\bar{z} = 2.5$, while for annealed samples $\bar{z} = 4.0$. Higher value of $\bar{z}$ for annealed samples can be explained by the fact that post-growth heat treatment removes manganese interstitials which are usually antiferromagneticaly coupled to substitutional Mn thus in effect enhances the effective (magnetic) coordination number $\bar{z}$. At these values for the model parameters the ratio $|\Delta E_{FM}|/|\Delta E_{AFM}| \sim 2$ justifies the dominance of the FM coupling in (Ga,Mn)As.

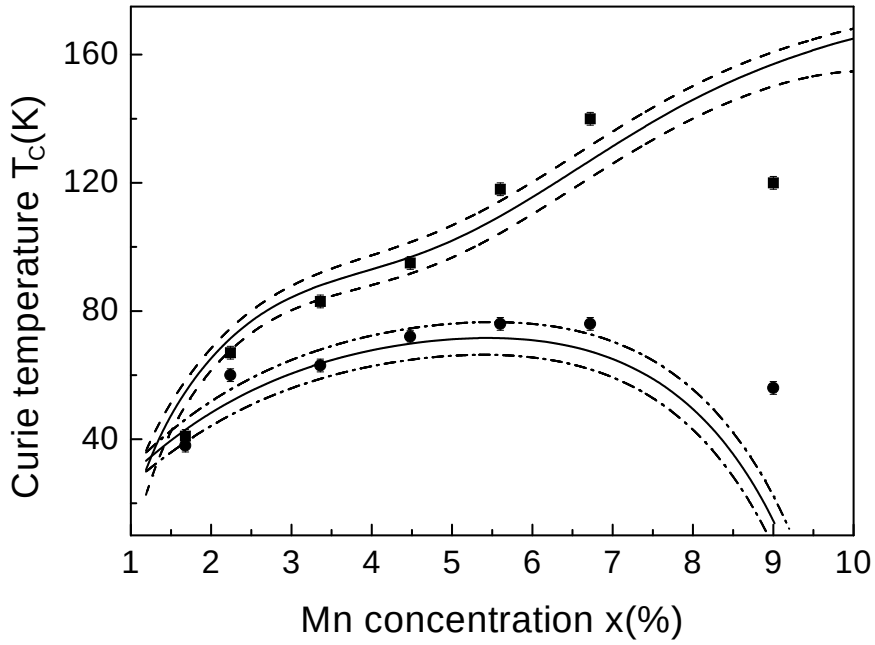

Fig. 2.3 Calculated dependence of T_C on the manganese concentration x in (Ga,Mn)As based on the experimental data for the hole density $p_h\,(x)$[88, 89]. Solid squares (circles) stand for experimental $T_C\,(x)$ of annealed (as-grown) samples. Dashed lines take into account the error bars of the hole density.

The non-monotonous dependence $T_C(x)$ is due to a non-equilibrium character of the sample preparation. Apparently, the ratio between the concentration of Mn impurities and the actual hole concentration depends on the doping method and the thermal treatment. In particular, the annealing of the sample results in a reduction of the donor-like Mn-related interstitial defects in favor of acceptor-like substitution impurities [18, 88]. A detailed measurements of the hole concentrations in a series of both as-grown and annealed $Ga_{1-x}Mn_xAs$ samples, [88] allowed us to compare the theoretical plot $T_C(p)$ with the experimental data. The Curie temperature was determined by anomalous Hall effect, using Arrot plots (M^2 vs. B/M) to improve accuracy. These results are presented in Fig. 2.4. Our fitting procedure uses the same equations (2.29) and (2.24), and the same values for the model parameters E_i, U, ε_i as in the above estimate. The Mn concentration point $x = 0.06$ is used as a reference point, while the same coordination number $\bar{z} = 4$ is taken

like in previous calculations. Two theoretical curves correspond to two values of the hybridization parameter $V = 1.24$ and 1.22 eV (solid and dash-dotted curves, respectively). One may conclude from these two fittings that the theory is not very sensitive to the choice of the model parameters. To check this statement, we made one more fitting of the experimental data obtained only for annealed samples. (see Fig. 2.5). These data are taken from Ref. [18]. We see that the calculations with the same set of model parameters give satisfactory quantitative agreement with the experiment for these samples as well.

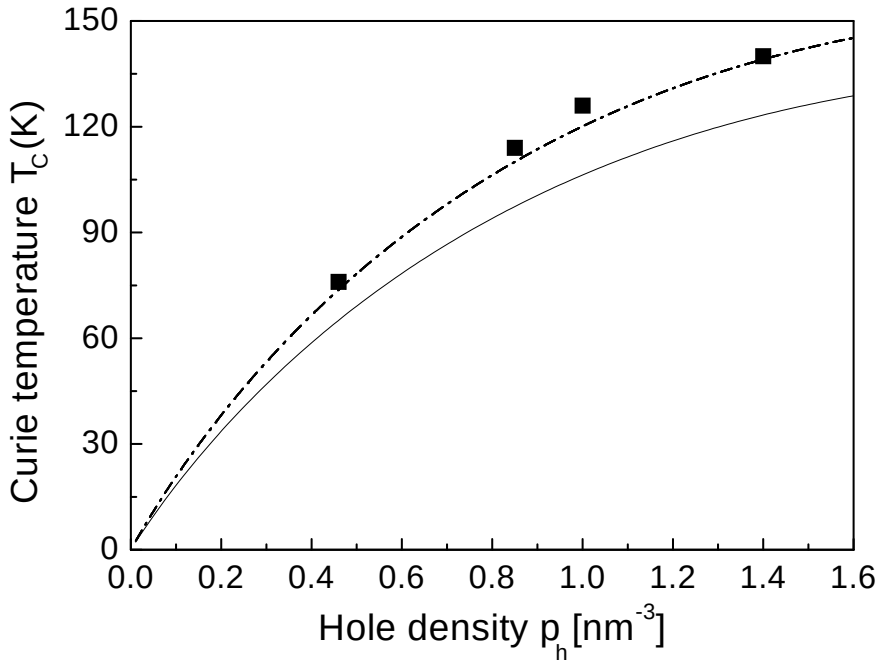

Fig. 2.4 The dependance of the Curie temperature on the hole density p_h in (Ga,Mn)As. Solid and dash-dotted lines are the theoretical curves for two values of the hybridization parameter ($V = 1.22$ and 1.24 eV, respectively), filled squares are the experimental points from Ref. [88].

Thus, our theory provides a satisfactory quantitative description of the behavior of the Curie temperature T_C as a function of the Mn content x and the hole concentration p_h in p-(Ga,Mn)As. In principle, this theory is applicable also to p-(Ga,Mn)P. It should be noted that in the latter case the DBH level lies deeper in the energy gap than in p-(Ga,Mn)As: its position

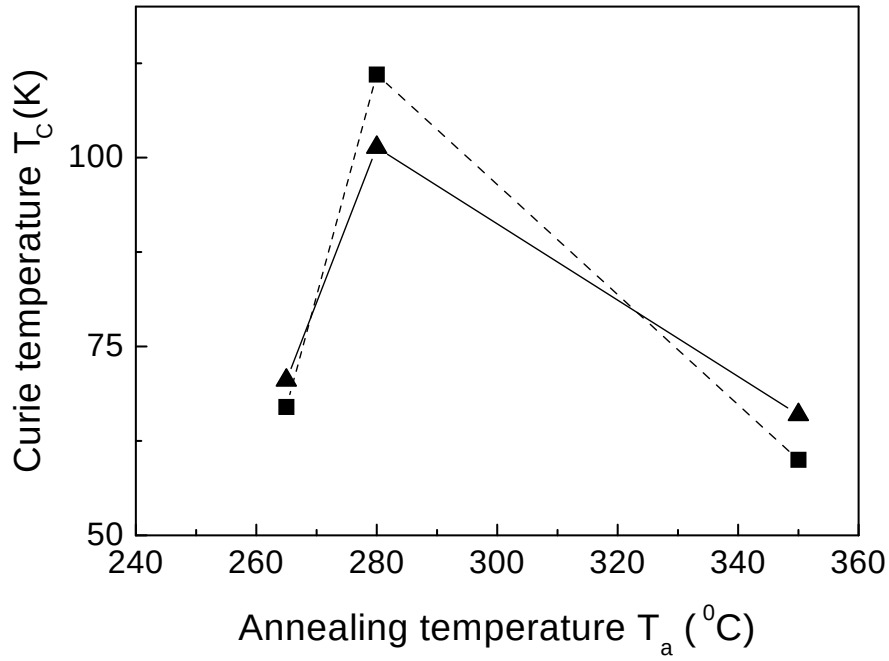

Fig. 2.5 Calculated T_C (triangles connected by a solid line) *vs* the annealing temperature T_a in (Ga,Mn)As. The data for the hole density and the experimental values of $T_C(T_a)$ (closed squares) are taken from Ref. [18]. The parameters used in the calculations are: $V = 1.22eV$, $\bar{z} = 4.0, E_{CFR} = -2.6eV$.

is estimated as ≈ 0.4 eV above the top of the valence band (see, e.g. Refs. [32, 66, 71, 85]). Presumably, this level is too deep to give a significant contribution to ΔE_{FM}. We tested our theory by fitting the experimental value of $T_C = 270$ K announced for p-type (Ga,Mn)P at $x = 0.05$ [91] with the hh bandwidth $w = 2.6eV$ and the acceptor level at $\varepsilon_i = 400meV$[85]; the calculated hybridization parameter and the deep CFR energy are $V = 1.5eV$ and $E_{CFR} = -3eV$, respectively. The values of our model parameters are close to those for (Ga,Mn)As and are in good agreement with the available information about the electronic structure of Mn doped GaP.

As to p-(Ga,Mn)N, the theory should be somewhat modified in order to describe this system. In this case Mn remains a neutral substitution isoelectronic defect in the configuration $Mn^{3+}(d^4)$, since the $Mn^{2+/3+}$ transition energy falls deep into the wide energy gap in accordance with the experimental [32] and theoretical [79] data. If the hole concentration p_h exceeds the

Mn content x, then we return to the situation discussed in this section, but with the localized moment $J = 2$ characteristic of the $Mn^{3+}(e^2t^2)$ configuration. In the opposite case, the valence band is full, and the Fermi energy lies within the deep impurity band formed by the $Mn^{2+/3+}$ levels. This situation is discussed in the next section.

Unfortunately, there is not enough experimental data on $T_C(x)$ available to make comparison with the theoretical predictions for p-(Ga,Mn)P and p-(Ga,Mn)N materials. We turn now to the case of n-(Ga,Mn)N, where the double exchange mechanism, as described above, should be revisited.

2.4 FERROMAGNETIC ORDER IN N-TYPE DMS

In accordance with the general predictions of the theory, [66, 71] Mn is a deep acceptor in GaN, and each Mn impurity creates an *empty* t_2 level close to the middle of the energy gap of GaN. Therefore, the Fermi energy should be pinned to these levels unless other (shallow) acceptors create enough free holes near the top of the valence band. This statement is confirmed by extended cluster "quasi band" calculations.[79] If a Mn-doped sample contains also shallow donors in a noticeable concentration, then the deep Mn-related impurity band is partially filled by electrons, and one arrives at the problem of magnetic order in n-type (Ga,Mn)N.

In this case the d^5/d^4 CFR energy levels forming the impurity band are partially filled, so one encounters the mixed valence Mn^{3+}/Mn^{2+} situation similarly to the original Zener model[87]. Hopping in the impurity band is possible due to an overlap of the tails of the impurity wave functions. These tails are formed by the superpositions of the Bloch electron wave functions from the hh band, so the latter in fact plays the role which is similar to that of the oxygen p-orbitals in $La(Mn,Sr)O_3$ considered by Zener.

The specific feature of the n-type (Ga,Mn)N DMS's is that the d^5/d^4 CFR impurity levels E_{CFR} lie deep within the forbidden energy gap. At a high enough Mn content they may form an impurity band, which still remains well separated from the hh band. This impurity band may be partially occupied by electrons and be responsible for the possible magnetization of the DMS. To describe the formation of a deep impurity band within the framework of our model, we solve Eq. (2.23) for a Mn-related CFR level and then substitute this solution into the secular equation (2.22). These calculations are performed using the same semi-elliptic density of valence states $\rho(\varepsilon)$ as in Section III. The bare level E_d in this case is above the top of the hh band, and the pd hybridization only slightly renormalizes its position in the energy gap. The graphical solution of Eq. (2.23) is presented in the left panel of Fig. 2.6.

We assumed that the hybridization parameter is nearly the same as in (Ga,Mn)As, $V = 1.2$ eV. The right panel of Fig. 2.6 illustrates the formation of an impurity dimer via an overlap of the tails of the CFR wave functions in accordance with Eq. (2.22). Then the electron hopping between the cor-

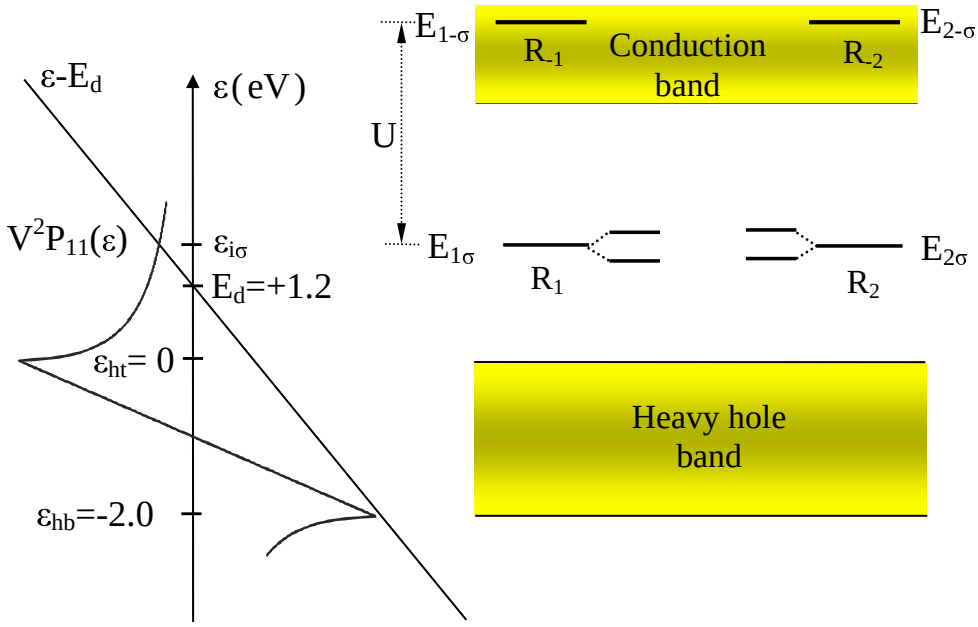

Fig. 2.6 Left panel: graphical solution of Eq. (2.23) for the antibonding CFR level in (Ga,Mn)N. Right panel: energy levels in GaN:Mn. The CFR d-levels d^5/d^4(denoted by $R_{1(2)}$) of each impurity, lie in the energy gap. The CFR levels d^6/d^5 $R_{-1(-2)}$ lie high in the conduction band.

related states R_1 and R_2 initiates the formation of an impurity band and the Zener type indirect exchange interaction arises, provided the impurity band is partially occupied. The empty (d^6/d^5) CFR levels are pushed up high to the conduction band by the Anderson-Hubbard repulsion U. Like in the previous case these levels can be a source of AFM ordering in the impurity band, but we do not consider this relatively weak mechanism here.

In order to calculate the double exchange interaction in such an impurity band, we consider first a pair of impurities at a distance R from each other. To be definite we assume that the Fermi energy E_F lies below the level E_{CFR} of an isolated impurity. According Eq. (2.18) the interaction between the

impurities results in splitting of the impurity levels with half-width $\Delta(R)$, where we neglect its possible dependence on the direction of the vector $\mathbf{R}$.

It is emphasized here again that the *pd* hybridization does not involve spin flips. It means that the electron spin does not change its projection in the course of the whole process leading to the indirect exchange.

One may conclude that the indirect exchange interaction within a pair of impurities appears if their angular moments are parallel (FM ordering), and if the distance between the impurities is not too large, i.e.

$$R < R_{ex}(\mu)$$

where $R_{ex}(\mu)$ is the solution of the equation

$$\Delta(R_{ex}) = E^0_{CFR} - E_F. \tag{2.30}$$

where $\Delta(R_{ex})$ is the half the value of impurity level splitting. Then one of the two impurity levels sinks below the Fermi energy and is occupied by an electron resulting in the energy decrease $\Delta(R)$, whereas the second level remains empty and does not contribute to the energy balance. If the angular moments of the impurities are not parallel, Hund's rule forbids the indirect exchange and there is no energy decrease. Therefore, we conclude that the exchange energy in such a pair equals just $-\Delta(R)$. It is zero if at least one of the above two conditions is not met.

The pair exchange interaction can be estimated as

$$\overline{\Delta} = \int_0^{R_{ex}(\mu)} \Delta(R) g(R) dR \tag{2.31}$$

where $g(R)$ is the impurity pair distribution function. For example, we may assume that the random distribution of the impurities obeys the Poisson law

$$g(R) = \frac{3R^2}{\overline{R}^{\,3}} \exp\left\{-\frac{R^3}{\overline{R}^{\,3}}\right\} \tag{2.32}$$

where $\overline{R}$ is the average distance between the impurities. The latter is connected with the impurity content x by $\frac{4\pi}{3}\overline{R}^{\,3}x = 1$.

This assumption may not work too well for relatively high impurity content, since it overestimates the contribution of closely lying impurities. In fact the impurities cannot approach each other to distances smaller than the lattice spacing. In such a case corrections should be introduced for these small distances.

In order to complete our calculations, we need also an equation connecting the position of the Fermi energy with the electron concentration n in the impurity band. This concentration coincides with the concentration of impurities in the d^5 state, hence

$$n = \int^{\mu} \rho(\varepsilon) n_{d^5}(\varepsilon - E_F) d\varepsilon \tag{2.33}$$

where $\rho(\varepsilon)$ is the density of states in the impurity band. The distribution $n_{d^5}(\varepsilon - E_F)$ is calculated in the Appendix, Eq. (6.15). At low temperatures $n_{d^5}(\varepsilon - E_F)$ is 1 for $\varepsilon < E_F$ and 0 for $\varepsilon > E_F$. This allows us to circumvent the calculation of the density of states $\rho(\varepsilon)$ and present the condition (2.33) in the alternative form

$$n = \int_0^{R_{ex}(\mu)} g(R)dR, \tag{2.34}$$

which is more convenient for our calculations. If an experiment provides us with dependencies of the Curie temperature and the electron concentration on the Mn content, then Eqs. (2.30) and (2.34) will allow us to connect the Fermi energy with the electron density in the impurity band and after that to use Eq. (2.31) in order to calculate the average pair exchange interaction $\overline{\Delta}(x)$ as a function of the impurity content x.

We may now use the theory of dilute ferromagnetic alloys developed in Ref. [92] (see also the review Ref. [93]) and arrive at the final result of this procedure, i.e. the Curie temperature

$$T_C(x) = \frac{J(J+1)}{6k_B}\overline{\Delta}(x) \tag{2.35}$$

determined by the average value of the pair exchange interaction. In the case of Mn in GaN we have $J = 2$.

At low electron concentrations, when $R_{ex}(E_F) > a$, only a minor part of the impurities is coupled by the indirect exchange interaction. Using the above averaging procedure for calculating T_C does not hold any more and a percolation type of approach should be applied. The resulting Curie temperature may become low and will decrease exponentially with the concentration. [94]

The behavior of the Curie temperature for higher electron concentrations when the Fermi energy lies above the energy E^0_{CFR} can be found in a similar fashion. We just have to switch to the hole representation and use the distribution function $3n_{d^4}(\varepsilon - E_F)$ instead of $n_{d^5}(\varepsilon - \mu)$. (Dealing with holes we have now to account for the three fold degeneracy of the t_2 states.) The function $3n_{d^4}$ is 1 if $\varepsilon > E_F$ and 0 if $\varepsilon < E_F$. As a result, we will obtain a mirror symmetric dependence of T_C on x in this concentration range.

To get an idea of the behavior of the average kinematic exchange $\overline{\Delta}$ and, hence of the Curie temperature as a function of the Mn content and the position of the chemical potential, i.e., electron concentration in the impurity band, we can make simple estimates. Consider the case when $E_F < E_{CFR}$, then $K = 1$ and according to Eq. (6.22) the levels of a pair of impurities separated by the distance R are split by

$$\delta\varepsilon_\pm = \pm\Delta(R) = \pm\frac{V^2 P_{12}(R)}{1 - V^2 P'_{11}}\,, \tag{2.36}$$

where the off-diagonal lattice sum can be estimated as

$$P_{12}(R) = \frac{1}{2\pi}\frac{ma^3}{\hbar^2 R}e^{-\kappa R}. \tag{2.37}$$

Here a is the lattice spacing and κ is the localization parameter. (Although we may use the estimate $\kappa \approx \hbar\sqrt{2mE_{CFR}}$, we should not forget that it may be rather crude for really deep levels.) Then

$$\Delta(R) \approx \Delta_0 \frac{a}{R} e^{-\kappa R} ,$$

where the value of Δ_0 depends on the parameters of the system but is generally of the order of 1eV.

The Poisson pair distribution truncated at small distances $R < a$ is chosen to be

$$g(R) = \begin{cases} \dfrac{3R^2}{\overline{R}^{\,3}} \exp\left\{\dfrac{a^3 - R^3}{\overline{R}^{\,3}}\right\}, & \text{for} \quad R > a \\ 0, & \text{for} \quad R < a \end{cases} . \tag{2.38}$$

This distribution accounts for the fact that the Mn impurities cannot come closer than a distance a from each other. For a deep enough level we may assume $\kappa \approx 1/a$ and calculate the dependence of the average kinematic exchange $\overline{\Delta}$ on the Mn content and position of the Fermi energy with respect to the isolated impurity level E_{CFR} (see Fig. 2.7). The two latter quantities are measured in units Δ_0 meaning that the kinematic exchange and, hence, the Curie temperature is maximal for any given value of x when the impurity band is half filled, i.e., $E_F = E^0_{CFR}$. At $x = 0.05$ the kinematic exchange $\overline{\Delta}$ may be about 0.035eV for Δ_0 =1eV. The angular moment $J = 2$ for the d^4 state of the Mn impurity in GaN, hence $T_C = \overline{\Delta}/k_B$, and we find $T_C \approx 300$K.

It is worth mentioning that by choosing the localization radius so small, $\kappa^{-1} \approx a$, we have actually found a lower bound for $\overline{\Delta}$. At larger values of the localization radius, we obtain a similar dependence of the exchange energy $\overline{\Delta}$ on the Mn content and the Fermi energy position, however the absolute value of $\overline{\Delta}$ may become essentially larger, e.g. $\sim$0.1eV for $\kappa^{-1} \approx 2a$ in the maximum (see Fig. 2.8). Then the Curie temperature may become as high as 1000K.

We should emphasize here again that the averaging procedure used to obtain the results in Figs. 2.7 and 2.8 works well only when the Fermi energy is close to the impurity level E^0_{CFR} (zero on the Fermi energy axis). Far from this region one should apply the percolation approach proposed in Ref. [94]. Then the effective kinematic exchange in this range may become smaller than shown in the figures, however the behavior does not change qualitatively, and certainly remains correct also quantitatively for E_F close to E^0_{CFR}. Experimental evidence of the Curie temperature dependence on the Fermi level position is given in Ref.[95], where series of samples of (Ga,Mn)N with different level and type of doping were examined. If (Ga,Mn)N is doped with increasing

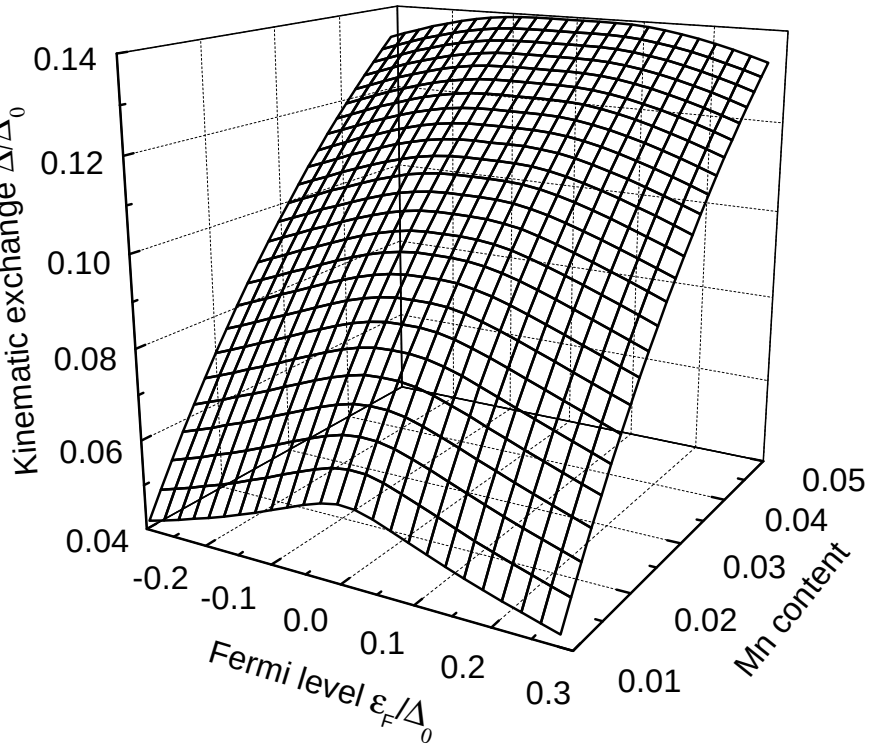

Fig. 2.7 Dependence of the kinematic exchange, measured in units of Δ_0 on the Mn content (x), and on the position of the Fermi energy relative to the level E_{CFR} of an isolated Mn impurity. We took $\kappa^{-1} = a$.

concentration of Si (n-type), the Fermi level approaches the conduction band, the transitional temperature vanishes, while the opposite behavour is noticed with Mg doping. The highest temperatures were obtained when the Fermi level was located close to the Mn derived impurity band which supports our findings that optimal T_C corresponds to a half-filled impurity band.

2.5 CONCLUDING REMARKS

According to the presented theory of magnetic interactions, the kinematic exchange between localized impurity spins embedded in a semiconductor host with covalent chemical bonding [96] is a generic property of the two-impurity

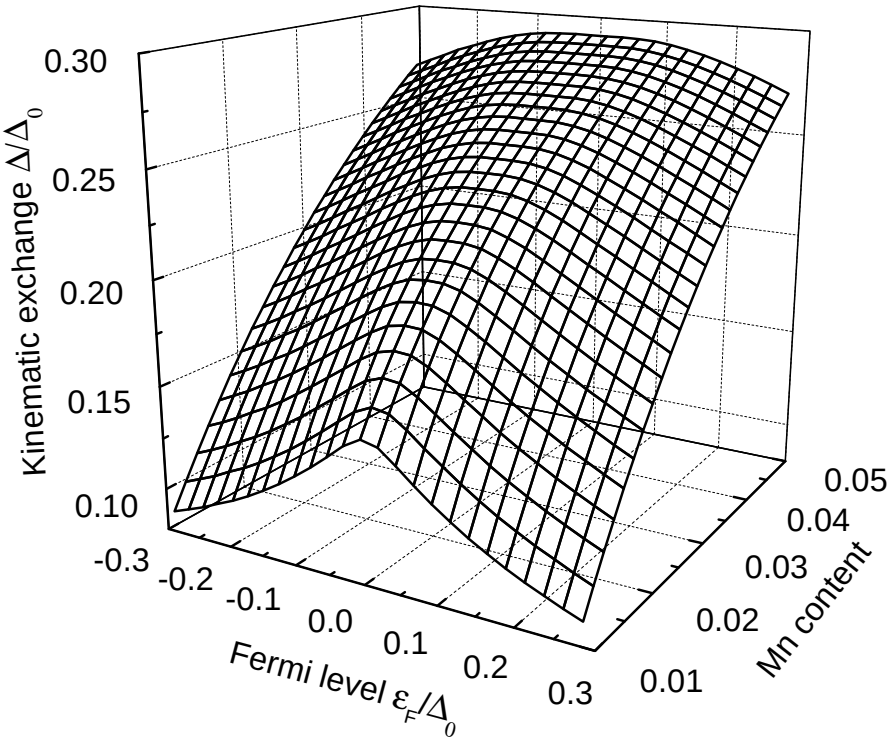

Fig. 2.8 The same as Fig. 6 but now for $\kappa^{-1} = 2a$.

cluster. We constructed such a cluster which was based on an ab initio knowledge about the electronic structure of isolated Mn impurity in a III-V semiconductor. After some simplifications this approach led us to a microscopic Hamiltonian similar to a two-center Anderson model. [83] This model allows for analytical solutions, and the final equation (2.29) for T_C with effective coupling constant (2.24) should be compared with the phenomenological mean-field equation [97, 98]

$$T_C = \frac{4xJ(J+1)K_{pd}^2}{3a} \frac{\chi_h}{(g\mu_B)^2}\,, \tag{2.39}$$

where a is the lattice constant, K_{pd} is the phenomenological pd-exchange constant, χ_h is the magnetic susceptibility of holes in the valence band. In principle, Eq. (2.29) and Eq. (2.39) consist of similar ingredients. It is natural to assume that J_{pd} in the phenomenological model stems from the

hybridization. Then it may be derived in the Anderson-type model by means of the usual Schrieffer-Wolff transformation, so that $K_{pd} \sim V^2/(\varepsilon_F - E_d)$. One easily discerns corresponding contributions in Eq. (2.24). The second fraction in Eq. (2.39) is proportional to $m^* k_F$, so the kinetic energy of metallic holes in the conduction band is its measure. *Unlike* the phenomenological model, which deals with localized spins and free holes near the top of the conduction band, our model takes into account the change in the density of hole states (and therefore in their magnetic response) due to resonance scattering and impurity band formation. One of the results of this change is a more complicated dependence of the magnetic coupling on the Mn content x than the linear law predicted by Eq. (2.39). Another improvement of the mean-field theory taken into account in Eq. (2.29) is a more refined description of the impurity magnetic moment. The actual moment J arises as a vector sum of the moments of the d-electrons and the bound p-hole, One should emphasize that at a high enough concentration all mean-field descriptions fail because the alloy approaches the instability region and the Mn distribution becomes strongly inhomogeneous. In the case of $Ga_{1-x}Mn_xAs$ this is, apparently, the region of $x > 0.07$.

Next, one should discuss the relation between our approach and the so called "ab initio" numerical calculations by means of the local-density functional method. [31, 79] Doping by Mn atoms is modeled in these calculations by means of a finite-size cluster of GaAs or GaN with one or several atoms replaced by Mn. Then periodic structures are constructed from magnetic clusters ("supercells") and the electronic bands in these artificial objects are calculated in the conventional local-spin-density approximation (LSDA). So, the starting point in our approach and the LSDA calculations is the same. No wonder that the positions of CFR and DBH levels in these calculations are in good agreement with those used in our model, based on previous single impurity calculations. [66, 71] However, a direct comparison of the two procedures, as far as the magnetic properties are concerned, is somewhat problematic. The self-consistent LSDA method results *by construction* only in a Stoner-like itinerant magnetism. Therefore, magnetic states are discussed in Refs. [31, 79] in terms of exchange splitting and majority/minority spin subbands. It is difficult to discern the genuine kinematic double exchange in this type of calculations.

To overcome this difficulty, Sanvito *et al* [31] tried to fit their LDSA calculation by a free-electron model with an effective hole mass m^* and uniformly distributed impurities described by the model square potential containing spin-independent and exchange components ($W(r)$ and $J(r)$, respectively). Such separation is purely phenomenological. It ignores the resonance origin of the exchange potential. Besides, short-range impurity scattering cannot be described in the effective mass approximation[77]. Nevertheless, the estimate of the magnetic component $|J| = 1.05$ eV is in good agreement with the corresponding parameter of our theory $\bar{z}V^2/E_i = 1.034$ eV for the parameters used in the fitting of Fig. 2.4 (the value of $W = 0.027$ eV is irrelevant because of

the above mentioned effective mass approximation). One should emphasize, however, that the double-exchange coupling in our model is determined not by this parameter, but by the integral ΔE_{FM} (2.24), and this difference is in fact the benchmark for discussion of the differences between the indirect pd exchange of Vonsovskii-Zener type [99] and the kinematic double exchange. [87]

A simplified picture of the valence band structure used in our model (single heavy-hole band with semielliptic density of states) allows us to describe the dependence $T_C(x, p)$ by a minimum number of fitting parameters. We have seen that the good quantitative agreement between theory and experiment could be achieved even with this very restricted set of parameters. With the help of a more realistic energy band scheme (e.g. by taking the light hole band into account), the restrictive symmetry of the density of states would be removed, and the fitting procedure would become more flexible. We intentionally imposed such severe restrictions on the model to demonstrate its explanatory capabilities. The above limitations will be lifted in future studies.

Further progress in the theoretical description of ferromagnetism in Mn-doped semiconductors is intimately related to the progress in sample preparation and characterization. At present more or less detailed data on $T_C(x, p)$ in p-type (Ga,Mn)As are available, and we succeeded in a quantitative description of these data within our model (Section III). We expect that the same approach is applicable to p-type (Ga,Mn)P, but the scanty experimental data do not allow us to check this expectation. As for (Ga,Mn)N, the accumulation of experimental data is in progress, and the most actual task is to reveal distinctions between p- and n-type magnetic alloys. According to our theory, FM order is expected in both cases, but the latter one demands a serious modification of the theory (Section IV) and a direct extrapolation of the semi-empirical formula (2.39) is questionable.

Publications. The results presented in this chapter were published as

- P. M. Krstajić, V. A. Ivanov, F. M. Peeters, V. Fleurov, K. Kikoin *Ferromagnetism in Mn-doped GaAs: The Kinematic Exchange*, Journal of Superconductivity **16**, 111 (2003) (3 pages).

- P. M. Krstajić, F. M. Peeters, V. A. Ivanov, V. Fleurov, and K. Kikoin, *Double-exchange mechanisms for Mn-doped III-V ferromagnetic semiconductors*, Phys. Rev. B **70**, 195215 (2004) (16 pages).

- P. M. Krstajić, V. A. Ivanov, F. M. Peeters, V. Fleurov, and K. Kikoin, *On the nature of ferromagnetic exchange in Dilute Magnetic Semiconductors: GaAs:Mn*, Europhys. Lett. **61**, 235 (2003) (7 pages).

- V. A. Ivanov, P.M. Krstajić, F. M. Peeters, V. Fleurov, K. Kikoin, *On the ferromagnetic exchange in Mn-doped IIIV semiconductors*, Physica B **329**, 1282 (2003) (2 pages).

• V. A. Ivanov, P. M. Krstajić, F. M. Peeters, V. Fleurov and K. Kikoin *On the Nature of Ferromagnetism in Dilute Magnetic Semiconductors: GaAs:Mn and GaP:Mn* Journal of Magnetism and Magnetic Materials **258**, 237 (2003) (4 pages).

3

Hole transport in GaAs/AlAs structures

3.1 INTRODUCTION

The idea is to study hole tunneling through DMS materials. Therefore, we will first develop and test the formalism on hole tunneling without the extra complication of Mn dopant atoms, but in case a external magnetic field is present in the tunnel barrier. Chemical bonds in III-V semiconductors are formed from 8 outer electrons of the constituent atoms in a unit cell. Since outermost shells of the atoms are s and p orbitals, III(s^2p^1) and V(s^2p^3), they hybridize to form tetrahedral bonds producing, within the tight-binding picture two levels: one bonding and one antibonding. In a crystal with a large number of unit cells they merge into bands: the *valence bands* from bonding levels which are occupied with electrons, and the *conduction bands* from antibonding levels which are empty at zero temperature. The topmost valence bands (Γ_8) are originated from bonding p-orbitals of constituent atoms which are anisotropic in space. Therefore, any theory of motion of electrons in the valence bands, i.e. holes should take into account from the beginning the angular momentum $l = 1$ of holes. Another consequence is that the valence band is degenerate (apart of spin) in the center of the first Brillouin zone (Γ point, see Fig.3.3). Coupling of angular momentum with the spin gives two possible values of total angular momentum $j = 3/2$ and $1/2$. The four states $|3/2, j_z\rangle$ form the irreducible representation Γ_8 of the point group T_d of symmetry, while two states $|1/2, j_z\rangle$ form the irreducible representation Γ_7. The initial three-fold degeneracy is, however, partially lifted by spin-orbit coupling, leading to separation of Γ_8 and Γ_7 points. That is the reason why

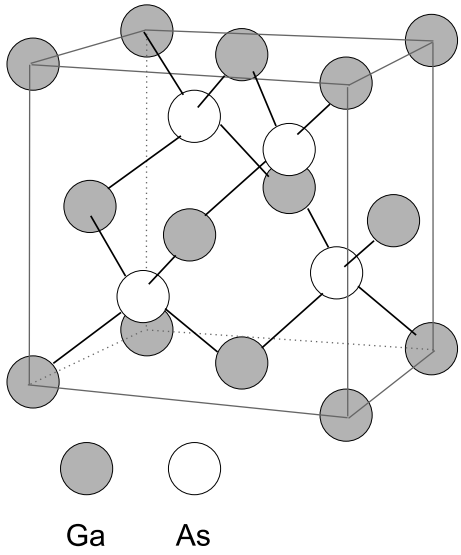

Fig. 3.1 Crystal structure of GaAs that consists of two face centered cubic lattices moved along the fourth of a diagonal of the cube.

the band formed by $|1/2, j_z\rangle$ hole states is called split-off band. It turns out that, within the first group, energy dispersion $E(k)$ of states $|3/2, \pm 3/2\rangle$ have less pronounced curvature than that of $|3/2, \pm 1/2\rangle$ states (in the vicinity of Γ_8 point). These states are called heavy and light holes respectively. On the other hand, successes of effective mass theory for electrons in semiconductors opens possibility to formulate sufficiently accurate analog theory for holes. However, due to complex nature of valence band, it turns out it can not be described by a simple scalar mass. Historically W. Shockley[102] first proposed effective tensor mass, whose form yields from general properties of symmetry of a cubic lattice. Effective mass tensor $D^{\alpha\beta}_{jj'}$ plays similar role of an effective scalar mass but here containing more information about the direction in space: α, β run over x, y, z; and 'interaction' among degenerate bands: j runs over different valence bands: heavy, light and split-off hole band. Luttinger and Kohn refined those ideas in their seminal papers[104, 105]. The basic idea of the effective mass theory is that the motion of an electron or a hole can be described by the effective mass tensor (in general) if the external potential V varies smoothly through the unit cell, and the Bloch functions at the top of the bands do not change rapidly across different materials in the heterostructure. The total wave function ψ can then be expressed as a product of a slowly varying envelope function $F = (F_1, F_2, ..., F_m)^T$ and

Bloch's function in the center of the first Brillouin zone u_{n0}.

$$\psi(\mathbf{r}) = \sum_{i=1,m} F_i(\mathbf{r}) \cdot u_{i0}(\mathbf{r}) \tag{3.1}$$

It is proven by Luttinger and Kohn that the functions u_{n0} form a complete set of basis functions. Envelope function $F = (F_1, F_2, ..., F_m)^T$ are determined by the band-alignment of semiconductors in a heterostructure, and a few phenomenological parameters of materials that enters the effective mass tensor. If the heterostructure layers are thick enough $d > 20$Å, envelope functions describe of holes with sufficient accuracy. First, we will consider case of a bulk semiconductor, where the one-electron Schrödinger equation with spin-orbit interaction included reads

$$\left(\frac{\mathbf{p}^2}{2m_0} + V(\mathbf{r}) + \frac{\hbar}{4m_0^2c^2}(\sigma \times \nabla V) \cdot \mathbf{p} \right) \psi(\mathbf{r}) = E\psi(\mathbf{r}) \tag{3.2}$$

On the other hand, periodicity of the crystal implies the following form of the one-electron wave function

$$\psi_{n\mathbf{k}}(\mathbf{r}) = u_{n\mathbf{k}}(\mathbf{r}) e^{i\mathbf{kr}}\,, \tag{3.3}$$

according to Bloch's theorem. Upon inserting this equation into Eq. (3.2), one arrives at

$$\left\{ \frac{\mathbf{p}^2}{2m_0} + V(\mathbf{r}) + \frac{\hbar}{4m_0^2c^2}(\sigma \times \nabla V) \cdot \mathbf{p} + \frac{\hbar^2 k^2}{2m_0} + \frac{\hbar\mathbf{k}}{m_0} \cdot [\mathbf{p} + \frac{\hbar}{4m_0c^2}(\sigma \times \nabla V)] \right\} u_{n\mathbf{k}} = E_{n\mathbf{k}} u_{n\mathbf{k}}$$

Note that $\mathbf{p}$ is the momentum of the electron, while $\hbar\mathbf{k}$ is the crystal momentum associated with the translational invariance of the crystal. The

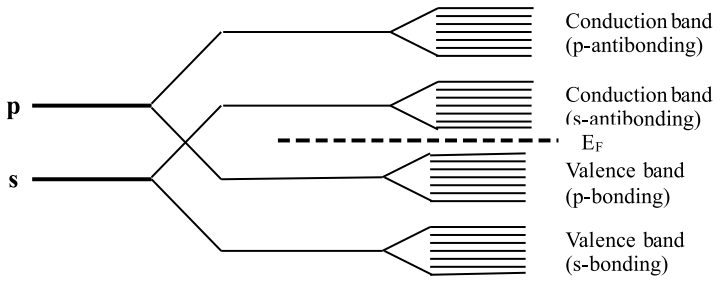

Fig. 3.2 Scheme of formation of bands in a semiconductor

appearance of the term $\mathbf{k}\cdot\mathbf{p}$ is the reason why the method is called $\mathbf{k}\cdot\mathbf{p}$ model. This equation can be rewritten as

$$\{H_0 + W(\mathbf{k})\}u_{n\mathbf{k}} = E_{n\mathbf{k}}u_{n\mathbf{k}}\,, \tag{3.4}$$

where H_0 contains no terms with $\mathbf{k}$. For small values of $\mathbf{k}$, i.e. near the Γ point, one can treat $W(\mathbf{k})$ as a perturbation, and write solutions as a series expansion of eigenfunctions u_{n0}

$$u_{n\mathbf{k}} = \sum_m c_m^n(\mathbf{k})u_{m0} \tag{3.5}$$

Usually, only limited number of bands (around the band of interest) is included in the expansion in order to simplify the calculations. The second order eigenenergies are then given by

$$E_{n\mathbf{k}} = E_{n0} + \frac{\hbar^2k^2}{2m_0} + \frac{\hbar^2}{m_0^2}\sum_{m\neq n}\frac{|\langle u_{n0}|\,\mathbf{k}\cdot\pi\,|u_{m0}\rangle|^2}{E_{n0}-E_{m0}}\,, \tag{3.6a}$$

$$\pi = \mathbf{p} + \frac{\hbar}{4m_0c^2}(\sigma\times\nabla V)\,. \tag{3.6b}$$

Thus for small k, the third term gives a correction to the second one, and one can write, up to the second order

$$E_{n\mathbf{k}} = E_{n0} + \frac{\hbar^2k^2}{2m^*}, \tag{3.7}$$

where m^* is called the effective mass. However, this relation is correct if all bands are non-degenerate (apart from spin). On the other hand, it may happen that some bands are too remote, so that they give only a "fine-tuning" of the relevant parameters. One should separate then the bands into two groups: A group - where the bands are treated exactly, and B-group where their influence is treated perturbatively. This approach was first proposed by Kane[103], and he considered valence bands (6 bands with spin included) and the lowest conduction (2 bands) which leads to 8×8 band $\mathbf{k}\cdot\mathbf{p}$. However, if the bandgap E_g is large compared to the interaction between the conduction and the valence band $\hbar^2/m_0^2|\langle u_{c0}|\,|\mathbf{k}\cdot\pi\,|u_{v0}\rangle|^2$, then it is sufficient to consider only the valence band themselves, which was elaborated by Luttinger and Kohn[104, 105]. We will start from their 6 - band $\mathbf{k}\cdot\mathbf{p}$ theory, and go back to Kane's model in the next chapter. In the beginning of the formulation of the theory, one usually omits the spin degree of freedom. In this case the matrix equation for the expansion coefficients c_j (j runs over bands $j = 1, 2, 3$) has the general form

$$\sum_{j'} D_{jj'}^{\alpha\beta}k_\alpha k_\beta c_{j'}(\mathbf{r}) = Ec_j(\mathbf{r}), \quad \alpha,\beta = x,y,z \tag{3.8}$$

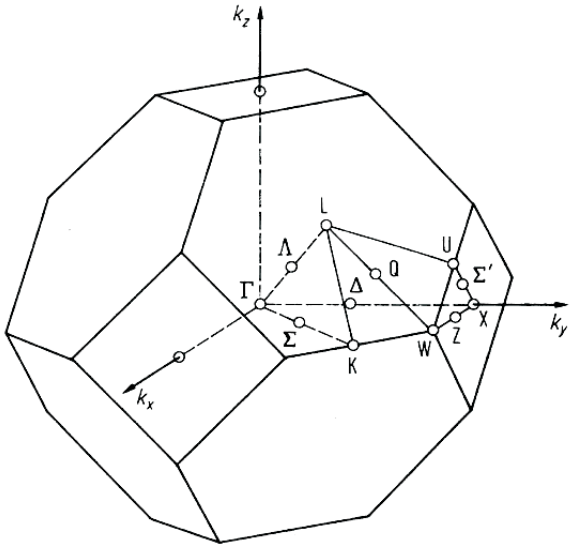

Fig. 3.3 The first Brillouin zone with points of high symmetry. For face centered cubic (FCC) lattices it is a truncated octahedron.

since we have decided to restrict ourselves to second order in $\mathbf{k}$. It follows from degenerate perturbation theory, that the effective tensor D should be

$$D_{jj'}^{\alpha\beta} = \frac{1}{2m_0}\delta_{jj'}\delta_{\alpha\beta} + \frac{1}{m_0^2}\sum_i \frac{\pi_{ji}^{\alpha}\pi_{ij'}^{\beta}}{E_0 - E_i}\,. \tag{3.9}$$

As mentioned earlier, the carriers in the valence bands possess angular momentum $l = 1$, and thus there are three degenerate, f_X, f_Y, and f_Z functions (in the absence of spin-orbit coupling) in the center of the Brillouin zone ($k = 0$). They transform like x,y,z coordinates under the operations of the cubic point group. Finally, the Hamiltonian $H_{3\times3}$ without spin degree of freedom is

$$H_{jj'} = D_{jj'}^{\alpha\beta}k_\alpha k_\beta\,, \tag{3.10}$$

$$H_{3\times3} = \begin{pmatrix} Ak_x^2 + B(k_y^2+k_z^2) & Ck_xk_y & Ck_xk_z \\ Ck_xk_y & Ak_y^2 + B(k_x^2+k_z^2) & Ck_yk_z \\ Ck_xk_z & Ck_yk_z & Ak_z^2 + B(k_x^2+k_y^2) \end{pmatrix}, \tag{3.11}$$

where new parameters A, B, C are defined through

$$A = D_{XX}^{xx}, \quad B = D_{XX}^{yy}, \quad C = D_{XY}^{xy} + D_{XY}^{yx}\,. \tag{3.12}$$

The appearance of only three parameters is a consequence of the fact that in a cubic symmetry real tensors of rank 4 like $D_{jj'}^{\alpha\beta}$ have only three independent non-zero components[106]. For instance, it can be proven that D_{XY}^{xz} vanish, so that $D_{XY} = D_{XY}^{xy}k_xk_y + D_{XY}^{yx}k_yk_x = Ck_xk_y$. The relation of A, B, C with more common Luttinger parameters is:

$$A = \frac{\hbar^2}{2m_0}(\gamma_1 + 4\gamma_2),\ B = \frac{\hbar^2}{2m_0}(\gamma_1 - 2\gamma_2),\ C = \frac{\hbar^2}{2m_0}(6\gamma_3)\,. \tag{3.13}$$

Until now, the spin degree is neglected, which is justified only if spin-orbit interaction is small. However in most III-V semiconductors it has significant influence on the band structure, and the corresponding term in the total Hamiltonian is

$$H_{so} = \frac{\hbar}{4m_0^2c^2}\sigma \cdot (\nabla V \times \mathbf{p}) \tag{3.14}$$

The full Hamiltonian with spin degree included, i.e. in $X\uparrow, Y\uparrow, Z\uparrow, X\downarrow, Y\downarrow$, $Z\downarrow$ basis, is given as

$$H_{6\times6} = \begin{pmatrix} H_{3\times3} & 0 \\ 0 & H_{3\times3} \end{pmatrix} + \begin{pmatrix} G_{so} & \Gamma \\ -\Gamma^* & G_{so} \end{pmatrix}, \tag{3.15}$$

where

$$G_{so} = \frac{\Delta_{so}}{3}\begin{pmatrix} 0 & -i & 0 \\ i & 0 & 0 \\ 0 & 0 & 0 \end{pmatrix}, \tag{3.16}$$

and

$$\Gamma = \frac{\Delta_{so}}{3}\begin{pmatrix} 0 & 0 & 1 \\ 0 & 0 & i \\ -1 & i & 0 \end{pmatrix}. \tag{3.17}$$

Here the quantity Δ_{so} is the energy separation between the split-off bands $|1/2, \pm 1/2\rangle$ (Γ_7) and the rest of bands $|3/2, j_z\rangle$ (Γ_8).

$$\Delta_{so} = \frac{3i\hbar}{4m_0^2c^2}\langle X| \frac{\partial V}{\partial x}p_y - \frac{\partial V}{\partial y}p_x |Y\rangle\ . \tag{3.18}$$

In the presence of spin-orbit coupling it is more convenient to change into $|j, j_z\rangle$ basis, since they are good quantum numbers.

$$u_{10} = \frac{1}{\sqrt{2}}\,|(X + iY)\uparrow\rangle\ , \tag{3.19a}$$

$$u_{20} = \frac{i}{\sqrt{6}}\,[|(X + iY)\downarrow\rangle - 2\,|Z\uparrow\rangle]\ , \tag{3.19b}$$

$$u_{30} = \frac{1}{\sqrt{6}}\,[|(X - iY)\uparrow\rangle + 2\,|Z\downarrow\rangle]\ , \tag{3.19c}$$

$$u_{40} = \frac{i}{\sqrt{2}} \left|(X - iY)\downarrow\right\rangle , \tag{3.19d}$$

$$u_{50} = \frac{1}{\sqrt{3}} \left[\left|(X + iY)\downarrow\right\rangle + \left|Z\uparrow\right\rangle\right] , \tag{3.19e}$$

$$u_{60} = \frac{i}{\sqrt{3}} \left[-\left|(X - iY)\uparrow\right\rangle + \left|Z\downarrow\right\rangle\right] . \tag{3.19f}$$

The basis eigenfunctions u_{i0} are the periodic part of the Bloch functions at $\mathbf{k} = 0$ and are ordered as $|3/2, 3/2\rangle$, $|3/2, 1/2\rangle$, $|3/2, -1/2\rangle$, $|3/2, -3/2\rangle$, $|1/2, -1/2\rangle$, $|1/2, 1/2\rangle$. In the absence of external fields functions like u_{10} and u_{40} are degenerate which can be proven by sequential application of the time and space inversion: $\hat{J}\hat{\theta}\,|3/2, 3/2\rangle = |3/2, -3/2\rangle$. The Hamiltonian in the new basis now reads

$$H_{6\times 6} = \begin{pmatrix} P_1 & L & M & 0 & iL/\sqrt{2} & -i\sqrt{2}M \\ L^\dagger & P_2 & 0 & M & -i\sqrt{2}Q & i\sqrt{3/2}L \\ M^\dagger & 0 & P_2 & -L & -i\sqrt{3/2}L & -i\sqrt{2}Q \\ 0 & M^\dagger & -L^\dagger & P_1 & -i\sqrt{2}M^\dagger & -iL^\dagger/\sqrt{2} \\ -iL^\dagger/\sqrt{2} & i\sqrt{2}Q & i\sqrt{3/2}L & i\sqrt{2}M & P + \Delta_{so} & 0 \\ +i\sqrt{2}M^\dagger & -i\sqrt{3/2}L^\dagger & i\sqrt{2}Q & iL/\sqrt{2} & 0 & P + \Delta_{so} \end{pmatrix} , \tag{3.20}$$

where the matrix elements of the Hamiltonian are given by

$$P = \frac{\hbar^2}{2m_0}\gamma_1 k^2,\; Q = \frac{\hbar^2}{2m_0}\gamma_2 (k^2 - 2k_z^2) , \tag{3.21a}$$

$$P_1 = P + Q \quad P_2 = P - Q , \tag{3.21b}$$

$$L = -i\frac{\sqrt{3}\hbar^2}{m_0}\gamma_3 \left(k_x - ik_y\right) k_z , \tag{3.21c}$$

$$M = \frac{\sqrt{3}\hbar^2}{2m_0}\left(\gamma_2 \left(k_x^2 - k_y^2\right) - 2i\gamma_3 k_x k_y\right) . \tag{3.21d}$$

3.2 KRAMERS THEOREM AND DEGENERACY OF BANDS

This subsection is concerned with the Kramers theorem that states that bands are doubly degenerate with respect to spin if the structure possesses inversion symmetry. This issue has recently become important in the field of spintronics especially in the case when an applied electric field spoils inversion symmetry and brings about different transmission amplitudes for spin-up and spin-down states. This effect is called Structural Inversion Asymmetry (SIA), and the corresponding term in the (mesoscopic) Hamiltonian Rashba term, named after its author. We start from the microscopic Hamiltonian

$$\hat{H}_{micro} = \frac{\mathbf{p}^2}{2m_0} + V(\mathbf{r}) + \frac{\hbar}{4m_0^2c^2}\sigma \cdot (\nabla V \times \mathbf{p}) \,. \tag{3.22}$$

The eigenfunctions of Eq. (3.22) have the Bloch form $\Psi_{\mathbf{k}} = e^{i\mathbf{kr}}u_{\mathbf{k}}$, with the eigenvalues $E(\mathbf{k})$. Since the microscopic Hamiltonian is time invariant, it commutes with the time reversal operator $\hat{\theta} = \sigma_y\hat{K}$, ($K$ is the complex conjugation operator):

$$\hat{\theta}\hat{H}\Psi_{\mathbf{k}} = E(\mathbf{k})(\sigma_y\Psi^*_{\mathbf{k}}) = \hat{H}\hat{\theta}\Psi^*_{\mathbf{k}} = \hat{H}(\sigma_y\Psi^*_{\mathbf{k}}) \,. \tag{3.23}$$

Therefore $\sigma_y\Psi^*_{\mathbf{k}}$ is an eigenfunction of $\hat{H}$ with eigenvalue $E(\mathbf{k})$. On the other hand $\sigma_y\Psi^*_{\mathbf{k}} = e^{-i\mathbf{kr}}w_{\mathbf{k}}(\mathbf{r})$, and $\sigma_y\Psi^*_{\mathbf{k}}$ is an eigenstate with wavevector $-\mathbf{k}$ and opposite spin, which yields an important relation

$$E(\mathbf{k},\uparrow) = E(-\mathbf{k},\downarrow) \,, \tag{3.24}$$

which holds regardless whether the system possesses inversion symmetry or not. In case the system is invariant under space inversion $J(\mathbf{r} \rightarrow -\mathbf{r})$, one should look at the equation satisfied by $u_{\mathbf{k}}$ as given by Eq. (3.4). Upon acting J on Eq. (3.4) one arrives at

$$\left\{ \frac{\mathbf{p}^2}{2m_0} + V(-\mathbf{r}) + \frac{\hbar}{4m_0^2c^2}(\sigma \times \nabla V(-\mathbf{r})) \cdot \mathbf{p} + \frac{\hbar^2k^2}{2m_0} - \frac{\hbar\mathbf{k}}{m_0} \cdot [\mathbf{p} + \frac{\hbar}{4m_0c^2}(\sigma \times \nabla V(-\mathbf{r}))] \right\} u_{\mathbf{k}} = E_{\mathbf{k}}u_{\mathbf{k}} \,,$$

taking into account that the operator has the following effect: $J : \mathbf{p} \rightarrow -\mathbf{p}, \nabla_{\mathbf{r}} \rightarrow -\nabla_{\mathbf{r}}$. As assumed $V(\mathbf{r}) = V(-\mathbf{r})$, and the last equation is the differential equation for $u_{-\mathbf{k}}(\mathbf{r})$ which means

$$u_{-\mathbf{k}}(\mathbf{r}) = u_{\mathbf{k}}(-\mathbf{r}) \,. \tag{3.25}$$

On the other hand, the Bloch function $u_{-\mathbf{k}}(\mathbf{r})$ corresponds to the energy $E(-\mathbf{k})$ and it has been proven to be equal to $E(\mathbf{k})$. As a consequence there are two different Bloch functions $u_{-\mathbf{k}}(\mathbf{r})$, $u_{\mathbf{k}}(-\mathbf{r})$ that correspond to the same energy. This completes the proof of Kramers theorem that states there is double degeneracy of bands when the crystal structure has inversion symmetry. In case of zinc-blend semiconductors like GaAs and AlAs it is assumed that inversion symmetry is approximately satisfied due to small difference in the constituent atoms. This difference, commonly named bulk inversion asymmetry (BIA), can be taken into account by introducing off-diagonal terms in the Hamiltonian. However, the splitting of bands is of the order of several meV, and is usually neglected especially when other sources of asymmetry are present. Presence of external magnetic or/and electric field, or strain lifts the degeneracy and this will be shown in the next sections.

3.3 HOLE MAGNETOTUNNELING THROUGH SINGLE AND DOUBLE BARRIERS

The semiconductors GaAs and AlAs are among the most studied materials within the III-V binary compounds. In case of both GaAs and AlAs the split-off (SO) band lies sufficiently below the Γ_8 point, and the 4×4 Luttinger-Kohn (LK) Hamiltonian is sufficiently accurate to explain the behavior of the holes (at least in the vicinity of $\mathbf{k}=\mathbf{0}$), and reads[110]

$$H=\begin{pmatrix} P_1 & L & M & 0 \\ L^\dagger & P_2 & 0 & M \\ M^\dagger & 0 & P_2 & -L \\ 0 & M^\dagger & -L^\dagger & P_1 \end{pmatrix} + V(z)I_4 - 2\kappa_0\mu_B\mathbf{J}\cdot\mathbf{B}\,, \tag{3.26}$$

where the matrix elements are given by Eq. (3.21).

Here γ_i are the well known Luttinger parameters (extracted from experiment) and κ_0 is an additional phenomenological parameter describing the coupling of the hole with an external magnetic field. The basis eigenfunctions $\{|j,j_z\rangle\}$ ($j=3/2$) are ordered as $\{|3/2,3/2\rangle,\ |3/2,1/2\rangle,\ |3/2,-1/2\rangle,\ |3/2,-3/2\rangle\}$. The axis of quantization of the angular momentum $\mathbf{J}$ is chosen to be along the growth direction[114, 118], for instance z, and hence $k_z\rightarrow\hat{k}_z=-i\partial_z$. The off-diagonal terms L and M cause the mixing of heavy and light holes for finite in-plane momentum k_x, k_y.

In the presence of a magnetic field, the wavectors k_i must be replaced by $k_i - eA_i/\hbar$, $i=x,y,z$, and they no longer commute. It was already noticed in the beginning of the development of the theory [104], that in order to preserve the hermicity of the Hamiltonian a symmetrized combination of the wavevectors $k_ik_j\rightarrow 1/2(k_ik_j+k_jk_i)$ must be used in the matrix elements in Eq. (3.21). Now, in order to rewrite the Hamiltonian in a form suitable for numerical calculations one should normally move the operator $\hat{k}_z=-i\partial_z$ to the rightmost place[115], which leads to an extra term in the Hamiltonian

$$H=H_0+\begin{pmatrix} 0 & K & 0 & 0 \\ K & 0 & 0 & 0 \\ 0 & 0 & 0 & -K \\ 0 & 0 & -K & 0 \end{pmatrix}, \tag{3.27}$$

where H_0 is the LK Hamiltonian in which $\hat{k}_z$ stands always at the rightmost end in the off-diagonal terms $\pm L$, $\pm L^\dagger$ (and thus using complex conjugation instead of hermitian conjugation). The term K is equal to $1/2[\hat{k}_z, L_1]$, where L_1 is the factor in L (Eq. (3.21c)) in front of $\hat{k}_z$. We assume that the external leads of the structure are not affected by the magnetic field (only by the vector potential $\mathbf{A}$) and the solution of the Schrödinger equation $H\Psi=E\Psi$ in bulk with $\mathbf{B}=\mathbf{0}$, is a linear combination of the following plane waves

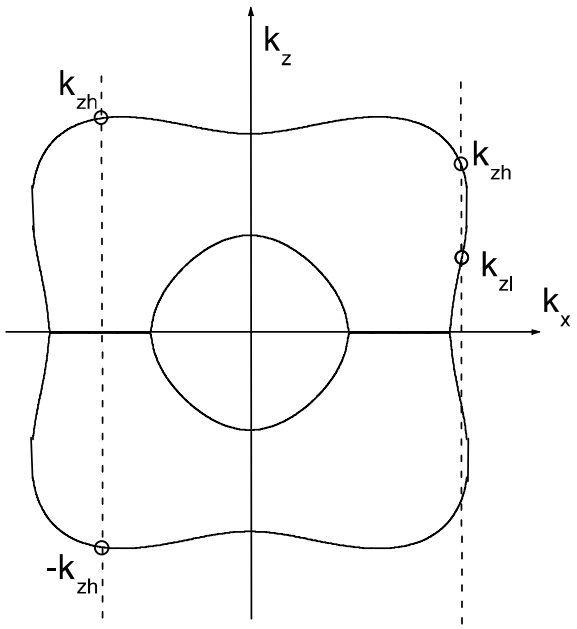

Fig. 3.4 Constant energy diagram for light and heavy holes determined by Eq. (3.29), at $k_y = 0$. For certain k_x (right vertical dashed line) all solutions lie on the heavy hole branch (the outer contour), the case (iii), with light holes having negative slope $\nabla_{\mathbf{k}} E(\mathbf{k})$. The left vertical dashed line shows case (ii) in the text, where the heavy hole propagates, while the light holes have evanescent wavefunctions.

$$\Psi(\mathbf{r}) = e^{i(k_x x + k_y y)} \sum_{i=1,8} a_i^{(L,R)} \cdot \begin{pmatrix} F_1 \\ F_2 \\ F_3 \\ F_4 \end{pmatrix} e^{ik_{zi} z} \,. \tag{3.28}$$

Here $(F_1, F_2, F_3, F_4)^T = V_i$ represents the 4-column eigenvectors (see e.g. Ref. [119]) of the Hamiltonian at the same energy E, and the wavevector k_z classifies the states of heavy and light holes. The eigenvectors V_i should be normalized to unity to ensure that the coefficients $a_i^{(L,R)}$ be directly proportional to the probability current density of the particular channels, i.e. to transmission (reflection) coefficients. This is particularly important if there is an applied bias across the structure, when even transmission of holes of the same kind must be normalized by the group velocity. In so doing, care must be taken during evaluation of the hermitian conjugate of an eigenvector $V_i^\dagger = (F_1^*, F_2^*, F_3^*, F_4^*)$, that whenever a term contains k_z, it must be kept

unchanged[119], i.e. $\{F_k(k_z)\}^* = F_k^*(k_z)$ even when it is a complex number. This is the consequence of the fact that the corresponding operator $-i\partial_z$ is hermitian and the value of the wavevector k_z is determined by the following biquadratic equation.

$$\epsilon = \gamma_1 k^2 \pm \sqrt{4\gamma_2^2 k^4 + C^2(k_x^2 k_y^2 + k_y^2 k_z^2 + k_z^2 k_x^2)}\,, \tag{3.29}$$

where $\epsilon = 2m_0(E-V)/\hbar^2$ is the normalized energy in the flat potential regions, and $C^2 = 12(\gamma_3^2 - \gamma_2^2)$. The plus (minus) sign corresponds to light (heavy) holes. Depending on the energy and values of the in-plane momenta k_x, k_y, the solution of Eq. (3.29) with respect to k_z can have the following properties:

1. $\epsilon > \epsilon_{c4}$, all k_{zh} and k_{zl} are real,
2. $\epsilon_{c4} > \epsilon > \epsilon_{c3}$, k_{zh} is real, and k_{zl} purely imaginary,
3. $\epsilon_{c3} > \epsilon > \epsilon_{c2}$, k_{zh} and k_{zl} are real,
4. $\epsilon_{c2} > \epsilon > \epsilon_{c1}$, k_{zh} and k_{zl} are complex,
5. $\epsilon < \epsilon_{c1}$, all k_{zh} and k_{zl} are purely imaginary,

where

$$\epsilon_{c1} = \frac{1}{2\gamma_2^2}\Big(-3\gamma_1(\gamma_3^2-\gamma_2^2)k_\parallel^2 - \big\{3(\gamma_1^2-4\gamma_2^2)(\gamma_3^2-\gamma_2^2) \Big[(3\gamma_3^2+\gamma_2^2)k_\parallel^4 - 4\gamma_2^2 k_x^2 k_y^2\Big]\big\}^{1/2}\Big)\,, \tag{3.30a}$$

$$\epsilon_{c2} = \frac{1}{2\gamma_2^2}\Big(-3\gamma_1(\gamma_3^2-\gamma_2^2)k_\parallel^2 + \big\{3(\gamma_1^2-4\gamma_2^2)(\gamma_3^2-\gamma_2^2) \Big[(3\gamma_3^2+\gamma_2^2)k_\parallel^4 - 4\gamma_2^2 k_x^2 k_y^2\Big]\big\}^{1/2}\Big)\,, \tag{3.30b}$$

$$\epsilon_{c3} = \gamma_1 k_\parallel^2 - \Big(4\gamma_2^2 k_\parallel^4 + 12(\gamma_3^2-\gamma_2^2)k_x^2 k_y^2\Big)^{1/2}\,, \tag{3.30c}$$

$$\epsilon_{c4} = \gamma_1 k_\parallel^2 + \Big(4\gamma_2^2 k_\parallel^4 + 12(\gamma_3^2-\gamma_2^2)k_x^2 k_y^2\Big)^{1/2},\ k_\parallel^2 = k_x^2 + k_y^2\,. \tag{3.30d}$$

The most interesting case is (iii) when all (real) solutions lie on the heavy hole branch (see Fig. 3.4). Due to its warped structure the nominally classified light hole states (with smaller k_z) have group velocity with opposite sign than that of its phase velocity. It is important to bear this in mind during the calculation of the transmitivity T and reflectivity R coefficients, because they are normalized by the probability density current, i.e. by the group velocity:

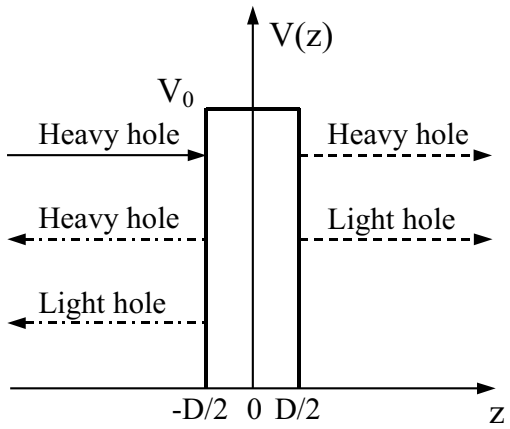

Fig. 3.5 A heavy hole impinging on a barrier can transmit (reflect) as a heavy hole or as a light hole on the right (left) side due to band mixing in the barrier (similarly for a light hole).

$$T_{\lambda\mu} = \frac{|a_\mu^{(R)}|^2}{|a_\lambda^{(L)}|^2} \cdot \frac{j_{z0\mu}^{(R)}}{j_{z0\lambda}^{(L)}} = |t_{\lambda\mu}^0|^2 \cdot \frac{v_{z\mu}^{(R)}}{v_{z\lambda}^{(L)}}\,, \tag{3.31a}$$

$$R_{\lambda\mu} = \frac{|a_\mu^{(L)}|^2}{|a_\lambda^{(L)}|^2} \cdot \frac{j_{z0\mu}^{(L)}}{j_{z0\lambda}^{(L)}} = |r_{\lambda\mu}^0|^2 \cdot \frac{v_{z\mu}^{(L)}}{v_{z\lambda}^{(L)}}\,. \tag{3.31b}$$

Here

$$v_{zh,l} = \frac{\hbar k_{zh,l}}{m_0} \frac{(\gamma_1^2 - 4\gamma_2^2)k^2 - 6(\gamma_3^2 - \gamma_2^2)k_\parallel^2 - \gamma_1\epsilon}{\gamma_1 k^2 - \epsilon}\,, \tag{3.32}$$

is the group velocity of both heavy and light holes $v_z = \hbar^{-1}\partial E/\partial k_z$. It was proven[120], that it is directly proportional to the probability current density even in case of degenerate bands $\mathbf{j} = \rho\mathbf{v}(\mathbf{k})$, which justifies using v_z instead of j_{z0} in Eqs. (3.31), as $\rho_0 = V_i^\dagger V_i = 1$. Furthermore, since the LK Hamiltonian describes a hole in 4 possible states (the two light and the two heavy hole states) there are four channels possible and due to band mixing, for instance, a heavy hole passing through the barrier can end up as either a heavy hole or a light hole with certain probabilities determined by the Schrödinger equation (see Fig. 3.5). The difference in the velocities of light and heavy hole outside the barrier must be accounted for, during this conversion, as was already done in Eq. (3.33). Therefore, the conservation of the probability current $div\mathbf{j} = 0$ leads to four relations among the transmission and reflection coefficients

$$R_{\lambda h_1} + R_{\lambda h_2} + R_{\lambda l_1} + R_{\lambda l_2} + T_{\lambda h_1} + T_{\lambda h_2} + T_{\lambda l_1} + T_{\lambda l_1} = 1. \tag{3.33}$$

Here the variable λ assumes all four states (h_1, h_2, l_1, l_2). These relations are also useful to check the consistency of the numerical calculations. However, for certain values of the in-plane momentum k_x, k_y the wavevector k_{zl} of the light hole is purely imaginary (case (ii), see Fig. 3.4), i.e. their wavefunctions are evanescent. The quantity $Re(\Psi^\dagger \hat{j}_z \Psi)$ can no longer be related to the particle flux, and one should put by hand $T_{\lambda l} = 0$, and $T_{l\mu} = 0$ (for both light holes $l = l_1, l_2$), as well as for the corresponding power reflection coefficients. Therefore the conservation relations Eq. (4.12) reduce to only two

$$R_{\lambda h_1} + R_{\lambda h_2} + T_{\lambda h_1} + T_{\lambda h_2} = 1, \quad \lambda \in \{h_1, h_2\}\,. \tag{3.34}$$

However it may happen that under a positive bias, and for some (k_x, k_y), the light holes have propagating states only in the right lead, so that Eq. (4.12) turns into

$$R_{\lambda h_1} + R_{\lambda h_2} + T_{\lambda h_1} + T_{\lambda h_2} + T_{\lambda l_1} + T_{\lambda l_2} = 1\,. \tag{3.35}$$

for $\lambda \in \{h_1, h_2\}$.

3.3.1 Numerical method

The major difference between tunnelling phenomena and e.g. treatment of bound states in semiconductor physics, from the numerical point of view, is that the boundary conditions are not known in advance in the former case. This is due to the presence of reflected waves, whose amplitude is yet to be found and the traditional method to tackle it, has been the transfer matrix method as developed earlier to treat analog problems in classical optics. An alternate way was developed by Frensley[121] for electrons and then later by Liu and coworkers[113] for holes i.e. for the case of degenerate bands, now called multiband quantum transmitting boundary method (MQTBM) where the problem is solved by a method similar as in a finite difference scheme but here adapted for the propagating states. The basic idea of the MQTBM method is to add an extra layer in the left lead, still in the flatband region, in order to eliminate the unknown reflection coefficients. However we treat the problem as a set of coupled differential equations, which is solved by the Adams method[122] (it belongs to the class of predictor-corrector methods). The procedure was originally outlined and explained in Ref. [110] and it will be repeated briefly here. It exploits the superposition principle in the solution of the Schrödinger equation. Let us define the matrix M that connects output and input channels, i.e. the coefficients of expansion in Eq. (3.28)

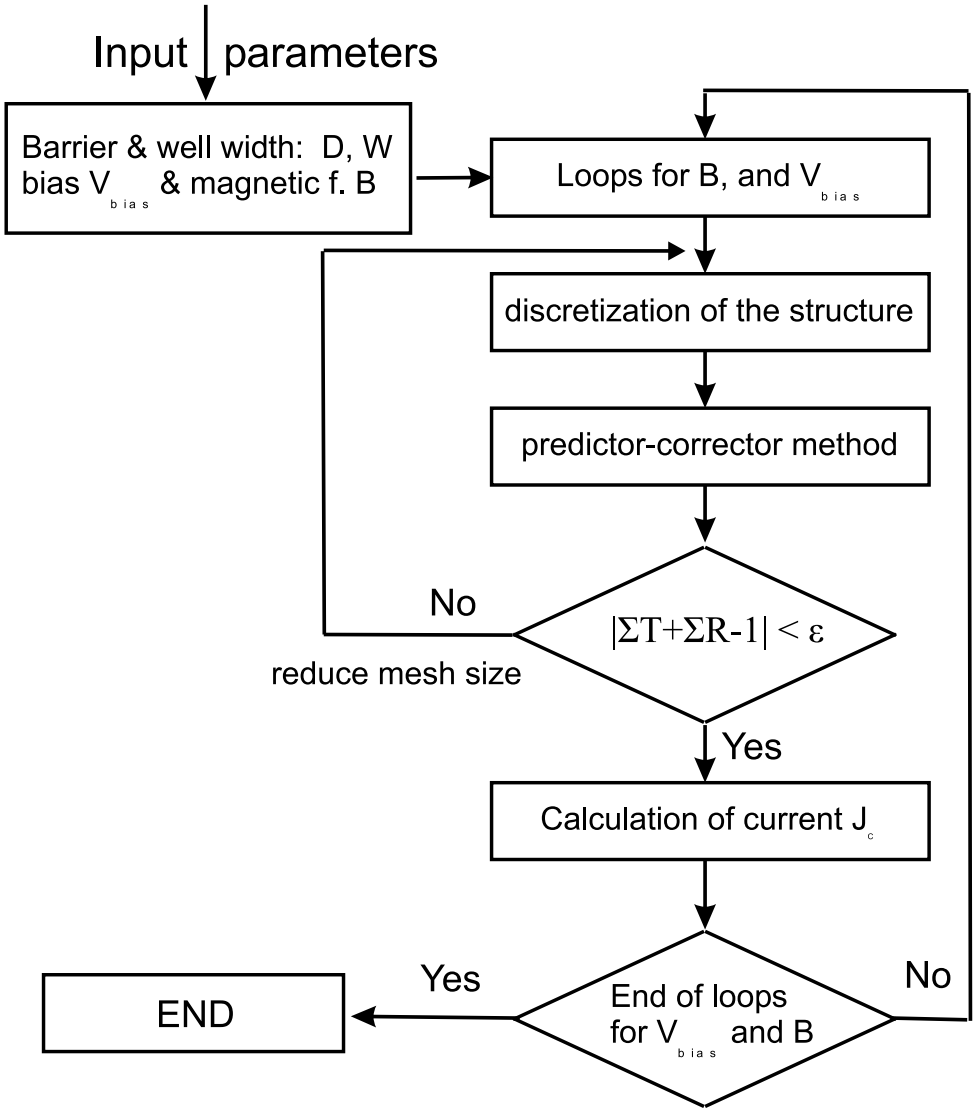

Fig. 3.6 Flowchart of calculations. The consistency and accuracy of calculation is checked by the conservation of probability current (sum of reflection and transmission coefficients). If it is not satisfied within predefined tolerance, the mesh size is reduced.

$$\begin{pmatrix} a_{h1} \\ a_{h2} \\ a_{l1} \\ a_{l2} \\ r_{h1} \\ r_{h2} \\ r_{l1} \\ r_{l2} \end{pmatrix} = M \cdot \begin{pmatrix} t_{h1} \\ t_{h2} \\ t_{l1} \\ t_{l2} \\ 0 \\ 0 \\ 0 \\ 0 \end{pmatrix} . \tag{3.36}$$

Note that the matrix M connects the coefficients from the right flatband region to the left, in the opposite direction than that in the TMM method. Now if we put $t_\lambda = 1$ for some $\lambda \in (h_1, h_2, l_1, l_2)$ and take the others zero (on the right lead) then we know the boundary conditions on the right side of the barrier, since there are no reflected waves. These are sufficient to solve the set of coupled equations arising from the 4×4 LK Hamiltonian, going *backward* to the left lead by discretizing the structure by a mesh with step $h = \Delta z = D/N$, where D is the barrier width. Then the solution, obtained by numerical integration is decomposed on the *left* side as a linear combination, likewise Eq. (3.28) of *normalized* eigenfunctions to obtain the coefficients a_i^L. These are actually the entries, or more precisely, λ^{th} column of the matrix M, since $t_\lambda = 1$. Upon repeating the whole procedure for each four outgoing states, one finds all entries in the left-half of the matrix, which we denote by two 4×4 submatrices, M^U, M^L

$$M = \begin{pmatrix} M^U & * \\ M^L & * \end{pmatrix} . \tag{3.37}$$

The right half of M is not important due to the absence of reflected waves on the right side of the barrier, i.e. due to zeros in the outgoing vector in Eq. (3.36). It can be easily proven that

$$T_{ij} = |N_{ji}|^2 \frac{v_{zj}^{(R)}}{v_{zi}^{(L)}}, \;\; R_{ij} = \left| \sum_{k=1,4} N_{j,k} M_{k,i}^L \right|^2 \frac{v_{zj}^{(L)}}{v_{zi}^{(L)}} , \tag{3.38}$$

where $i, j \in \{1, 2, 3, 4\} = \{h_1, h_2, l_1, l_2\}$, $N = (M^U)^{-1}$. The major advantage of the method presented here is that the calculation time increases linearly with the number of mesh points N, i.e. when the step h is diminished, in contrast with the MQTBM where it increases as $O(N^2)$, as the order of the matrix equation that has to be solved is $4(N + 3)$. The flowchart of calculation is given on Fig. 3.6, where it is indicated that a loop is inserted to check whether the sum of all transmission and reflection coefficients are close to 1 within predefined accuracy.

3.3.2 Transmission and reflection coefficients: Single barrier

The theory will be applied to the case of a barrier made of $Al_{0.2}Ga_{0.8}As$ which is embedded in GaAs. The barrier width is taken to be $D = 25$ Å, the barrier height, i.e. the valence band mismatch between the two materials is $V_0 = 95meV$, and the Luttinger parameters are $\gamma_1^a = 6.85$, $\gamma_2^a = 2.1$, $\gamma_3^a = 2.9$, (GaAs); and $\gamma_1^b = 3.45$, $\gamma_2^b = 0.68$ $\gamma_3^b = 1.29$ (AlAs) (linear interpolation of γ_i was used for the alloy $Al_xGa_{1-x}As$). The Fermi energy is taken to be $E_F = 10meV$. In the absence of a magnetic field the wavevectors k_x, k_y, k_z commute with each other and the term K equals zero. The in-plane wavevector $\mathbf{k}_\parallel = (k_x, k_y)$ is still a good quantum number when inelastic processes at the interfaces are neglected. The difference in the Luttinger parameters $\gamma_2 \neq \gamma_3$ causes anisotropy in the plane parallel to the interfaces and it will be then important to investigate the dependence $T_{\lambda\mu}$ on the in-plane momentum $\mathbf{k}_\parallel = (k_x, k_y)$. A contour-plot of the transmission amplitude $T_{h_1h_1}(k_x, k_y)$ between the two heavy holes is shown in Fig. 3.8. There is a clear anisotropy in the dispersion relation $E(k_x, k_y)$ as reflected in this graph. For small k_x and k_y the contour lines resemble circles as band mixing is less pronounced. However as the in-plane momentum is increased beyond the first critical value $k_\parallel \approx \sqrt{\epsilon/(\gamma_1 + 2\gamma_2)}$ (when the light holes become evanescent) the contour lines become more distorted. The deviation from isotropic shape is maximal when k_x, k_y lie in the region (iii), i.e. when all solutions lie on the heavy

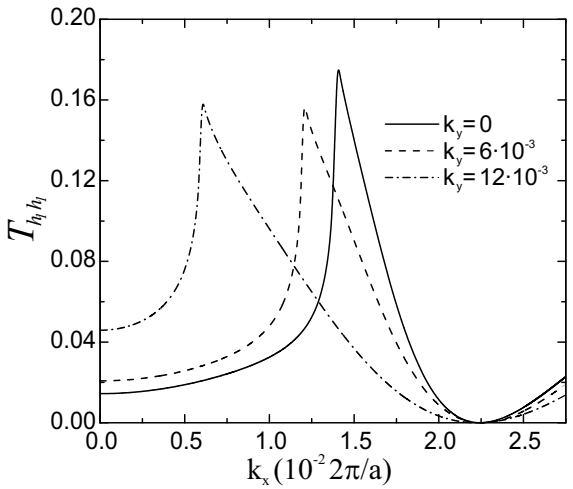

Fig. 3.7 Transmission coefficient $T_{h_1h_1}$ for heavy holes as a function of k_x for three different values of k_y: 0.0 (solid line), $6 \cdot 10^{-3} \times 2\pi/a$ (dashed), and $12 \cdot 10^{-3} \times 2\pi/a$ (dot-dash). The energy is $E = 10meV$

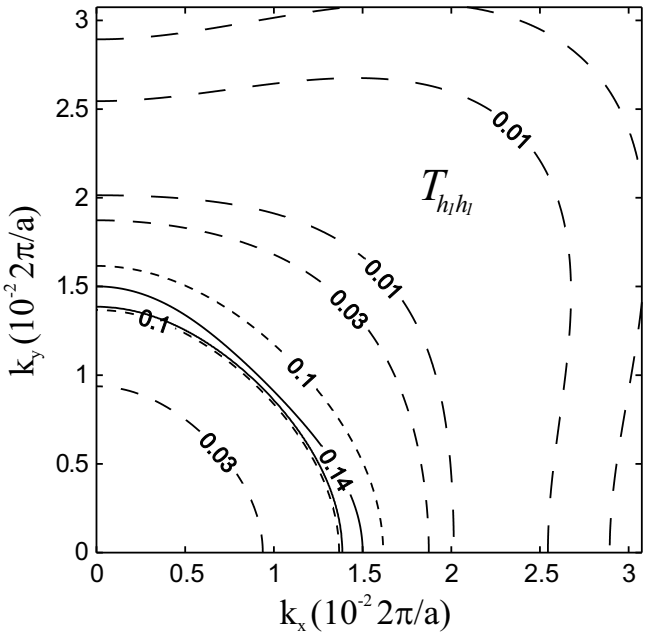

Fig. 3.8 Contour diagram of the transmission coefficient $T_{h_1h_1}$ for heavy holes of the same kind with energy $E = 10meV$, in units of reciprocal vector $2\pi/a$. Due to Kramer's degeneracy the graph is identical to $T_{h_2h_2}$.

hole branch. The latter is expected since the dispersion relation has now a pronounced warped structure. In this case the term $C^2k_x^2k_y^2$ becomes dominant in the dispersion relation, when both k_x and k_y are large, which makes the wavevector k_z small and the transmission coefficient $T_{h_1h_1}$ attains very small values below 10^{-2}, presented by the dashed lines in the corners of the graph of Fig. 3.8. Now in order to understand better the contour graph, it is also instructive to have a look at the dependence $T_{h_1h_1}(k_x)$ at fixed k_y, which is given in Fig. 3.7 for three different values of $k_y/(2\pi/a)$: 0.0 (solid line) $6 \cdot 10^{-3}$ (dashed), and 0.012 (dash-dotted). Due to band mixing the transmission coefficient of the heavy holes increases with k_x which is opposite to the predictions of the simple one-band picture. This increase continues as long as the propagating states of the light holes exist, as is so for case (i): the peaks in the graph for different k_y indeed correspond to the critical energy ϵ_{c4} (Eq. (3.30d)). Beyond the maximum, it decreases and begins to increase again when values of (k_x, k_y) are large enough for the 'light holes' to become propagating. It was noticed[109, 123] previously that the heavy hole tunnelling times through double barrier structures are significantly shorter

than can be concluded from their mass $m_{hh} = m_0/(\gamma_1 - 2\gamma_2)$ at $\mathbf{k}_\parallel = 0$. Yu et al.[109] attributed this discrepancy to band mixing in the sense that heavy holes in a barrier acquire somewhat of a light-hole character, having lighter mass, and thus enhancing the tunnelling of the heavy holes[115]. Their results were obtained from the 4×4 LK model, as used in the present paper as well, and are in good agreement with the experimental results of Ref. [123].

Since the heterostructure has inversion symmetry (in the absence of an applied bias) the two heavy hole states (and the two light hole states) are degenerate (Kramer's degeneracy) and hence the corresponding coefficients are identical, so that it will suffice to show only $T_{l_1 l_1}$ $(= T_{l_2 l_2})$ and $T_{h_1 l_1}$ $(= T_{h_2 l_2})$, which are given in Figs. 3.9(a,b). The transmission coefficient between the two light holes as a function of k_x, k_y is more isotropic than that of the heavy holes since their propagating states exist only for relatively small $k_\parallel < \sqrt{\epsilon/(\gamma_1 + 2\gamma_2)}$. The values of $T_{l_1 l_1}$ are larger than that of $T_{h_1 h_1}$, since the light holes transmit through the barrier more easily due to their lighter mass. The transmission coefficients $T_{h_1 h_2}$ and $T_{l_1 l_2}$ vanish identically due to zeros on the side diagonal in the Hamiltonian. We find that the conservation relations (4.12) and (3.34) are always fulfilled in contrast to what was found in Ref. [120], even in the case (iii), when the light holes propagate in the opposite direction than the phase velocity. In this case one should either assume $T'_{h,l} = -R_{h,l}$ and $R'_{l,h} = -T_{l,h}$ or choose[120], a negative value for k_z for light holes.

Next we will give the reflection coefficients. There is a difficulty to represent them transparently on a contour graph since many values are concentrated near unity. However, we choose to present contour lines for 0.01, 0.03, 0.2, and 0.6. The reflection from a heavy to a heavy hole (with the same sign of j_z) is given in Fig. 3.10(a). Total reflection occur for large values of (k_x, k_y) when the propagation wavevector k_z is too small to ensure efficient tunnelling. In the next figure, Fig. 3.10(b), one can see that a heavy hole can reflect as a light hole (but with a negative group velocity) which is denoted by dashed lines in the corners of the graph. For moderate values of the in-plane momentum (around $0.02 \cdot 2\pi/a$) there is no reflection as light holes then do not exist. Finally the reflection coefficient as a function of (k_x, k_y) from a light hole to a light hole is presented in Fig. 3.10(c).

When the magnetic field is in-plane, i.e. parallel to the interfaces, but acting only in the barrier region, i.e. $z \in (-D/2, D/2)$ and aligned along the x-axis the wavevectors k_x, k_y, k_z no longer commute. For the case of the commonly used Landau gauge $\mathbf{A} = (0, -Bz, 0)$ the term Q contains both non-commuting z and $\hat{k}_z$, and the term K is equal to $K = i\sqrt{3}\hbar/(2m_0)\gamma_3 eB$. The vector potential component A_y is constant outside the barrier $A_y(z < -D/2) = +BD/2$, $A_y(z > +D/2) = -BD/2$ and except for the constant shift in the wavevector $k_y = k_y^0 - eA_y/\hbar = k_y^0 + eBz/\hbar$, the solution in the external leads are similar to the nonmagnetic case (Eq. (3.28))

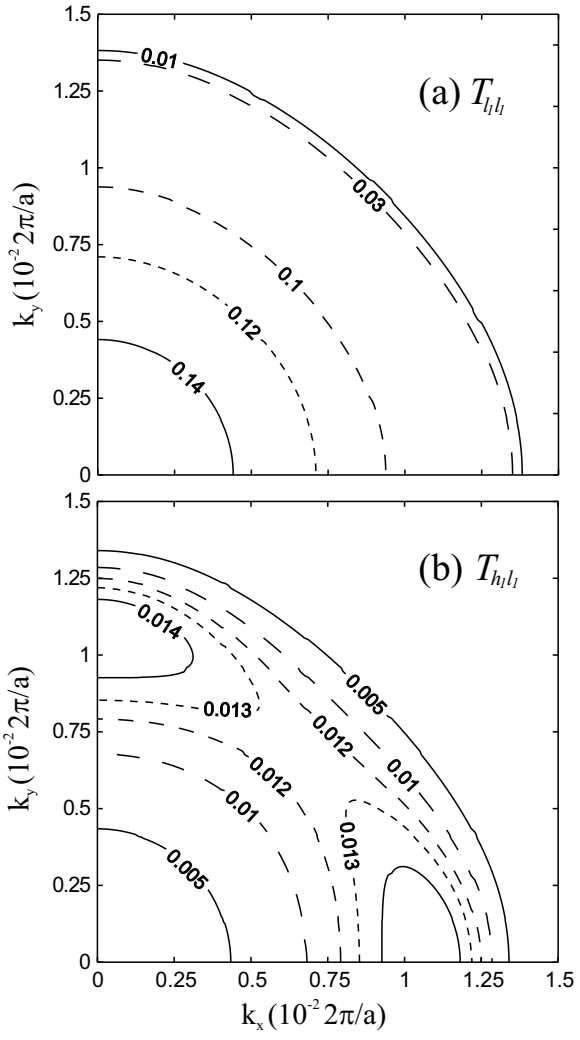

Fig. 3.9 Contour diagram of the transmission coefficient (a) $T_{l_1 l_1}$ for light holes of the same kind (due to Kramer's degeneracy the graph is identical to $T_{l_2 l_2}$), and (b) $T_{h_1 l_1}$ from the heavy to the light holes, in units of reciprocal vector $2\pi/a$, for the energy $E = 10meV$.

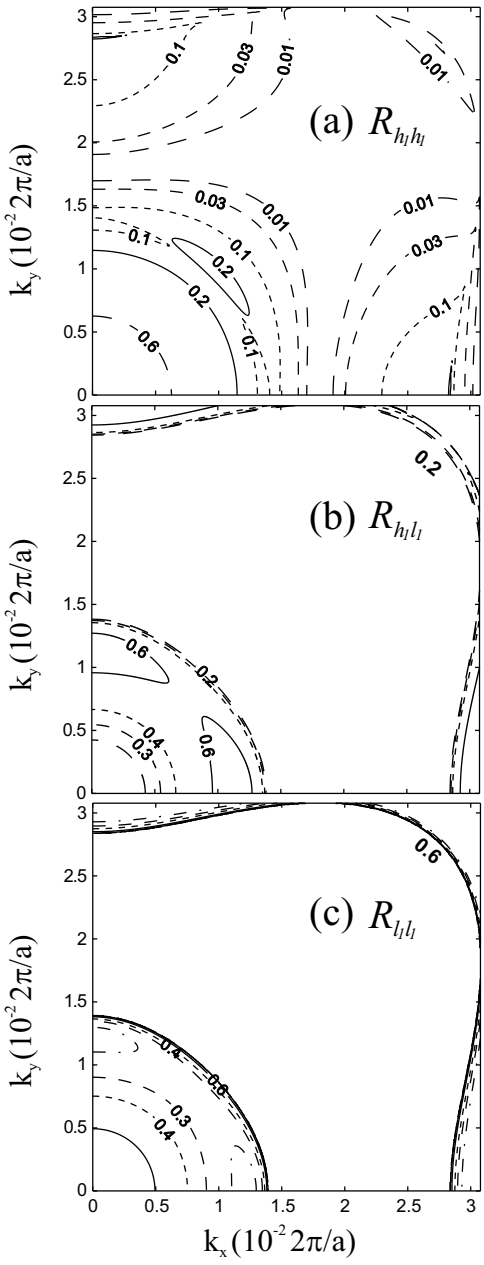

Fig. 3.10 Contour diagram of reflection coefficients: (a) $R_{h_1 h_1}$ for heavy holes of the same kind (due to Kramer's degeneracy the graph is identical to $R_{h_2 h_2}$), (b) $R_{h_1 l_1}$ from the heavy holes to the light holes, and (c) $R_{l_1 l_1}$ from a light hole to a light hole with the same $J_z = 3/2$ in units of reciprocal vector $2\pi/a$. The energy is $E = 10meV$.

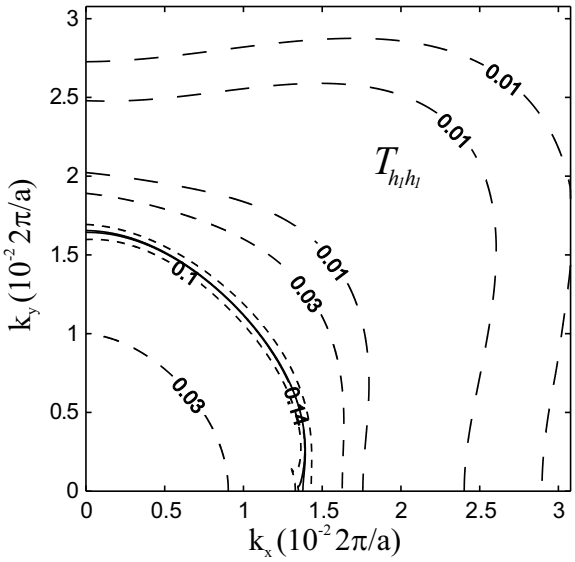

Fig. 3.11 Contour diagram of the transmission coefficient $T_{h_1 h_1}$ of the heavy holes of the same kind, in units of reciprocal vector $2\pi/a$, when magnetic field $B = 15T$ is applied along the x-axis parallel to the interfaces. The energy of the holes is $E = 10meV$.

$$\Psi(\mathbf{r}) = e^{i(k_x^0 x + k_y^0 y)} \sum_{i=1,8} a_i^{(L,R)} \cdot \begin{pmatrix} F_1 \\ F_2 \\ F_3 \\ F_4 \end{pmatrix} e^{ik_{zi} z}. \tag{3.39}$$

The quantities k_x^0, k_y^0 are canonical momenta associated with the translational invariance and therefore good quantum numbers throughout the structure[114, 124]. However within the barrier, where $\mathbf{B} \neq 0$, the third term in the Hamiltonian Eq. (3.26) introduces off-diagonal terms due to the matrix J_x that represents the projection of the angular momentum on the x-axis

$$J_x = \begin{pmatrix} 0 & \sqrt{3}i/2 & 0 & 0 \\ -\sqrt{3}i/2 & 0 & i & 0 \\ 0 & -i & 0 & \sqrt{3}i/2 \\ 0 & 0 & -\sqrt{3}i/2 & 0 \end{pmatrix}. \tag{3.40}$$

Now the transmission between the two light holes (with opposite projection $j_z = \pm 1/2$) becomes possible thanks to the presence of the magnetic field. In other words the quantity j_z is no longer a conserved quantum number since

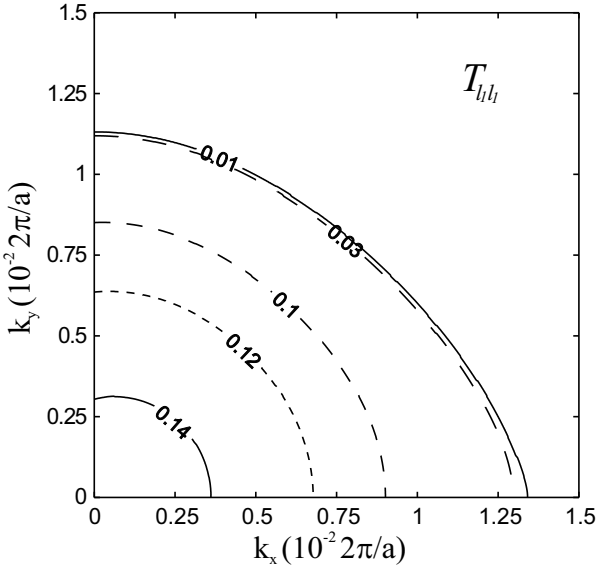

Fig. 3.12 Contour diagram of the transmission coefficient $T_{l_1 l_1}$ for light holes of the same kind, in units of reciprocal vector $2\pi/a$, when magnetic field $B = 15T$ is applied along the x-axis parallel to the interfaces. The energy is $E = 10meV$.

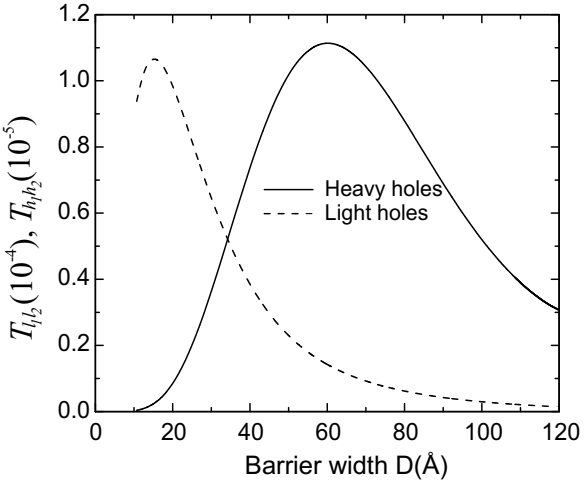

Fig. 3.13 Transmission coefficient $T_{l_1 l_2}$ between the two light hole states (solid line), and heavy hole states $T_{h_1 h_2}$ (dashed) as a function of barrier width D. The magnetic field strength is $B = 15T$, and the energy is $E = 10meV$.

J_z does not commute with J_x, and holes undergo an angular momentum precession. In Fig. 3.11 the contour plot of the transmission coefficient $T_{h_1h_1}$ is shown for magnetic field strength $B = 15T$. When compared with Fig. 3.8 we see that the magnetic field enhances the anisotropy. Analogue results for $T_{l_1l_1}$ are shown in Fig. 3.12. To demonstrate the precession of the hole spin in the barrier we present the transmissions $T_{l_1l_2}$ and $T_{h_1h_2}$ as a function of the barrier width D in Fig. 3.13. Normally the transmission between the states $j_z = +3/2$ (h_1) and $j_z = -3/2$ (h_2) is not possible at $k_\parallel = 0$ due to zeros in the corresponding terms in the Hamiltonian Eq. (3.26). However, mixing of heavy holes with the light holes lifts this selection rule[125] at finite $k_\parallel$. This can also be seen if one evaluates $j_z =< J_z >=< \Psi_h|\hat{J}_z|\Psi_h >$ for heavy holes, which turns into $j_z = V_h^\dagger J_z V_h$ for continuum states or $j_z = \int V_h^\dagger J_z V_h e^{-2\chi_z z} dz$, $k_z = i\chi_z$, for evanescent states. The expectation value of the angular momentum on the z-axis for the heavy holes axis decreases with $k_\parallel$ below the nominal value of $3/2$. This effect was already noticed out for bound states in quantum wells[126]. Thus one can not speak about pure heavy holes or light holes away from the center of the Brillouin zone. Since the tunnelling $T_{h_1h_2}$ is not a direct effect but is induced by band mixing, its value is smaller than that of $T_{l_1l_2}$, as can be seen from Fig. 3.13 (notice there is a factor of 10 difference in the used scale for $T_{l_1l_2}$ and $T_{h_1h_2}$).

3.3.3 Accuracy of the numerical methods

This subsection is concerned with the accuracy of the method used here and the accuracy of MQTBM mentioned earlier, when different numerical implementations of matching conditions at interfaces are used in the latter. It is, in principle, possible to derive analytical expressions for the transmission and reflection coefficients for the problem of a single barrier, but their forms are cumbersome, and we restrict ourselves to the final results. For the case of the method used here, we find that the average relative error obtained is $\delta_{max} = 0.15\%$, when using $N_{mp} = 20000$ mesh points. Now we turn our attention to the MQTBM method, where the system of differential equations are approximated into finite difference equations for each mesh point:

$$\mathbf{H}_{\sigma,\sigma+1}F_{\sigma+1} + \mathbf{H}_{\sigma,\sigma}F_\sigma + \mathbf{H}_{\sigma,\sigma-1}F_{\sigma-1} = 0, \tag{3.41}$$

with $\mathbf{H}_{\sigma\mu}$ being 4×4 numerical matrices. The boundary conditions on the interface proposed in Ref. [111] reads

$$\mathbf{H}_{\eta,\eta} = \frac{2(\mathbf{H}_R^{(2)} + \mathbf{H}_L^{(2)})}{h^2} - i\frac{\mathbf{H}_R^{(1)} - \mathbf{H}_L^{(1)}}{2h}, \tag{3.42a}$$

$$\mathbf{H}_{\eta,\eta+1} = -\frac{2\mathbf{H}_R^{(2)}}{h^2} - i\frac{\mathbf{H}_R^{(1)}}{2h}, \tag{3.42b}$$

$$\mathbf{H}_{\eta,\eta-1} = -\frac{2\mathbf{H}_L^{(2)}}{h^2} + i\frac{\mathbf{H}_L^{(1)}}{2h}\,. \tag{3.42c}$$

These forms of matrices are obtained when the condition $J_z F_L = J_z F_R$ is imposed on the wavevectors F_σ. Though mathematically not inconsistent, we find that a direct implementation of the continuity of wavefunction in our numerical calculation is not appropiate. For instance if one puts intentionally $\mathbf{H}_R^{(i)} = \mathbf{H}_L^{(i)}$ (as if there were no changes of materials at the interface) then Eq. (3.42a-3.42c) will not reduce to the layer element of a single material (see Eq. (21a-c) in Ref. [111]). Thus we propose the following forms for $\mathbf{H}_{\sigma\mu}$

$$\mathbf{H}_{\eta,\eta} = \frac{(\mathbf{H}_R^{(2)} + \mathbf{H}_L^{(2)})}{2h^2} + \frac{1}{2}(\mathbf{H}_R^{(0)} + \mathbf{H}_L^{(0)}) + V_\sigma - E, \tag{3.43a}$$

$$\mathbf{H}_{\eta,\eta+1} = -\frac{\mathbf{H}_R^{(2)}}{h^2} - i\frac{\mathbf{H}_R^{(1)}}{2h}, \tag{3.43b}$$

$$\mathbf{H}_{\eta,\eta-1} = -\frac{\mathbf{H}_L^{(2)}}{h^2} + i\frac{\mathbf{H}_L^{(1)}}{2h}. \tag{3.43c}$$

These forms of boundary conditions are obtained in similar manner to those for finite difference scheme[127], in order to symmetrize matrix elements that were derived from L, M elements of the Hamiltonian. When compared with analytical values for $T_{h_1 h_1}$, then the new matching relations (3.43a-3.43c) yield an average relative error $\delta_{av1} < 0.2\%$ for $N_{mp} = 300$, while the "old" relations (3.43a-3.43c) give $\delta_{av2} = 3\%$ for the same N_{mp} which is an improvement with more than a factor 10.

3.3.4 Resonant tunnelling

First we consider a simple case when carriers are electrons which can be described by a single band model. A typical double barrier resonant structure (DBRS) is given in Fig.3.14, that consists of two different semiconductors, one of which serves as a barrier. If one denotes t_1 and t_2 transmission probabilities through the first and the second barrier, r_1' reflection from the first barrier (on the right side, see Fig.3.14), r_2 from the second barrier, then the overall transmission t can be found by summing the geometrical sum arising from multiple reflection inside the well:

$$t = \frac{t_1 t_2 e^{i\phi}}{1 - e^{i2\phi} r_1' r_2} = \frac{t_1 t_2 e^{i\phi}}{1 - e^{i\theta}\sqrt{R_1 R_2}}\,, \tag{3.44}$$

where $\theta = 2\phi + arg(r_1' r_2)$, resulting in

$$T = \frac{T_1 T_2}{1 + R_1 R_2 - 2\sqrt{R_1 R_2}\cos\theta}\,. \tag{3.45}$$

The maximum for the transmittance is attained when $\cos\theta = 1$, and its value is

$$T_{max} = \frac{T_1 T_2}{(1 - \sqrt{R_1 R_2})^2}\,, \tag{3.46}$$

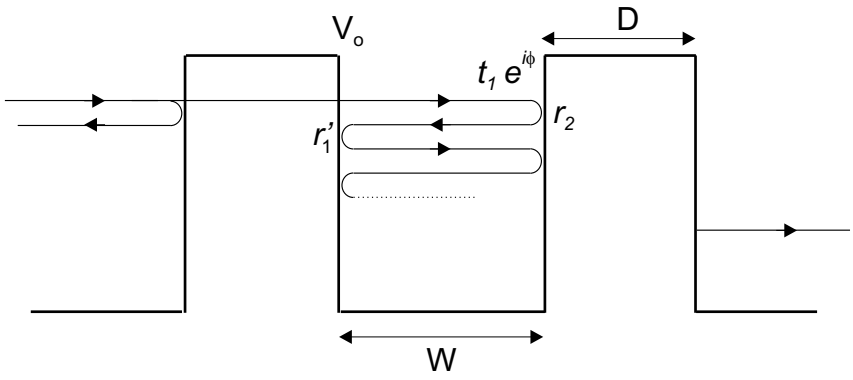

Fig. 3.14 Scheme of a double barrier (resonant) structure. Electron experiences several reflections (on average) in the well before leaving the structure. The change of the phase of the electron wavefunction should be taken into account. Note that the coefficient r_1' denotes reflection from the first barrier from the left side.

if the barriers are sufficiently wide, which is fulfilled in most practical cases, then the transmittances T_1, T_2 are much less than unity so that the following approximation $1 - \sqrt{R_1 R_2} \approx 1 - \sqrt{1 - (T_1 + T_2)} \approx 1/2(T_1 + T_2)$ may be employed. Then the expression (3.46) reduces to

$$T_{max} = \frac{4T_1 T_2}{(T_1 + T_2)^2} \,. \tag{3.47}$$

It is obvious from the last relation that the total transmittance may theoretically reach unity if DBRS is symmetrical, the barrier widths are sufficiently large, and if the condition $\theta = 2n\pi, n \in N$ is met. The last condition gives the values of the resonant energies

$$\cos\theta(E^{(r)}) = 1, \rightarrow \theta(E^{(r)}) = 2n\pi \,. \tag{3.48}$$

In order to gain more transparent information from the original expression for T it is convenient to expand the cosine function as

$$\cos\theta = 1 - \frac{1}{2}\left(\frac{\partial\theta}{\partial E}\right)^2 (E - E^{(r)})^2 \,, \tag{3.49}$$

and the formula for the transmittance reads

$$T \approx \frac{T_1 T_2}{\frac{1}{4}(T_1 + T_2)^2 + (\theta')^2 (E - E^{(r)})^2} = \frac{\Gamma_1 \Gamma_2}{\frac{1}{4}(\Gamma_1 + \Gamma_2)^2 + (E - E^{(r)})^2} \,. \tag{3.50}$$

In the last expression, the substitutions $\Gamma_i = T_i/|\theta'|$ are made so that it resembles the Breit-Wigner formula for resonant scattering. The physical

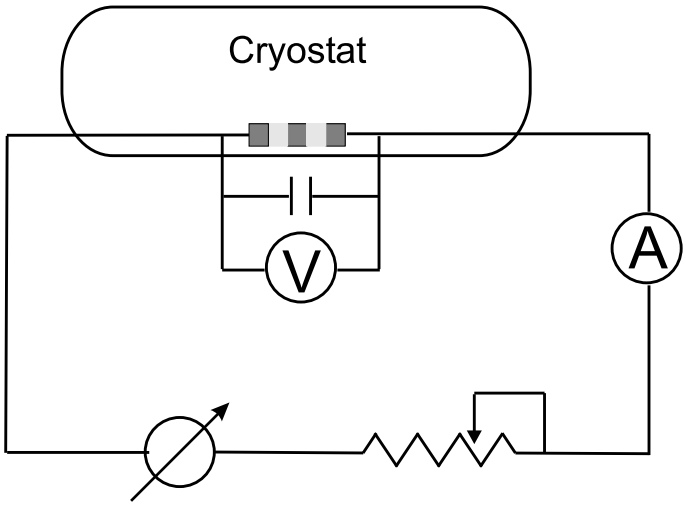

Fig. 3.15 Electrical scheme of the device to probe hole tunneling through double barrier resonant tunneling structure (diode). It is placed under cryostat containing either liquid helium or nitrogen. A small capacitor connected in parallel to the diode is needed to stabilize the voltage.

meaning of the quantities Γ_i is readily revealed if one assumes that all phase shift is due to the motion of carriers inside the quantum well. It can be easily shown that in this case $\Gamma_i = \hbar v/(2W)T_i$, where $\nu = v/(2W)$ is called the attempt frequency, while Γ_i is the escape rate. Further, since the formula Eq. (3.50) has a Lorentzian form, the quantity $\tau = \hbar/\Gamma_i$ is the measure of time spent inside the well. Thus if the resonant peaks are narrow (i.e. Γ_i are small), it is indication that carriers spend a long time inside the structure. Of course this time is always finite, as the resonant levels are only quasi-bound due to finite barrier height/thickness. Now we turn our attention back to the realistic case of hole tunneling where transmission and reflection coefficients should be evaluated numerically, and in the presence of an applied bias. A typical electrical scheme of the whole device to probe tunneling through such a structure is given in Fig. 3.15. The voltage is usually computer controlled, while the current is measured using low noise amplifier[112]. The resonant tunneling diode is placed within cryostat containing liquid helium or nitrogen. A small capacitor is placed parallel to DBRS in order to stabilize the voltage.

When a bias is applied across the structure there is a net current flowing from the left to the right lead, if there are unoccupied states on the right lead. Taking into account $|t^0_{\lambda\mu}|^2 \cdot v^{(R)}_{z\mu} = T_{\lambda\mu} \cdot v^{(L)}_{z\lambda}$ the expression for the current

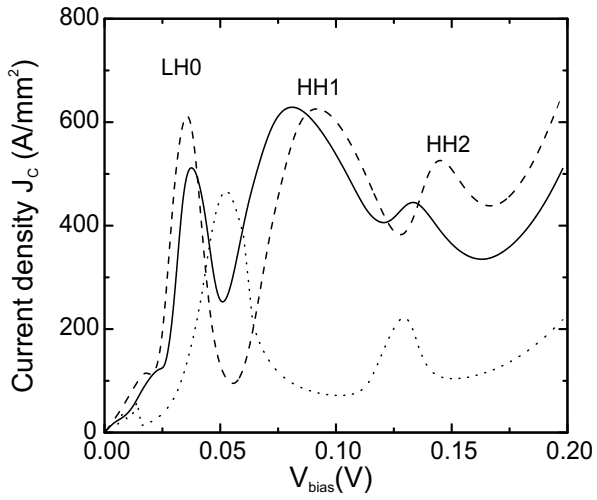

Fig. 3.16 Tunnelling current through DBRS as a function of applied bias at $\mathbf{B}$=0 in arbitrary units (solid line) in the spherical approximation, $\gamma_2 = \gamma_3$. As a reference $J_C(V_{bias})$ is shown (dotted line) when the approximation $k_\parallel = 0$ is used as in Ref. [115]. The dashed line represents the values of the current calculated without approximations.

density is

$$J_C = \frac{e}{8\pi^3}\int dk_x dk_y dk_z \left\{\sum_\mu T_{h_1\mu} v_{zh_1}^{(L)} + \sum_\mu T_{h_2\mu} v_{zh_2}^{(L)} + \sum_\mu T_{h_1\mu} v_{zl_1}^{(L)} + \sum_\mu T_{l_2\mu} v_{zl_2}^{(L)}\right\} [f(E) - f(E + eV_b)]\,. \tag{3.51}$$

However since the transmission coefficient are calculated at fixed E, it is better to change the variable k_z into E_z. Then the used formula has the form

$$J_C = \frac{e}{8\pi^3\hbar}\int_0^{k_{\parallel max}} k_\parallel\, dk_\parallel \int_0^{2\pi} d\phi\, dE \Big(\sum_{\mu\lambda} T_{\mu\lambda}\Big) \times [f(E) - f(E + eV_b)]$$

where it is assumed that $dE = dE_z$ since integration over $k_\parallel$ is in the front of integral over dE_z. The tunnelling current is calculated for a double barrier resonant structure. However another set of values of the Luttinger parameters is taken $\gamma_1 = 7.65, \gamma_2 = 2.845, \gamma_3 = 2.845, \kappa_0 = 1.72$ (for both materials) in order to make a comparison with the results of Ref. [115] possible. The other parameters are taken from the same reference: barrier height $V_0 = 0.1eV$, barrier width $D = 25$Å, well width $W = 80$Å, and the Fermi energy $E_F = 10meV$. The current density as a function of applied bias is plotted in Fig.

3.16, along with results of Ref. [115] (dashed line) for $T = 0K$. The first two peaks correspond (neglecting the small one -HH0 at small V_{bias}) to the first light hole resonance (in the well) - LH0, and the second heavy hole resonance - HH1. In Ref. [115] the explicit dependence of the current on the in-plane momenta was neglected in order to facilitate numerical integration in Eq. (3.51). Though the two curves are of the same order of magnitude, the two peak structure is not reproduced with the approximation $J_C(E, k_\parallel) \approx J_C(E_\parallel)$. These two peaks indeed coincide with one another at $k_\parallel = 0$, but because of the different mass of the heavy and light holes, and more importantly because of band mixing the position of the resonant levels in the well between the two barriers split when $k_\parallel > 0$.

Now we revert to the previous values for the Luttinger parameters: $\gamma_1^a = 6.85$, $\gamma_2^a = 2.1$, .. etc. (see previous section) but the same dimensions of the DBRS, i.e. $D = 25$Å$W = 80$Å. The transmission coefficients $T_{h_1\lambda}$ and $T_{l_l\lambda}$ ($\lambda \in \{h_1, h_2, l_1, l_2\}$) when an external magnetic field $\mathbf{B} = 10T$ is applied in plane (except in the contact regions), i.e. parallel to the layers, is shown in Figs. 3.17(a) and 3.17(b), respectively. Out of 16 possible transmission channels only 8 are different and shown in the figures, due to the fact the magnetic field is normal to the quantization axis and there is no bias. The peaks in $T_{\lambda\mu}$ that correspond to the light hole resonance LH0 are broader than those that correspond to HH resonances since the light holes reside shorter in the structure. It can be seen that the HHx resonant peaks do not show any visible splitting when a magnetic field is applied along the $x-$axis. This is a consequence of the fact that the quantization axis for angular momentum is chosen to be along z, and the operator $\hat{S}_z$ for the heavy hole states at $k_\parallel = 0$ has definite values $s_z = \pm 1/2$. Thus expectation value of $\hat{J}_x$ between the states of the heavy holes at $k_\parallel = 0$ is zero[115, 128], i.e. $< J_x >= 0$. This conclusion becomes a little bit more relaxed for larger in-plane momenta, but still the heavy hole splitting is significantly smaller than that of the light holes.

Finally, the current density is given in Fig. 3.18, for four different values of the magnetic field strength at $T = 0K$. The amplitudes of peaks in general decreases with increase of magnetic field, as the vector potential component $eA_y/\hbar$ narrows the range of (k_x^0, k_y^0) in momentum space that can ensure efficient tunnelling. However, one can see that a significant drop in the values of the current occurs at $B = 15T$. The reason is that the energy of light holes that corresponds to the shift in wavevector $\Delta k_y = e/\hbar(W + 2D)B/2$ by the field is comparable to the Fermi energy. Then the current consists only of heavy holes, which though having larger density of states in the emitter, contribute less to the current due to their heavier mass[120]. The heavy hole component of the current is shown in Fig. 3.19. It is apparent that the peak LH0 increases with B as the heavy holes acquire the light hole character thus lowering their effective mass. To check spin polarization effects in DBRS one

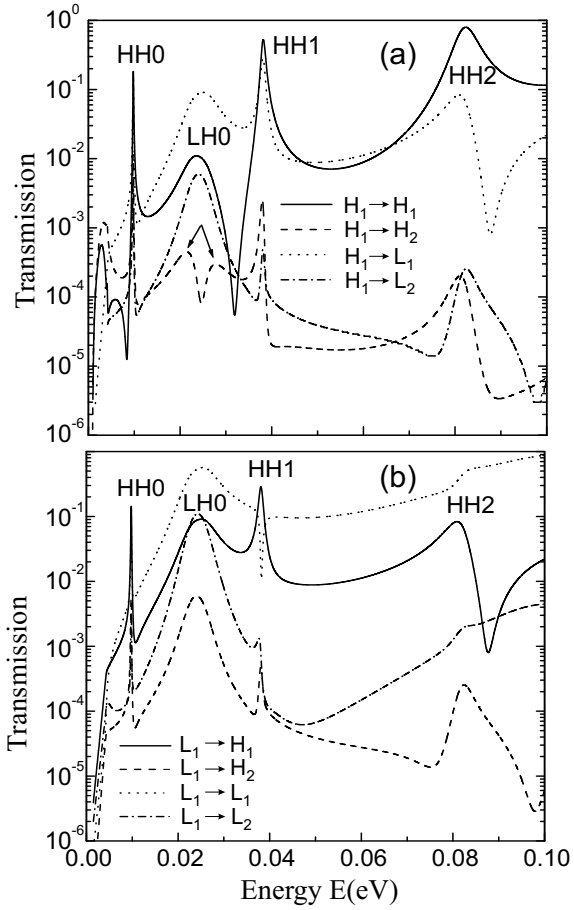

Fig. 3.17 Transmission coefficients of: (a) the heavy hole h_1 and (b) the light hole l_1 to other four possible hole states as a function of the energy of the incoming hole, in the presence of an in-plane magnetic field $B = 10T$.

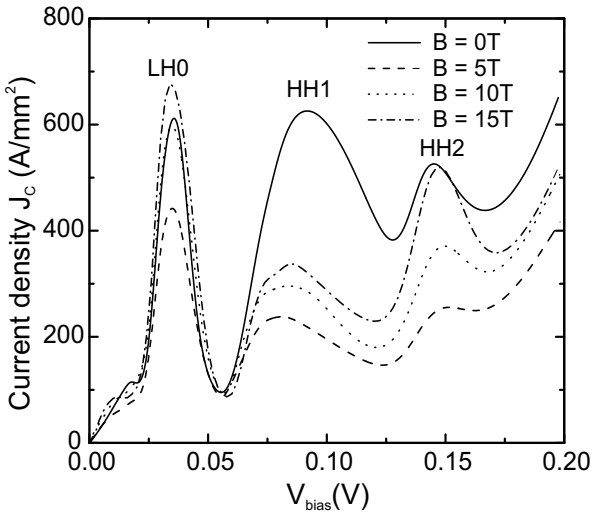

Fig. 3.18 Tunnelling current through DBRS as a function of applied bias for $B = 0\,T$ (solid line), $B = 5\,T$ (dashed), $B = 10\,T$ (dotted), and $B = 15\,T$ (dash-dotted).

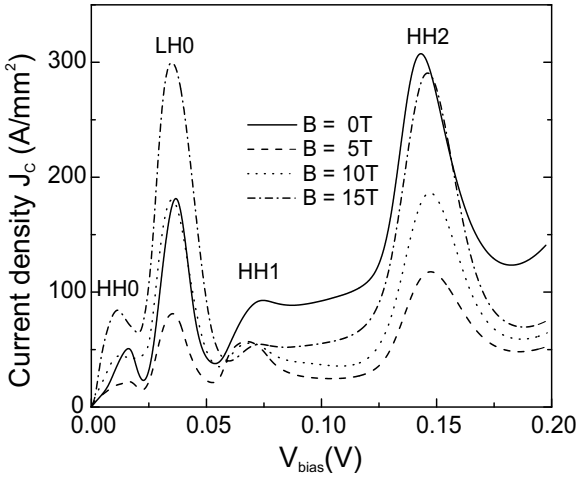

Fig. 3.19 Heavy hole current component as a function of applied bias for $B = 0\,T$ (solid line), $B = 5\,T$ (dashed), $B = 10\,T$ (dotted), and $B = 15\,T$ (dash-dotted).

needs to evaluate the ratio

$$P = (J_C^{\uparrow} - J_C^{\downarrow})/J_C = \Delta J_C/J_C\,, \tag{3.52}$$

where

$$\begin{aligned}\Delta J_C \quad &= \tfrac{e}{8\pi^3\hbar}\int k_{\|}\,dk_{\|}\,d\phi\,dE\Big(\textstyle\sum_{\mu\lambda} T_{\mu\lambda} < V_\lambda|\hat{\sigma}_z|V_\lambda > \Big) \\ &\quad \times [f(E) - f(E + eV_b)]\,.\end{aligned}$$

Here $\hat{\sigma}_z$ is the Pauli spin operator acting as a weighting factor in the output channels in Eq. (3.53) and reads

$$\sigma_z = \begin{pmatrix} 1 & 0 & 0 & 0 & \cdot & 0 & 0 \\ 0 & \frac{1}{3} & 0 & 0 & \cdot & \frac{2\sqrt{2}i}{3} & 0 \\ 0 & 0 & -\frac{1}{3} & 0 & \cdot & 0 & -\frac{2\sqrt{2}i}{3} \\ 0 & 0 & 0 & -1 & \cdot & 0 & 0 \\ \cdot & \cdot & \cdot & \cdot & \cdot & \cdot & \cdot \\ 0 & -\frac{2\sqrt{2}i}{3} & 0 & 0 & & -\frac{1}{3} & 0 \\ 0 & 0 & \frac{2\sqrt{2}i}{3} & 0 & & 0 & \frac{1}{3} \end{pmatrix} \tag{3.53}$$

For 4-component vectors (neglecting the SO band) is actually equal to $\frac{2}{3}J_z$ in the subspace of heavy and light holes $|3/2, j_z\rangle$, as was already pointed out during the derivation of the hole Zeeman term in Ref. [105]. In the limit of a strong spin-orbit coupling and a small Fermi energy $E_F/\Delta \to 0$, as in our case, the 4×4 LK is a good approximation[129] to explain the holes. The spin polarization of the current and its HH and HL components as a function of magnetic field are given in Fig. 3.20, for an applied bias $V_{bias} = 0.1eV$. The currents are polarized even at $B = 0$, which is a consequence of lifting of Kramers degeneracy due to structural inversion asymmetry (SIA). The increase of magnetic field strength enhances the total polarization, while the kinks in the HH and LH polarization around $B = 15T$ is due to the disappearance of the light holes in the right lead at this particular bias. The maximal polarization that can be achieved for this dimensions of DBRS is 3%. The spin polarization can be enhanced by tuning the external bias V_{bias} or/and the well width W. We note, at this point, that P is not a monotonous function of V_{bias} and W.

In this chapter the tunnelling of holes is investigated within the frame of the 4×4 Luttinger-Kohn Hamiltonian in the most general case where $\gamma_1 \neq \gamma_2 \neq \gamma_3$. The transmission coefficients are plotted as a function of in-plane momenta (k_x, k_y), which is a conserved quantum number throughout the structure. The conservation of probability current density, i.e. the sum of all transmission and reflection coefficients equals unity, is confirmed to be valid in all cases, contrary to the conclusions of Ref. [120]. The anisotropy caused by the difference in the Luttinger parameters in $\gamma_2 \neq \gamma_3$ is reflected mainly in the transmission between the two heavy holes (with or without external magnetic field), because their propagating states exist for larger (k_x, k_y) (than

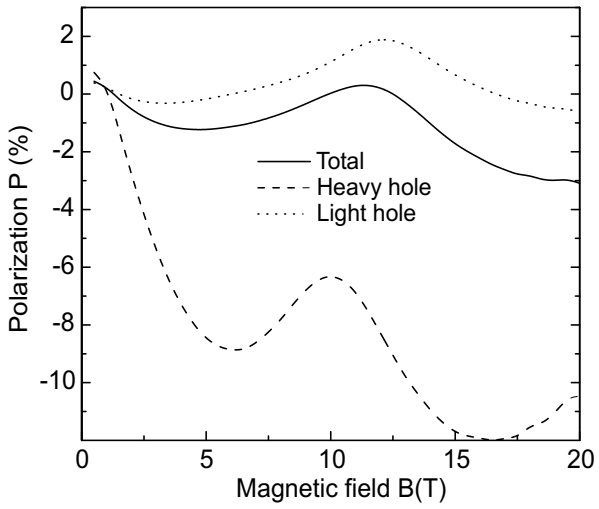

Fig. 3.20 Spin polarization (-P) of the current as a function of in-plane magnetic field for bias $V_{bias} = 0.1eV$: total polarization (solid line), heavy hole (dotted), and light hole polarization (dashed). Not that the values of P are negative.

that of the light hole) when band mixing plays an important role. Range of parameters (E, k_x, k_y) for case (iii), where the light holes propagate at group velocity opposite to their phase velocity, is narrow, and transmission coefficients are small so its influence on the current is not significant. However, we find that employing any approximation, such as spherical, isotropical, or neglecting the dependence of J_C on (k_x, k_y) can lead to visible discrepancies as was shown in Fig. 3.16. The main consequence of band mixing is that heavy holes acquire light hole character in the barrier, thus enhancing their tunnelling. The values of $T_{h_1 h_1}$ are larger than in the one-band picture, and increase with (k_x, k_y) as long as both heavy and light holes exist in the external leads (case(i)). In the presence of an in-plane magnetic field (normal to the current) the holes acquire an additional in-plane momentum k_y and for certain values of (E, k_x, k_y) heavy holes stay longer in the barrier, thus enhancing their (partial) light hole character. Then the transmission between the two light holes is possible, i.e. the hole undergoes a precession. The heavy holes at $k_\parallel = 0$ can not precess because of the zeros in the hamiltonian between h_1 and h_2. However the band-mixing lifts this 'selection rule' as heavy holes acquire some of the light hole character. We presented results for the current density of DBRS which is an interesting structure for possible applications, and it is a common setup in experiments. Upon comparing results with other theoretical results already present in the literature, we find that band mixing is important and can not be neglected. At the end, we presented the

ratio of spin polarization P as a function of magnetic field. Spin polarization can be enhanced by tuning the well width and/or by the increase of applied bias.

Publications. The results presented in this chapter were published as

- P. Krstajić and F. M. Peeters, *Magnetotunneling of holes through single and double barriers using a multiband treatment*, Phys. Rev. B **71**, 115321 (2005) (10 pages).

4

Hole tunneling through DMS structures

4.1 INTRODUCTION

There has been a continuing interest in spin-dependent tunneling in diluted magnetic semiconductors (DMS), due to its possible application in devices such as sensitive read heads[2], in data storage systems, spin transistors[3], magnetic memories[130] etc. Giant magnetoresistance (GMR) has been realized in the form of a spin-valve and gained acceptance in commercial hard disks during the past $5-10$ years. A spin valve (GMR) read head consists of two ferromagnetic layers (alloys of nickel, iron, and cobalt) sandwiching a thin nonmagnetic metal (usually copper). One of the layers is made of softer magnetic materials (lower coercive field) and its orientation is sensitive to small magnetic fields. The orientation of the another layer is fixed (pinned) by an additional layer, called exchange layer which is usually antiferromagnet. Due to technological reasons, the materials used are (half)metallic ferromagnets, and metallic conductors. The modulation of the resistance during reading of a magnetic disc, i.e. magnetoresistance $(R(H)-R(0))/R(0)$, in this type of heads can reach[2] 20%. They were introduced in production line by IBM in 1997 and replaced old Anisotropic Magnetoresistive heads (AMR) that had magnetoresistance typically 2%. As a consequence spin-valve heads have higher sensitivity that, in turn, made possible to reach higher areal data density of 10Gb/in^2 instead of 3.3Gb/in^2 in the early nineties. In order to achieve higher density, a promising alternative, is to use magnetic tunneling junction (MTJ) devices that consist, at its core, of two thin ferromagnetic layers separated by a semiconductor, where the tunneling magnetoresistance (TMR) can

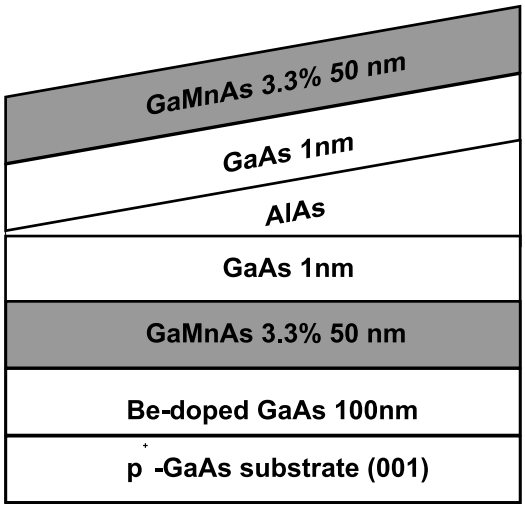

Fig. 4.1 Schematic illustration of a wedge-type trilayer heterostructure sample grown by LT-MBE. It was obtained by linearly moving the shutter during the growth[132].

reach $40 - 50\%$. With the advent of novel DMS materials like (Ga,Mn)As several groups have achieved higher TMR, in trilayer structures made of two (Ga,Mn)As layers separated by an AlAs (barrier) up to[131] 290% and[132, 133] 75%. However, the low Curie temperature (below room temperature) of many III-V DMS still poses a serious obstacle to its wide commercial use. Another disadvantage is high resistivity of these structure that deteriorates signal to noise ratio. In this chapter I concentrate on the theoretical investigation of hole tunneling through a (Ga,Mn)As/GaAs/AlAs/GaAs/(Ga,Mn)As structure, where a thin layer of GaAs is used in experimental setups to avoid diffusion[134] of Mn into AlAs, unwanted strain, and make interfaces smoother. The first experiment on DMS trilayer structure was conducted in 2001 by Higo and Tanaka at Tokyo University, Japan. In order to probe the performances of trilayer structure as a function of the barrier thickness, the authors of Ref.[132] linearly moved the shutter during growth MBE so that a wedge-type trilayer structure is obtained, which scheme is shown on Fig. 4.1. On the other hand, tunneling processes and spin-polarization have already been treated[135] in double barrier structures made of (Ga,Mn)As/GaAs within the single band model. However, a more generalized 6×6 Luttinger - Kohn[104] Hamiltonian where exchange is included[52, 136, 137] has been employed to estimate theoretically the value of GMR in similar structures. A similar theoretical framework was already used previously to investigate the charge and spin distribution in (Ga,Mn)As/GaAs multilayers[138]. Furthermore, the success of $\mathbf{k} \cdot \mathbf{p}$ theory to determine resonant peaks[108] and tunneling lifetimes in double barrier structures[109] gives us confidence to apply it to FM DMS

trilayers as well, as several authors have already done in other structures[137, 139].

4.2 MODEL

The 6×6 Luttinger - Kohn model will be used (as described) in the previous chapter in order to account for spin-orbit coupling. While in nonmagnetic GaAs/AlAs heterostructures it is still possible to neglect the SO band ($\epsilon_F >> \Delta_{SO}$) and use the 4×4 LK[140], the inclusion of all three bands is necessary in DMS since the spin-splitting of holes is comparable with Δ_{SO}. The Hamiltonian with exchange reads

$$H_{6\times 6} = H_{LK} + V(z)I_6 - \Delta_{ex} s_x \tag{4.1}$$

The $H_{6\times 6}$ is 6×6 Luttinger - Kohn Hamiltonian

$$H_{LK} = \begin{pmatrix} P_1 & L & M & 0 & iL/\sqrt{2} & -i\sqrt{2}M \\ L^\dagger & P_2 & 0 & M & -i\sqrt{2}Q & i\sqrt{3/2}L \\ M^\dagger & 0 & P_2 & -L & -i\sqrt{3/2}L^\dagger & -i\sqrt{2}Q \\ 0 & M^\dagger & -L^\dagger & P_1 & -i\sqrt{2}M^\dagger & -iL^\dagger/\sqrt{2} \\ -iL^\dagger/\sqrt{2} & i\sqrt{2}Q & i\sqrt{3/2}L & i\sqrt{2}M & P+\Delta_{SO} & 0 \\ +i\sqrt{2}M^\dagger & -i\sqrt{3/2}L^\dagger & i\sqrt{2}Q & iL\sqrt{2} & 0 & P+\Delta_{SO} \end{pmatrix}, \tag{4.2}$$

where the matrix elements of the Hamiltonian are given by

$$P = \frac{\hbar^2}{2m_0}\gamma_1 k^2,\ Q = \frac{\hbar^2}{2m_0}\gamma_2(k^2 - 2k_z^2)\,, \tag{4.3a}$$

$$P_1 = P + Q \quad P_2 = P - Q\,, \tag{4.3b}$$

$$L = -i\frac{\sqrt{3}\hbar^2}{m_0}\gamma_3\left(k_x - ik_y\right)k_z\,, \tag{4.3c}$$

$$M = \frac{\sqrt{3}\hbar^2}{2m_0}\left(\gamma_2\left(k_x^2 - k_y^2\right) - 2i\gamma_3 k_x k_y\right)\,, \tag{4.3d}$$

while Δ_{ex} is the exchange splitting at $\mathbf{k} = 0$ between the two heavy hole states, and s_x is the operator of hole-spins in the $|j, j_z\rangle$ basis. This term is actually the mean-field approximation of the $p-d$ exchange interaction term

$$H_{pd} = \sum_i \int d^3\mathbf{r} J_{pd}(\mathbf{r} - \mathbf{R}_i)\delta(\mathbf{r} - \mathbf{R}_i)\mathbf{S}_i \cdot \mathbf{s}(\mathbf{r})\,, \tag{4.4}$$

where $\mathbf{s}$ is the spin-operator of holes, and the index i runs over Mn sites. The basis functions are ordered as $\{|3/2, 3/2\rangle\,, |3/2, 1/2\rangle\,, |3/2, -1/2\rangle\,, |3/2, -3/2\rangle\,, |1/2, -1/2\rangle\,, |1/2, 1/2\rangle\}$.The quantization axis is commonly chosen to be along the growth direction z. On the other hand, it is known that the easy axis of

magnetization of ferromagnetic layers of (Ga,Mn)As is in-plane, when grown on GaAs substrate due to compressive strain. Note that the lattice constant of (Ga,Mn)As increases with Mn content. In the present model the $p-d$ exchange between holes and d-electrons on Mn, parameterized by the β integral, is taken in the mean-field approximation. The value of Δ_{ex} can be estimated to be $xS(T)\beta N_0$, where $S(T)$ is roughly given by the Brillouin function, and N_0 is the number of cations per unit area. If the magnetization M of the sample is experimentally known, than a better estimate would be $\Delta_{ex} = \beta M/(g\mu_B)$. The internal magnetic field ($B_{int} = \mu_0 M$) is considered to have negligible effect on the orbital motion of the holes (k_α are unchanged), and also the ordinary Zeeman effect is omitted from the Hamiltonian. Here γ_i are the well known Luttinger parameters fitted according to experimental data. In each n^{th} layer the wave function has the following form

$$\Psi(\mathbf{r}) = e^{i(k_x x + k_y y)}\psi(z)\,, \tag{4.5}$$

with

$$\psi(z) = \sum_{i=1,n_b} \left[A^+_{n,i} V^+_{n,i} e^{ik^+_{n,i}z} + A^-_{n,i} V^-_{n,i} e^{ik^-_{n,i}z}\right]. \tag{4.6}$$

Here V_i represents the 6-column eigenvectors[119] of the Hamiltonian at the same energy E, and parallel momentum $\mathbf{k}_\parallel$ and the wavevector k_{zi} classifies the states of heavy and light holes (n_b is the number of bands). The canonical wavevectors $\mathbf{k}_\parallel = (k_x, k_y)$ are conserved, so that mathematically the problem is reduced to a one dimensional problem. The eigenvectors V_i should be normalized to unity to ensure that the coefficients $a_i^{(L,R)}$ are directly proportional to the probability current density of the particular channels, i.e. to transmission (reflection) coefficients. If the Hamiltonian is written as

$$H = H_n^{(2)} k_z^2 + H_n^{(1)} k_z + H_n^{(0)}\,, \tag{4.7}$$

the wavevectors k_{zi} can be found from the augmented eigenvalue problem

$$\begin{pmatrix} \mathbf{0} & I \\ -(H_n^{(2)})^{-1} H_n^{'} & -(H_n^{(2)})^{-1} H_n^{(1)}(k_\parallel) \end{pmatrix} V_a = k_z V_a\,, \tag{4.8}$$

where $V_a = (V_i, k_{zi}V_i)^T$ and $H_n^{'} = H_n^{(0)} - E_n I$. This leads to the characteristic polynomial with 12 solutions corresponding to waves travelling in both directions. This procedure has the advantage that one obtains both wavevectors k_{zi} and eigenvectors V_i at once. The coefficients A_n^+ correspond to the eigenvalues travelling with positive group velocity, i.e. $j_z > 0$ and $Im\{k_z\} = 0$, or decaying in the positive direction $Im\{k_z\} > 0$. The number of positive modes should be half the total number of modes, since the relation

$$E(-\mathbf{k}, \uparrow) = E(+\mathbf{k}, \downarrow)\,, \tag{4.9}$$

still holds even in the presence of a magnetic field and/or localized moments. This is a consequence of the time invariance of the Hamiltonian:

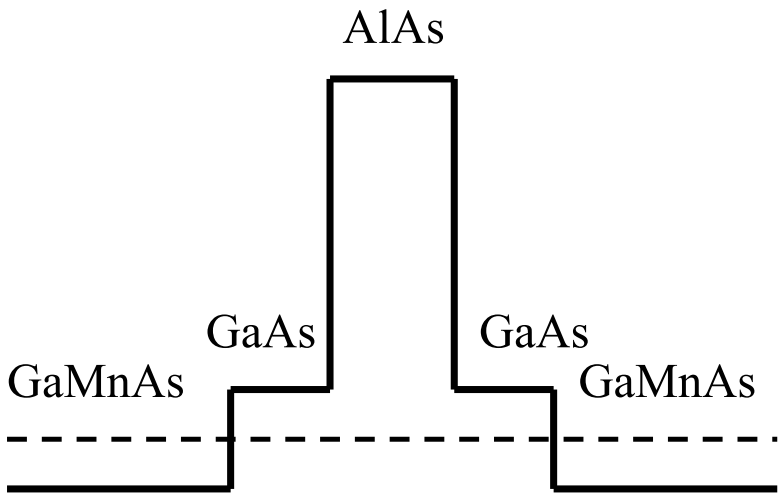

Fig. 4.2 Schematic band diagram (top of valence band) of a trilayer structure made of two DMS layers (Ga,Mn)As separated by an AlAs layer acting as a barrier. Two additional layers of GaAs are inserted in-between in order to prevent diffusion of Mn into the barrier.

$$[\hat{\theta}, \hat{H}] = 0, \quad \hat{\theta}\Psi(\mathbf{r}, t) = \sigma_y \Psi^{\dagger}(\mathbf{r}, -t)\,. \tag{4.10}$$

A typical trilayer structure(Ga,Mn)As/GaAs/AlAs/GaAs/(Ga,Mn)As used in experiments is shown in Fig. 4.2. It consists of two (Ga,Mn)As layers separated by a thin layer made of AlAs. Two additional layers of GaAs are inserted to prevent diffusion of Mn into AlAs. Since there are six channels possible for tunneling (see Chapter 3), i.e. mixing of different kinds of holes may happen depending on the scattering potential (barrier), the transmission and reflection coefficients should be normalized to the group velocity[140]

$$T_{\lambda\mu} = \left| \frac{A^{+}_{R\mu}}{A^{+}_{L\lambda}} \right|^2 \cdot \frac{v_{gr\mu}}{v_{gr\lambda}}\,. \tag{4.11}$$

The quantities $A^{+}_{R\mu}$ and $A^{+}_{L\lambda}$ are amplitudes of the quantum mechanical waves right and left of the structure, while μ, λ denote various hole states. The conservation of the probability current leads to six relations among transmission and reflection coefficients

$$\sum_{\mu} \Big(T_{\lambda\mu} + R_{\lambda\mu} \Big) = 1\,. \tag{4.12}$$

Here the variable λ assumes all six hole states (h_1, h_2, l_1, l_2, s_1 and s_2). These relations are also useful to check the consistency of the numerical calculations.

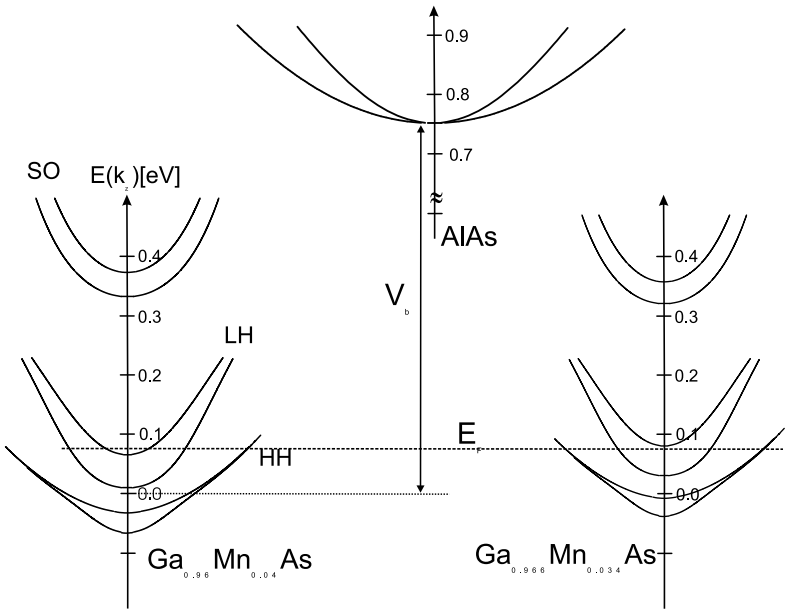

Fig. 4.3 Scheme of the band positions of the two (Ga,Mn)As layers and the barrier of AlAs. The band diagram of GaAs, and split-off band of AlAs are not shown for clarity.

Formally present in Eq. (4.12) split-off band states s_1, s_2 do not contribute to the current since the band edge of the LH "upper subband" is still higher than the SO down subband ($\Delta_{SO} > \Delta_{ex}$). They influence the current values however in an indirect way since the imaginary parts of k_{so} are small, and because the matrix component $\sqrt{2}Q$ (that contains $\hat{k}_z$) mixes the LH and the SO holes. Thus, one should take into account more precisely the dispersion relation $\epsilon_{hh,lh}(k)$ obtained from $H_{6\times 6}$ when ϵ_{lh} approaches the SO band. A better insight into band alignment of materials is given in Fig. 4.3, with GaAs spacers excluded. The scheme of dispersions $E(k_z)$ are given for $k_x = 0, k_y = 0$, for ($Ga_{0.96}$,$Mn_{0.04}$)As (first FM layer), pure AlAs and ($Ga_{0.966}$,$Mn_{0.034}$)As (second FM layer). The valence band of AlAs is shifted by 0.75eV to the total barrier height AlAs/GaAs and GaAs/(Ga,Mn)As. The smaller splitting between the heavy holes as compared to the one of the light holes is a result of spin-orbit interaction[141, 142] and the fact that the magnetization M is in plane.

4.2.1 Results

The numerical method is based on the transfer matrix method for stratisfied media. The coefficients A on either side are connected by

$$\begin{pmatrix} A^+ \\ 0 \end{pmatrix} = T \begin{pmatrix} I_\lambda \\ r \end{pmatrix}, \tag{4.13}$$

where the column I_λ contains 1 for the λ-th channel, other being zero i.e. $I_\lambda = \delta_{i\lambda}$, while r sub-column contains reflection coefficients. The matrix M is composed of the boundary matching matrix M_i and the propagation matrix P

$$T = M_N^{-1}(M_{N-1}P_N M_{N-1}^{-1}) \cdot .. \cdot (M_1 P M_1^{-1}) M_0 \,, \tag{4.14}$$

whose explicit expressions can be found elsewhere[120]. In the case of a trilayer one has three layers GaAs/AlAs/GaAs, while two (thick) layers of (Ga,Mn)As act as the emitter and collector leads. It is found[143] that GaAs acts as a barrier to (Ga,Mn)As, whose height depends on the manganese content. Its experimental value is in the range $(88, 146)meV$ for $x(Mn)(1.2-2.5\%)$ according to Ref.[143] and consistent with Ref. [134]. Having found transmission coefficients $T_{\lambda\mu}$, $\lambda, \mu = 1, .., 6$ from Eq. (4.14), the current density is given by

$$J_C \quad = \tfrac{e}{8\pi^3\hbar} \int_0^{k_{\parallel max}} k_\parallel \, dk_\parallel \int_0^{2\pi} d\phi \left(\textstyle\sum_{\mu\lambda} T_{\mu\lambda} \right),$$

in the limit of small $V_{bias} << \epsilon_F$. The tunneling current Eq. (4.15) is calculated for both alignment of the two (Ga,Mn)As, so that the tunneling magnetoresistance is found from

$$TMR = \frac{J_{Cp} - J_{Ca}}{J_{Cp}} \,, \tag{4.15}$$

where J_{Cp} is the density of tunneling current when the two FM films are parallel, while J_{Ca} denotes the current density when the two are antiparallel. For our numerical calculations we used the sample parameters of Ref. [132]. These parameters are: width of two GaAs layers is $D_0 = 1$nm, barrier thickness D of AlAs varied from 1.2nm till 2.2nm, the Mn molar content of the two DMS layers are 4.0% and 3.3%. The exchange energies corresponding to these values are $\Delta_{ex}^L = 0.12eV$ and $\Delta_{ex}^R = 0.1eV$, respectively assuming full alignment of manganese localized moments. The different manganese concentration is made deliberately in order to build in the discrepancy in coercivity of the two DMS layers, i.e. to allow an easy change from parallel to antiparallel orientation. The applied bias was $eV_{bias} = 1$meV much smaller than the Fermi level $\epsilon_F \approx 80$meV. The barrier height $V_b = 0.75$eV, and the measurement was performed at low temperature $T = 8K$ which justifies using formula Eq. (4.15). The barrier height V_{b2} between (Ga,Mn)As and GaAs is taken to be approximately $0.2eV$, since x(Mn) is higher than 3%. The Luttinger

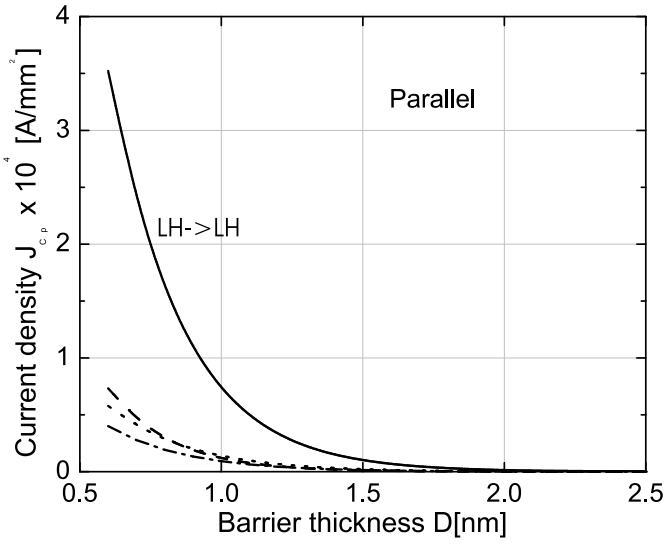

Fig. 4.4 Components of the current density J_{Cp} as a function of barrier thickness D in case when the DMS layers are aligned parallel. Light hole to light hole transmission is dominant.

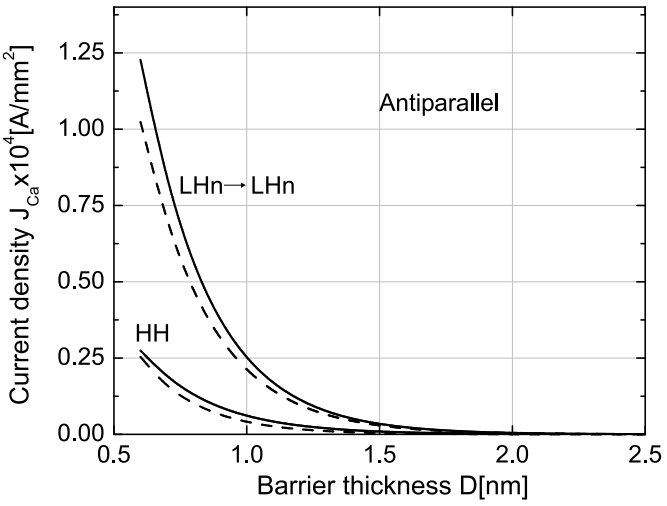

Fig. 4.5 Components of the current density J_{Ca} as a function of barrier thickness D in case when the DMS layers are aligned antiparallel. Heavy to heavy hole component makes up less than 20% of the total current.

parameters are: $\gamma_1^{(1)} = 6.85$, $\gamma_2^{(1)} = 2.1$, $\gamma_3^{(1)} = 2.9$ (GaAs) $\gamma_1^{(2)} = 3.45$, and $\gamma_2^{(2)} = 1.29$, $\gamma_3^{(2)} = 0.68$ (AlAs).

In order to gain better insight in the process of tunneling, we show the current density for the case of parallel orientation of the two DMS layers (Fig. 4.4) and for antiparallel (Fig. 4.5) orientation. Out of the 36 possible transmissions only 12 are nonzero since the split-off band is below the Fermi energy, and within the barrier there is no magnetic field. This means, for instance that the transmissions between HH1 and HH2, and between LH1, LH2 are not possible because of the presence of zeros on the small off-diagonal in the matrix elements of Eq. (4.2). However out of these 12 channels only about 4 to 8 are significant depending on the alignment of the ferromagnetic layers. The current components, when the two FM are parallel, are shown in Fig. 4.4. Only one component, light hole to light hole is significantly larger than the other as a result of their lighter mass. They exhibit rapid decay with the barrier thickness. In the next figure, i.e. Fig. 4.5, we present the results for the antiparallel case, where one can notice significantly smaller values for the tunnel currents. The closely spaced curves, two by two, is a consequence of a different Mn content of the two FM layers, i.e. they have different exchange splitting. Thus the transmission probabilities LH1 into LH1 and LH2 into LH2 are not the same. On the other hand, the different polarization of heavy and light holes is because the HH eigenfunctions well defined spin

$$\left|\frac{3}{2},\frac{3}{2}\right\rangle = \frac{1}{\sqrt{2}}\left|X+iY\right\rangle\uparrow;\ \left|\frac{3}{2},-\frac{3}{2}\right\rangle = \frac{i}{\sqrt{2}}\left|X-iY\right\rangle\downarrow, \tag{4.16}$$

while the LH eigenfunctions are composed of different spin subspaces

$$\left|\frac{3}{2},\frac{1}{2}\right\rangle = \frac{i}{\sqrt{6}}\left[\left|X+iY\right\rangle\downarrow -2\left|Z\right\rangle\uparrow\right], \tag{4.17a}$$

$$\left|\frac{3}{2},-\frac{1}{2}\right\rangle = \frac{1}{\sqrt{6}}\left[\left|X-iY\right\rangle\downarrow +2\left|Z\right\rangle\downarrow\right]. \tag{4.17b}$$

Fig. 4.6 shows the theoretical estimate for TMR (solid line), along with the experimental data from Ref.[132] (closed circles) for manganese concentration $x = 4\%$ (1st FM layer) and $x = 3.3\%$ (2nd FM layer). A decent agreement is achieved only for two experimental points, while for higher D, the experimental data show a rapid decay. There could be several reasons for this discrepancy: the possibility of indirect tunneling[134], presence of defects that spoil resonant tunneling, presence of Mn in the barrier, etc. Despite the fact that the structure is made by the sophisticated MBE growth technique, the presence of As antisites, and interstitial Mn is inevitable in the fabrication of (Ga,Mn)As. Another reason is the presence of two GaAs layers on both sides, whose thickness is comparable with the width of the trilayer structure and is not changed in the experiment, while the barrier they impose is not so high. This is clearly shown on the same figure, where the dash-dotted line corresponds to the TMR in the absence of the two GaAs layers. The

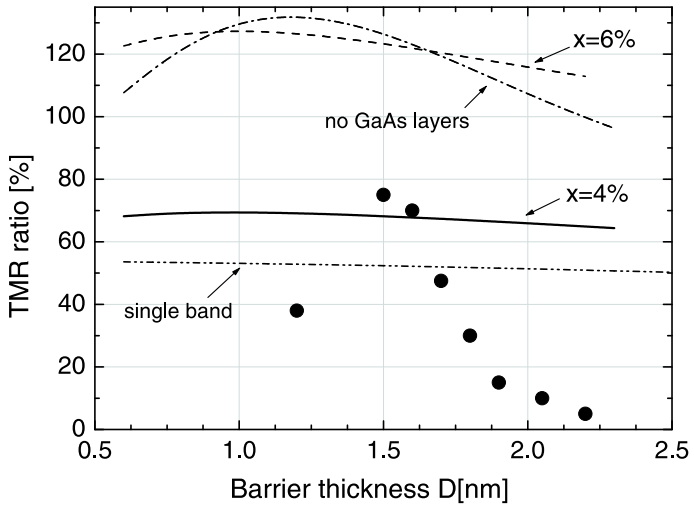

Fig. 4.6 Tunneling magnetoresistance ratio (TMR) as a function of the thickness D of the AlAs tunnel barrier of AlAs (solid line), is shown along with experimental data taken from Ref.[132] (closed circles). For comparison, theoretical TMR without the two GaAs spacers (dash-dotted line), and within the single band approximation (dash-dot-dot) are given, all for x(Mn)= $(4.0, 3.3)$%. In addition, we present the result for a higher Mn content x= $(6.0, 5.5)$% of the two layers.

slope of the curve is more pronounced than in the previous case. On the other hand, the considered model does not have any fitting parameter, apart from the assumption of full alignment of Mn spins, so that theory sets an upper bound for the TMR and gives correct order of magnitude of the TMR. Clearly, in order to enhance TMR one should enlarge the spin-splitting of the holes in (Ga,Mn)As, e.g. by increasing the Mn content. Calculations of TMR for $x = 6\%$ ($x = 5.5\%$) are given in the same Fig. 4.6 (dashed line). The predicted value of the magnetoresistance for this x(Mn) reaches 130%, a promising value, but it was obtained under the assumption that there are no self-compensation effects, either for the hole density or the magnetization of the layers.

4.2.2 Single band approximation

In order to gain better insight into the tunneling processes, we depart from the 6×6 Luttinger-Kohn model and analyze the problem within the single band approximation. This serves only as an illustration and to explain qualitatively the slow variation of the TMR ratio on the barrier thickness. The wave function in the three regions, for incoming spin-up state is

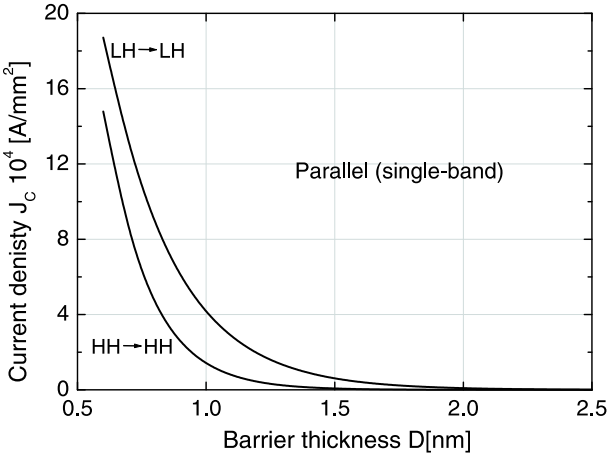

Fig. 4.7 Light and heavy hole components of the tunneling current, within the single band approximation, when the FM layers are parallel.

$$\psi_I(z \leq 0) = V_\uparrow e^{ik_{z\uparrow}z} + r_{\uparrow\uparrow}V_\uparrow e^{-ik_{z\uparrow}z} + r_{\uparrow\downarrow}V_\downarrow e^{-ik_{z\downarrow}z}\,, \tag{4.18a}$$

$$\psi_{II}(0 < z < d) = A_\uparrow V_\uparrow e^{ik_{z2\uparrow}z} + B_\uparrow V_\uparrow e^{-ik_{z2\uparrow}z} + A_\downarrow V_\downarrow e^{ik_{z2\uparrow}z} + B_\downarrow V_\downarrow e^{-ik_{z2\downarrow}z}\,, \tag{4.18b}$$

$$\psi_{III}(z \geq d) = t_{\uparrow\uparrow}V_\uparrow e^{ik_{z\uparrow}z} + t_{\uparrow\downarrow}V_\downarrow e^{ik_{z\downarrow}z}\,, \tag{4.18c}$$

where

$$V_\uparrow = \frac{1}{\sqrt{2}}\begin{pmatrix} 1 \\ 1 \end{pmatrix}, \quad V_\downarrow = \frac{1}{\sqrt{2}}\begin{pmatrix} 1 \\ -1 \end{pmatrix}. \tag{4.19}$$

To simplify the problem further, we neglect the influence of the two GaAs layers. The result for the TMR ratio is shown in Fig. 4.6 (dash-dot-dot line). The exchange energy of heavy holes was taken smaller ($\Delta_{exHH} = 40\%\Delta_{ex}$) than in the full 6-band treatment to account for the influence of spin-orbit interaction (see Fig. 4.3). This value was obtained from the secular equation corresponding to the $H_{6\times6}$ Hamiltonian. Note that, within the single band approximation the HH subbands are significantly split[136]. However, this is only an approximation, since the spin-orbit coupling tends to decrease the heavy hole splitting. Nevertheless, the HH currents for both orientations is significantly smaller than that of the light holes since the heavy holes tunnel less efficiently as they have heavier mass. In figure 4.7 we show the current components within the single band approximation when the ferromagnetic layers are parallel (without GaAs). Like for the case of the 6×6 LK, the current for LH→LH are larger than the HH→HH current. In this case the difference is smaller because we neglected the role of the two GaAs layers acting as a low barrier $V_{b2} = 0.2eV$, and the fact that the effective mass of

holes do not change with $k_{\|}$. One can take into account their influence by introducing the effective width $D_{eff} - D = 0.5$nm, which results into the current values comparable with those given in Fig. 4.4.

4.3 CONCLUSIONS

We have investigated spin-dependent tunneling through a diluted magnetic semiconductor trilayer structure. The problem is investigated within the 6×6 Luttinger-Kohn model for the valence bands, and it was assumed that the TMR is due to direct tunneling because of the high quality of the semiconductor layers. However, the presence of interstitial manganese atoms, and the low temperature MBE that introduces As antisites spoils the coherence of the hole wavefunctions, so that only a semi-quantitative agreement with experiment is achieved. Our theoretical results should be considered as an upper bound, and the main discrepancy between the model and the experimental data is that our predictions of the TMR as a function of the barrier thickness do not show a rapid decay with the barrier thickness. Possible reasons could be non-coherent tunneling as a result of the presence of defect-As antisites, interstitial Mn, etc. Previous theoretical predictions that HH spin-splitting is reduced by spin-orbit interaction is confirmed by our results. However, their influence on the total TMR is smaller than that of the light holes because their tunneling currents (for both orientation) are smaller due to their heavier mass in the tunneling direction.

Publications. The results presented in this chapter were published as

- P. Krstajić and F. M. Peeters, *Spin-dependent tunneling in diluted magnetic semiconductor trilayer structures*, Phys. Rev. B **72**, 125350 (2005) (10 pages).

5

Influence of strain on hole transport

5.1 INTRODUCTION

When an epilayer is pseudomorphically grown on a substrate whose lattice constant differ by several procents, the epilayer is subject to strain. In general the strain spreads over all three directions in space, and it is characterized by a tensor. If one concentrates on two close particular points $A(x_{1a}, x_{2a}, x_{3a})$ and $B(x_{1b}, x_{2b}, x_{3b})$ in a crystal then the displacement $d\mathbf{u}$, is actually a vector that gives rise to a change in their interdistance. If we denote by dl and dl' their distance before and after the deformation:

$$dl = \sqrt{dx_1^2 + dx_2^2 + dx_3^2},\ dl' = \sqrt{dx_1'^2 + dx_2'^2 + dx_3'^2}$$
$$dl'^2 = \sum_i (dx_i + du_i)^2 \tag{5.1}$$

then by expanding dl' up to the first order, we get[149]

$$dl'^2 = dl^2 + 2\frac{\partial u_i}{\partial x_k} dx_i dx_k + \frac{\partial u_i}{\partial x_k}\frac{\partial u_i}{\partial x_l} dx_k dx_l = dl^2 + 2\epsilon_{ik} dx_i dx_k\,. \tag{5.2}$$

The quantity ϵ_{ik} is called the strain or deformation tensor and is given by

$$\epsilon_{ik} = \frac{1}{2}\left(\frac{\partial u_i}{\partial x_k} + \sum_l \frac{\partial u_l}{\partial x_i}\frac{\partial u_l}{\partial x_k}\right). \tag{5.3}$$

The strain tensor can be diagonalized locally as any other symmetrical tensor[149, 150]

$$dl'^2 = (1 + 2\epsilon_{11})dx_1^2 + (1 + 2\epsilon_{22})dx_2^2 + (1 + 2\epsilon_{33})dx_3^2 \,. \tag{5.4}$$

For small deformation, which is the case in semiconductor heterostructures the second term in Eq.(5.1) can be neglected which yields a simple expression

$$\epsilon_{ik} = \frac{1}{2}\left(\frac{\partial u_i}{\partial x_k} + \frac{\partial u_k}{\partial x_i}\right) \tag{5.5}$$

In this chapter we concentrate on the theoretical investigation of hole tunneling through a (Ga,Mn)As/AlAs/(Ga,Mn)As structure grown on a $(In_{0.15}Ga_{0.85})As$ buffer layer[144, 145] that introduces strain into the structure. As the lattice constant of (Ga,Mn)As is smaller ($0.566-0.567$Å) than that of the buffer layer ($a_b = 5.7036$Å), the resulting tensile strain makes the magnetic easy axis orient along the growth direction [001]. Furthermore, the strain shifts the heavy hole bands upward relative to the light hole bands, making electrical transport more complicated. Though the shift at $\mathbf{k} = 0$ is smaller than the magnetic exchange $\Delta_{ex} \approx 100 - 150$meV, and the Fermi energy $E_F \approx 100$meV, its influence is two-fold: first the redistribution of holes in the valence bands, caused by strain, moves the Fermi energy for constant hole density p_h; and the shift between HH and LHs changes the TMR since the heavy and light holes have different mass and different expectation value of spin s_z. The situation considered here corresponds to a somewhat different arrangement to the one treated in previous chapter where the structure was grown on a GaAs substrate. There a small compressive strain makes the easy axis be oriented in-plane, parallel to the interfaces, usually along the [100] direction. Another important fact is that the width D of the barrier made of AlAs is thicker 3 nm (as opposed to $D = 1 - 2.5$ nm for the experiment of Ref. [132]), which makes the use of the envelope approximation more plausible.

5.2 MODEL

Here we will use the 6×6 $\mathbf{k} \cdot \mathbf{p}$ model which is described in the first chapter. The structure of interest is grown pseudomorphically on a substrate/buffer with a different lattice constant, the lattice mismatch introduces biaxial strain, when the deformation tensor is diagonal[151, 152]:

$$\epsilon_{xx} = \epsilon_{yy} = (a_s - a)/a, \quad \epsilon_{zz} = -2C_{12}/C_{11}\epsilon_{xx} \,, \tag{5.6a}$$

$$\epsilon_{\alpha\beta} = 0, \quad \alpha \neq \beta \in x, y, z \,. \tag{5.6b}$$

The total Hamiltonian with biaxial, and magnetic exchange reads

$$H_{6\times6} = H_{LK} + H_{strain} + V(z)I_6 - \Delta_{ex}s_z \,. \tag{5.7}$$

The standard H_{LK} Luttinger - Kohn Hamiltonian was given in the fourth chapter. The quantization axis is commonly chosen to be along the growth direction z. The biaxial strain introduces shifts in the band edges mainly through additional diagonal elements in the Hamiltonian

$$H_{strain} = \begin{pmatrix} P_\epsilon + Q_\epsilon & 0 & 0 & 0 & 0 & 0 \\ 0 & P_\epsilon - Q_\epsilon & 0 & 0 & -i\sqrt{2}\,Q_\epsilon & 0 \\ 0 & 0 & P_\epsilon - Q_\epsilon & 0 & 0 & -i\sqrt{2}\,Q_\epsilon \\ 0 & 0 & 0 & P_\epsilon + Q_\epsilon & 0 & 0 \\ 0 & i\sqrt{2}\,Q_\epsilon & 0 & 0 & P_\epsilon & 0 \\ 0 & 0 & i\sqrt{2}\,Q_\epsilon & 0 & 0 & P_\epsilon \end{pmatrix}, \tag{5.8}$$

the terms P_ϵ, Q_ϵ are related to the deformation tensor $\epsilon_{\alpha\beta}$ through the Bir-Pikus deformation potentials: a_v and b

$$P_\epsilon = -a_v(\epsilon_{xx} + \epsilon_{yy} + \epsilon_{zz}), \quad Q_\epsilon = -\frac{b_v}{2}(\epsilon_{xx} + \epsilon_{yy} - 2\epsilon_{zz})\,. \tag{5.9}$$

In the initial relation for the total Hamiltonian the quantitity Δ_{ex} is the exchange splitting due to the localized $Mn^{2+}(d^5)$ and s_z is the spin operator of holes in the $|j, j_z\rangle$ basis. The value of Δ_{ex} can be estimated if the magnetization of the sample is known, via the relation $\Delta_{ex} = \beta M/(g\mu_B)$, where g is the Landé factor of one localized moment. In each n^{th} layer the wave function has the following form

$$\Psi(\mathbf{r}) = e^{i(k_x x + k_y y)}\psi(z)\,, \tag{5.10}$$

with

$$\psi(z) = \sum_{i=1,n_b} \left[A^+_{n,i} V^+_{n,i} e^{ik^+_{n,i} z} + A^-_{n,i} V^-_{n,i} e^{ik^-_{n,i} z}\right], \tag{5.11}$$

where V_i represents the 6-column eigenvectors[119] at the same energy E, and in-plane momentum $\mathbf{k}_\parallel$, and n_b is number of bands. The coefficients A^+_n correspond to the eigenvalues travelling with positive group velocity, i.e. $j_z > 0$ and $Im\{k_z\} = 0$, or decaying in the positive direction $Im\{k_z\} > 0$. If the Hamiltonian is written as

$$H = H^{(2)}_n k_z^2 + H^{(1)}_n k_z + H^{(0)}_n\,. \tag{5.12}$$

The wavevectors k_{zi} along the growth direction and corresponding eigenvectors V_i can be found from the augmented eigenvalue problem as described in the previous chapter.

5.3 RESULTS FOR THE TRILAYER STRUCTURE

The scheme of the trilayer structure (Ga,Mn)As/GaAs/AlAs/GaAs/(Ga,Mn)As used in the experiment of Ref. [144] is shown in Fig. 5.1. It consists of two

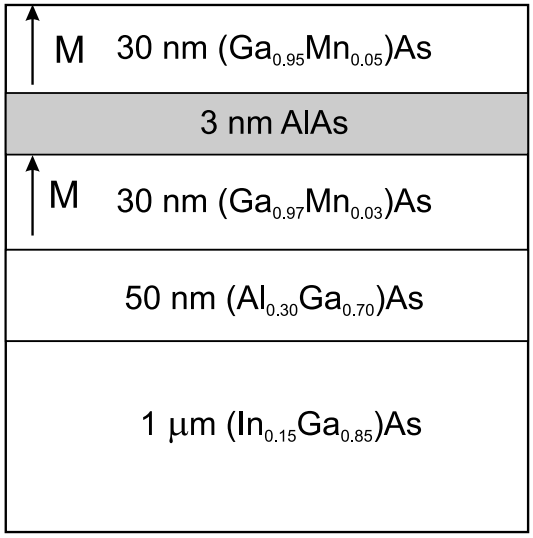

Fig. 5.1 Trilayer structure made of two ferromagnetic (Ga,Mn)As, and an AlAs barrier which was grown on a $In_{0.15}Ga_{0.85}As$ buffer layer. The tensile strain due to the lattice mismatch with the buffer layer causes the magnetization to be in-plane.

Table 5.1 The lattice constants a_{lc}, thermal coefficients α and Bir-Pikus deformation potentials (a_v, b, C_{11}, and C_{12}) for the semiconductors used in the trilayer structure, after Ref. [148]

Mat.	a_{lc}(300K)[Å]	$\alpha[\times 10^{-5}$Å/K]	a_v[eV]	b[eV]	$C_{11}(C_{12})$[GPa]
GaAs	5.65325	3.88	-1.16	-1.7	1221(566)
AlAs	5.6611	2.90	-2.47	-2.30	1250(534)
InAs	6.0583	2.74	-1.00	-1.80	832.9(452.6)

(Ga,Mn)As layers having the same width $d = 20$nm, while their manganese concentration is different $x = 0.05$ and $x = 0.03$. The exchange energies corresponding to these values are $\Delta_{ex}^{L} = 0.1eV$ and $\Delta_{ex}^{R} = 0.06eV$. A different manganese concentration is used deliberately in order to realize a difference in coercive forces of the two DMS layers. The magnetic layers are separated by a thin layer made of AlAs ($D = 2.8$nm), that acts as a tunneling barrier. The barrier height between GaMnAs and AlAs is estimated to be $V_b = 0.75$eV, while other parameters are the same as in Ref. [146]. Contrary to the usual setups, the structure was grown on a $(In_{0.15}Ga_{0.85})As$ buffer layer in order to introduce tensile strain which makes the spontaneous magnetization M to align along the growth direction.

When calculating the lattice mismatch $(a_s - a)/a$ one needs to take care that values of the lattice constant of $Ga_{1-x}Mn_xAs$ are measured at room

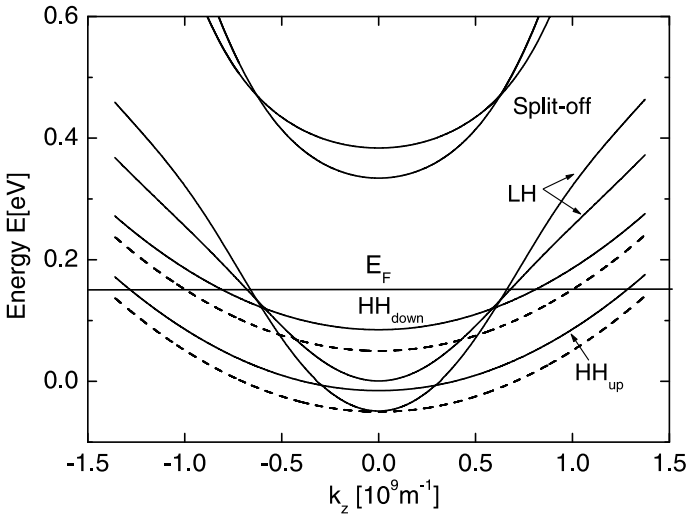

Fig. 5.2 Hole band structure $E(k_z)$ of (Ga,Mn)As for x(Mn)=5%, at the Γ_8 point, in the presence of both strain and magnetic exchange (solid curve), and in the presence of the magnetic moments only (dashed curve). The latter case is given for heavy holes and split-off band only, for clarity.

temperature, since measurements of TMR are done at low temperature ($4.2-77$K). Due to the lack of experimental data on the thermal coefficient for (Ga,Mn)As, we assume it to be the same as for GaAs (the same holds for the Bir-Pikus parameters). On the other hand, the temperature at which the TMR measurement was performed was $T = 20K$, and using the data of Table 5.1, one finds the strain to be $e_1 = 0.0077$ for (Ga,Mn)As and $e_2 = 0.0090$ for AlAs. Notice that in Ref. [101] the same value for e_1 was found. The tunneling magnetoresistance ratio is commonly defined as

$$\mathrm{TMR} = \frac{J_{Cp} - J_{Ca}}{J_{Ca}} = \frac{R_a - R_p}{R_p}\,, \tag{5.13}$$

where the current densities J_{Cp} and J_{Ca} for parallel and antiparallel alignment are found from an integration in k space

$$J_C = \frac{e}{8\pi^3\hbar}\int_0^{k_{\parallel max}} k_\parallel\, dk_\parallel \int_0^{2\pi} d\phi\, \Big(\sum_{\mu\lambda} T_{\mu\lambda}\Big)\,, \tag{5.14}$$

in the limit of small $V_{bias} << \epsilon_F$, and at low temperature $k_BT << \epsilon_F$. Here, $T_{\mu\lambda}$ denotes the transmission amplitude from channel μ to λ, where the indices run over all hole states: $\mu, \lambda \in \{\mathrm{HH1}, \mathrm{HH2}, \mathrm{LH1}, \mathrm{LH2}, \mathrm{SO1}, \mathrm{SO2}\}$. However, only a subset of these channels are usually active depending on the position of the Fermi level E_F relative to $E(k)$. The bandstructure of (Ga,Mn)As in the

vicinity of the Γ_8 point is depicted in Fig. 5.2. The energy dispersion $E(\mathbf{k})$ is given in the [001] k_z direction with the hole energies being positive. The solid curves are the result from a diagonalization of the full Hamiltonian, while the dashed curves correspond to the case when tensile strain ($e = 0.0077$) is absent, for which we show only the HH subbands for clarity. The presence of tensile strain shifts the heavy hole band upwards. The shifts of the energy band edges at $k = 0$ may be obtained analytically and their values are

$$E_{HH} = P_\epsilon + Q_\epsilon \pm \frac{1}{2}\Delta_{ex} \tag{5.15a}$$

$$E_{LH} = \frac{1}{2}\left[2P_\epsilon + \Delta_{SO} - Q_\epsilon - \lambda(\Delta_{SO}^2 \mp 2/3\Delta_{SO}\Delta_{ex}\right. \tag{5.15b}$$

$$\left. + \Delta_{ex}^2 + 2\Delta_{SO}Q_\epsilon \mp 6\Delta_{ex}Q_\epsilon + 9Q_\epsilon^2)^{1/2}\right] \tag{5.15c}$$

$$E_{SO} = \frac{1}{2}\left[2P_\epsilon + \Delta_{SO} - Q_\epsilon + \lambda(\Delta_{SO}^2 \pm 2/3\Delta_{SO}\Delta_{ex}\right. \tag{5.15d}$$

$$\left. + \Delta_{ex}^2 + 2\Delta_{SO}Q_\epsilon \pm 6\Delta_{ex}Q_\epsilon + 9Q_\epsilon^2)^{1/2}\right] \tag{5.15e}$$

where $\lambda = sign(Q_\epsilon)$. The upper(down) signs in front of the exchange energy corresponds to down(up) spin subbands, so that the degeneracy of the valence bands is removed completely and one has six different bands. The offset of heavy holes is simply due to the addition of the exchange energy Δ_{ex} and strain components since they are not coupled to LH or SO bands by the term k_z^2 (inside Q), and their axis quantization is parallel to the magnetization M. In the limit of small spin-orbit coupling Δ_{SO}, the expression for shifts of both SO and LH bands are similiar to Eq. (5.15a). The Fermi level is indicated in Fig. 5.2 by a thin solid line for a hole density $p_h = 2 \cdot 10^{20}\text{cm}^{-3}$. As mentioned earlier, the interplay between the parameters Δ_{ex}, E_F and e (strain) is important for the tunneling process. The variation of the Fermi energy versus hole density is given in Fig. 5.3, along with its values in the absence of tensile strain and magnetic impurities (Mn) (dashed curve), and in the presence of Mn only (dotted curve). Note that the Fermi energy is measured from the unperturbed valence band edge (in the absence of strain/fields). The reason why all three curves lie close to each other is probably coincidental for these particular values of Δ_{ex} and e. For instance, for $p_h = 3.5 \cdot 10^{20}\text{cm}^{-3}$ in pure GaAs we obtained $E_F = 191\text{meV}$ which is very close to the value 195meV calculated by Dietl *et al.*[52].

The hole concentration was not determined in the experiment of Ref. [144] and therefore we used the experimental value for the TMR of 5.5%, to fit the hole density which results into $p_h \approx 2 \cdot 10^{20}\text{cm}^{-3}$, and this in turn leads to a Fermi energy $E_F = 146\text{meV}$ (see Fig. 5.3). The TMR as a function of hole density is given in Fig. 5.4, where the dashed curve is the hypothetical case when strain is absent. The theoretical results are given for a reasonable range

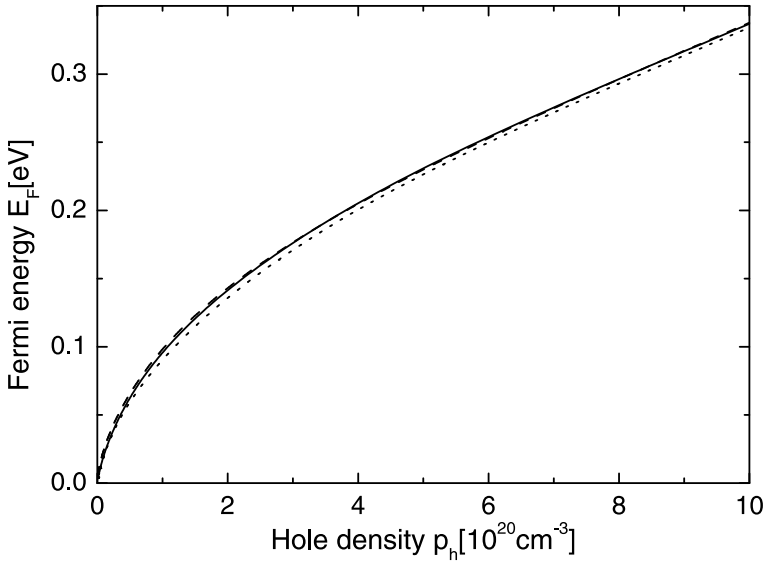

Fig. 5.3 Fermi energy as a function of the hole density in (Ga,Mn)As: (1) with magnetic exchange Δ_{ex} and tensile strain ($e = 0.0077$) included (solid curve), (2) only with exchange Δ_{ex} (dotted curve), and (3) for x(Mn)= 0.0, i.e. pure GaAs without strain (dashed curve).

of hole densities: $(0.5-10)\cdot 10^{20}\mathrm{cm}^{-3}$, where values of p_h of as-grown samples are usually found. The overall trend in both cases is a decrease of TMR with hole density, since the Fermi energy rises making opposite spin subbands more populated. This results in a smaller spin-polarization and thus smaller TMR. Higher TMR at small p_h and E_F, however are not always desirable since currents are then smaller, and more difficult to measure. We found that the theoretical magnetoresistance ratio at the same hole concentration but in the absence of tensile strain is $\mathrm{TMR}_{\mathrm{ns}} = 13.2\%$.

Thus, tensile (biaxial) strain deteriorates TMR for a fixed value of the hole density p_h. This is due to the fact that tensile strain pushes both light hole subbands downwards making the LH opposite spin subband more populated and consequently resulting in a smaller spin-polarization. Of course, both subbands are shifted by approximately the same value, but because of the non-trivial dependence of the transmission amplitude on the energy, the overall result is a smaller magnetoresistance. The trend is opposite for heavy holes, but as they have heavier mass and due to a relatively high potential barrier (≈ 0.75eV) their contribution to TMR is less pronounced. For a comparison we also calculated the TMR in the hypothetical case of compressive strain with the same absolute value, i.e. $e = -0.0077$, and found TMR = 35%. In this case the Fermi energy at the same hole density is $E_F = 130$meV which

is smaller than in previous case. This is expected since HH bands are moved upwards and they have a higher density of states. This high value of TMR for compressive strain is also due to the lower value of the Fermi energy.

The high value of TMR is achieved when, say, spin-up states for heavy and light holes are fully occupied in the emitter, while the same (spin-up) states are depopulated in the collector, in the antiferromagnetic alignment of the two FM layers. As the heavy hole splitting is larger than the light hole splitting, and the Fermi energy is at least 100meV in real structures, this condition can only be met for heavy holes. Thus we can estimate the following bound for the Fermi energy to attain a high TMR

$$E_F < \frac{1}{2}\min\{\Delta_{ex1}, \Delta_{ex2}\} + P_\epsilon + Q_\epsilon \,. \tag{5.16}$$

On the other hand, spontaneous magnetization of the samples is always smaller than the saturation magnetization, which is below the theoretical estimate $M_{max} = xSN_0 g\mu_B B_S(g\mu_B H/(k_B T))$. One of the reasons for $M_{sat} < M_{max}$ is the presence of interstitial $\mathrm{Mn_I}$ that are antiferromagneticaly coupled to substitutional $\mathrm{Mn_{Ga}}$. One normally expects that when the magnetization reaches its ideally maximal value M_{max}, the TMR ratio also increases. This is confirmed by our calculations which are shown in the inset of

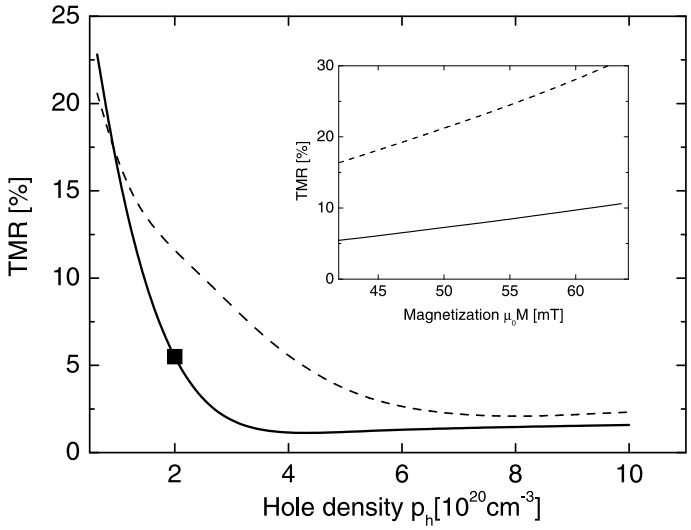

Fig. 5.4 The tunneling magnetoresistance ratio as a function of hole density (solid curve). The dashed curve corresponds to the case when tensile strain is absent, and the closed square is the experimental result from Ref. [144]. Inset: TMR versus magnetization M (in untits of Tesla) in the range from the experimental value 42mT to the theoretically maximal value 64mT (solid curve). As a comparison we also show the TMR for the same structure but grown on a GaAs substrate (dashed curve).

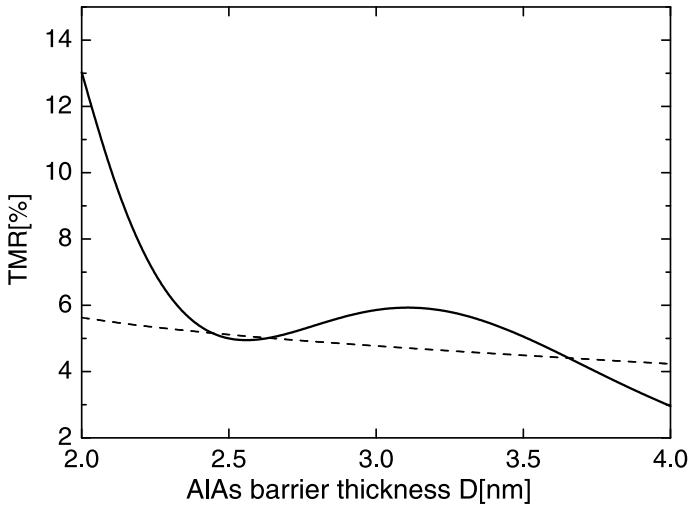

Fig. 5.5 The theoretical value of TMR ratio as a function of AlAs barrier thickness D: obtained by 6×6 $\mathbf{k}\cdot\mathbf{p}$ (solid curve), and by the single band approximation (dashed curve).

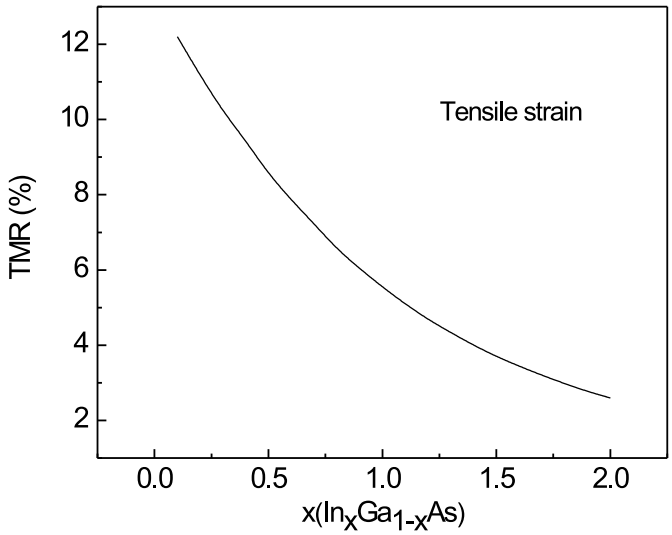

Fig. 5.6 The dependance of tunneling magnetoresistance ratio on the content x(In) in (Ga,In)As. The figure clearly shows that tensile strain deteriorates TMR.

Fig. 5.4, where the TMR is given as a function of $\mu_0 M \in (\mu_0 M_{exp}, \mu_0 M_{max}) = (42\text{mT}, 64\text{mT})$, for a fixed value of the Fermi energy $E_F = 146\text{meV}$. For comparison, we calculated the TMR also for the case of in-plane magnetization, and compressive strain $e_1 = 0.28\%$ as if the structure was grown on a GaAs substrate. This result is shown in the same figure by the dashed curve. The magnetoresistance ratio obtained was $\text{TMR}_{\|} = 16\%$ and $\text{TMR}_{\|0} = 15.4\%$ in the absence of strain for $\mu_0 M = 42mT$. The higher value of TMR for in-plane magnetization is in accord with the conclusions of Ref. [137] that holes exhibit higher polarization when M is parallel to the layers. We also present the results of TMR for tensile strain but as a function of AlAs barrier thickness which is varied in the range $D \in (2, 4)\text{nm}$ (Fig. 5.5) (solid curve), along with the result of the single band approximation (dashed curve) when heavy and light holes states are treated independently of each other. The values in general decrease with D, while there is a small maximum for $D = 3.1\text{nm}$. This maximum is lacking in the single band approximation, which indicates that strong band-mixing between the heavy and light holes takes place in the barrier[140], and that there exists an optimal value of its width when TMR attains a maximum. This comparison also clearly shows the limitations of the single band approximation in case of hole tunneling. At the end, TMR as a function of the In content in the InGaAs substrate layer is given on Fig.5.6. This dependance clearly shows the negative effect of tensile strain on magnetoresistance of trilayer structures.

5.4 DOUBLE BARRIER MAGNETIC TUNNEL JUNCTION

Next we turn our attention to double barrier magnetic tunnel junctions (MTJ), which consists of two nonmagnetic barriers separated by a semiconductor, while the emitter and collector leads are made of diluted magnetic semiconductors. TMR experiments on such a structure were recently reported in Ref. [147]. It consists of two $(Ga_{0.94}Mn_{0.06})As$ layers with the same thickness, 20 nm, acting as emitter and collector, while in between a double barrier heterostructure AlAs(D nm)/$(In_{0.4}Ga_{0.6})$As/AlAs(D nm) (see Fig. 5.7) is placed. The choice of (In,Ga)As as a material for the well is to ensure that at least one bound state lies below the Fermi energy, so that only a small bias voltage is needed to realize resonant tunneling. This layer is under compressive strain, which adds about 80meV to the band-offset (relative to pure GaAs). There is also a shift due to strain which for heavy holes amounts to 120meV. Thus, the heavy hole bands lies approximately 200meV below the Fermi level.

First, we calculated the TMR using the 4×4 $\mathbf{k}\cdot\mathbf{p}$ model including exchange and taking the parameters of Ref. [147]: exchange energy $\Delta_{ex} = 240\text{meV}$, Fermi energy $E_F = 150\text{meV}$. Note that here Δ_{ex} denotes the heavy hole splitting which is three times larger than the light hole splitting which was used as a parameter in Ref. [147], while the reference level of the Fermi energy is the unperturbed valence band edge (Γ_8). Our theoretical results are

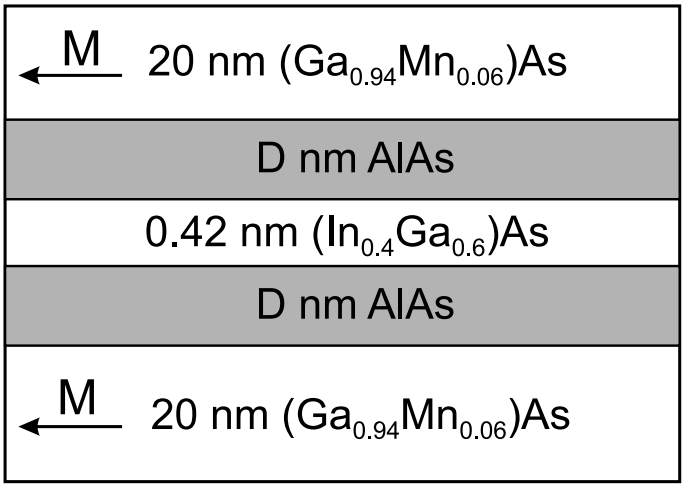

Fig. 5.7 Double barrier magnetic tunnel junction made of two ferromagnetic (Ga,Mn)As layers, acting as emitter and collector, two AlAs barriers, while the well is made of $In_{0.4}Ga_{0.6}As$.

shown in Fig. 5.8 (dashed curve), and they are similar to the values obtained in Ref. [147]. Notice that there is a rapid increase of the TMR after $D > 0.7$nm, which indicates that efficient resonant tunneling takes place when the thickness of the barriers is large enough. This is expected since only for sufficiently thick barriers one can expect the formation of a quasibound state in the well. However, the 4×4 $\mathbf{k} \cdot \mathbf{p}$ model neglects spin-orbit interaction which was proven[136] to have a significant effect on TMR in double barrier structures, when DMS layers are used. Therefore we extended our calculations to the 6×6 $\mathbf{k} \cdot \mathbf{p}$-theory (as in the previous section) whose results are also shown in Fig. 5.8 but as a solid curve. The values are significantly smaller than in the simpler case when only heavy and light holes are included especially for larger thicknesses of the AlAs barriers D. Furthermore, the TMR exhibits an oscillatory behaviour as a function of D. This is in qualitative agreement with the conclusions of Ref. [136].

5.5 CONCLUSIONS

We have investigated spin-dependent tunneling through a diluted magnetic semiconductor trilayer structure under the influence of tensile strain, when the magnetization is perpendicular to the layers. It is shown that the $\mathbf{k} \cdot \mathbf{p}$ model can semi-quantatively describe the tunneling processes through the barrier made of AlAs. Tensile strain resulting from the substrate, made of

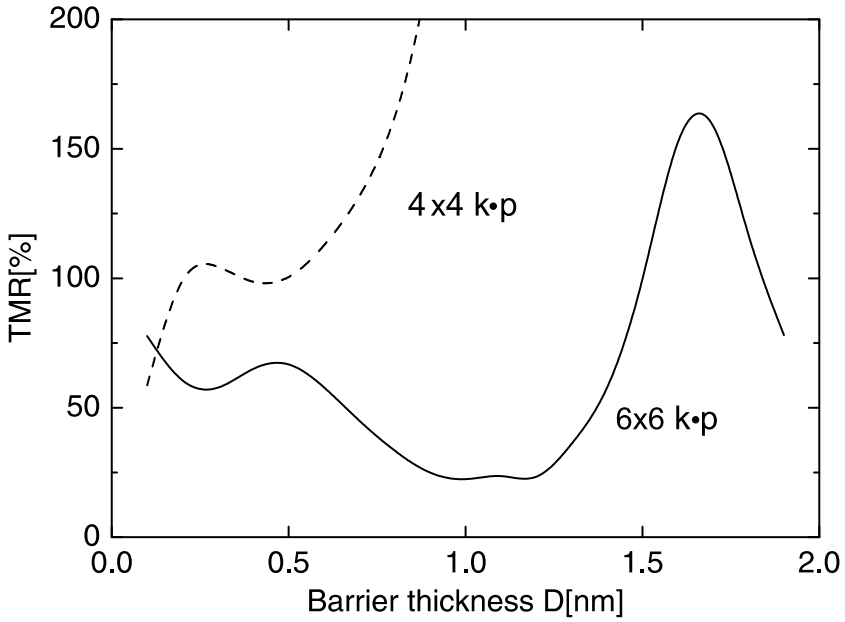

Fig. 5.8 The tunneling magnetoresistance ratio as a function of AlAs barrier thickness D in a double barrier MTJ (Ga,Mn)As/AlA/$In_{0.4}Ga_{0.6}As$/AlAs/(Ga,Mn)As, obtained using 6×6 $\mathbf{k} \cdot \mathbf{p}$ theory (solid curve) and using 4×4 $\mathbf{k} \cdot \mathbf{p}$ (dashed curve).

(In,Ga)As, diminishes the tunneling magnetoresistance as it pushes the subbands of light holes downwards making them less spin polarized, while the influence of compressive strain is opposite. The contribution of light holes to TMR for the considered values of the barrier height and Fermi energy, is larger than that of heavy holes due to their light mass. Since in Ref. [144] there are no detailed data on the hole concentration in the (Ga,Mn)As layers we presented our results as a function of p_h within a range of estimated upper and lower bounds. Though the experimental value of $\mathrm{TMR_{exp}} = 5.5\%$ can be fitted for $p_h \approx 2 \cdot 10^{20}\mathrm{cm}^{-3}$, it is not sufficient to draw any conclusions on the reliability of the method. However, this value of the hole concentration is in accord with values measured for as-grown samples. For instance, it was determined that an as-grown sample from Ref. [156] with slightly higher Mn concentration $x = 5.3\%$ has $p_h = 3.5 \cdot 10^{20}\mathrm{cm}^{-3}$. As for the case of a double barrier magnetic tunnel junction, treated in Sec. 5.4, we find that spin-orbit interaction reduces significantly the value of the TMR, and makes it a non-monotonous function of the AlAs barrier thickness. The predictions of the simple 4×4 $\mathbf{k} \cdot \mathbf{p}$ theory that TMR may reach $10^4\%$ or even larger, are shown to be unrealistic by employing the more accurate 6×6 $\mathbf{k} \cdot \mathbf{p}$ model, that limits TMR to 160% when the AlAs barrier thickness is varied. How-

ever, these values are still larger than determined by experiment[147]. The possible reasons for the discrepancy between the model and the experimental data are: violation of in-plane momentum conservation as a result of scattering on Mn impurities on the (Ga,Mn)As/AlAs interface, presence of Mn in AlAs (interdiffusion of Mn), and the influence of the tunneling anisotropical magnetoresistance (TAMR)[157, 158]. The role of TAMR is still a controversial issue, as other authors[134, 159] claimed that its influence is not very pronounced. For instance, Saito *et al.*[159] estimated that the contribution of TAMR to the total TMR_{tot} in a trilayer (Ga,Mn)As/ZnSe/(Ga,Mn)As is only about 10%.

6

Appendix: Green's functions for the magnetic exchange

The system of four Dyson equations for the d-electron Green functions $G^{\sigma}_{dii'}$ (i, i') has the following form within the Hartree approximation:

$$G^{\sigma}_{dii'}(\varepsilon) = g_{d\sigma}(\varepsilon)\left(\delta_{ii'} + \sum_{\mathbf{pp'}}\sum_{j=1,2} V_{\mathbf{p}d}V^{*}_{\mathbf{p'}d}e^{-i\mathbf{p}\cdot\mathbf{R}_i}G^{\sigma}_{\mathbf{pp'}}e^{i\mathbf{p'}\cdot\mathbf{R}_{i'}}G^{\sigma}_{dji'}\right). \quad (6.1)$$

Here

$$g_{d\sigma}(\varepsilon)\delta_{ij} = (\varepsilon - E_d - Un_i^{-\sigma} + i\delta\mathrm{sign}(\varepsilon-\mu))^{-1}\delta_{ij}\,, \quad (6.2)$$

is the bare single site d-electron Green function for the $t_2\sigma$ electron centered at the ion i, taken in the Hartree approximation, and μ is the chemical potential. The diagram of this system of Dyson equation is shown on Fig. 6.1. The Green function $G^{\sigma}_{\mathbf{pp'}}$ describes the spectrum of the valence band electrons modified by the two-impurity short-range potential scattering. It satisfies the Dyson equation

$$G^{\sigma}_{\mathbf{pp'}}(\varepsilon) = g_{\mathbf{p},\sigma}(\varepsilon)\delta_{\mathbf{pp'}} + g_{\mathbf{p},\sigma}(\varepsilon)\sum_{\mathbf{p''}} W_{\mathbf{pp''}}e^{i(\mathbf{p}-\mathbf{p''})/\hbar\mathbf{R_i}}G^{\sigma}_{\mathbf{p''p'}}(\varepsilon)\,, \quad (6.3)$$

where

$$g_{\mathbf{p},\sigma}(\varepsilon) = (\varepsilon - \varepsilon_{\mathbf{p}} + i\delta\mathrm{sign}(\varepsilon-\mu))^{-1}\,. \quad (6.4)$$

All the above equations give linear relations between the Green functions. We may rewrite equation (6.3) using shorthand notations for the Green function matrices

$$\mathsf{G}_b = \mathsf{A}\cdot\mathsf{g}_b\,, \quad (6.5)$$

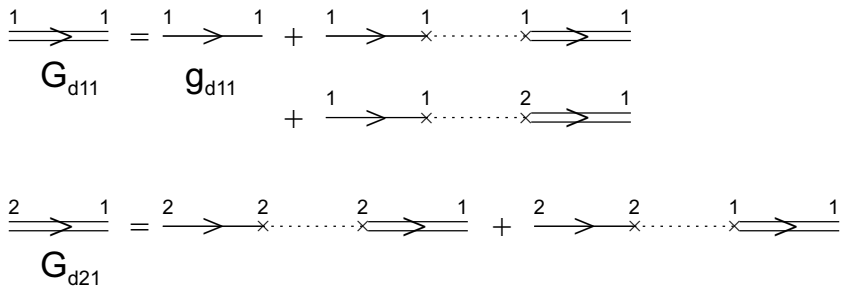

Fig. 6.1 Diagram for the system of Dyson equations for d-electrons: single (full) line corresponds to single site d-electron Green's function $g_{d\sigma}$, while dotted line corresponds to the band electrons $G_{\mathbf{p}\mathbf{p}'}$

where g_b stands for the diagonal matrix (6.4). Equations (6.1) and (6.3) take the form

$$\mathsf{G} = \mathsf{B} \cdot \mathsf{g}_0 \,, \tag{6.6}$$

where

$$\mathsf{g_0} = \begin{pmatrix} \mathsf{G_b} & 0 \\ 0 & \mathsf{g_d} \end{pmatrix}.$$

with g_d being a 2×2 matrix (6.2). The explicit expressions for the matrices A and B can be readily found from the Dyson equations (6.1) and (6.3).

For further calculations we need determinants of the matrices A and B,

$$\mathsf{Q}(\varepsilon) \equiv \det \mathsf{A} = \mathsf{q}(\varepsilon)^2 - W^2 L_{12}(\varepsilon) L_{21}(\varepsilon) \,, \tag{6.7}$$

where

$$\mathsf{q}(\varepsilon) = 1 - W L_{11}(\varepsilon)$$

and

$$L_{ij} = \sum_{\mathbf{p}} g_p e^{-i\mathbf{p}\cdot(\mathbf{R}_i - \mathbf{R}_j)} \,, \tag{6.8}$$

is the lattice Green function. It is assumed that that two Mn impurities are identical, i.e. $L_{11} = L_{22}$. The second determinant is

$$\mathsf{R} \equiv g_d^{-2}(\varepsilon) \det \mathsf{B} = [g_d^{-1}(\varepsilon) - V^2 M_{11}^{\sigma}(\varepsilon)]^2 - V^4 M_{12}^{\sigma}(\varepsilon) M_{21}^{\sigma}(\varepsilon). \tag{6.9}$$

Here

$$M_{11}^{\sigma} = \sum_{\mathbf{p}\mathbf{p}'} e^{-i(\mathbf{p}-\mathbf{p}')\cdot\mathbf{R}_1} G_{\mathbf{p}\mathbf{p}'}^{\sigma} = L_{11} + W\mathsf{Q}^{-1}[L_{11}^2\mathsf{q} + L_{12}L_{21}\mathsf{q} + 2WL_{11}L_{12}L_{21}]. \tag{6.10}$$

M^{σ}_{22} is obtained from Eq. (6.10) by exchanging indices 1 and 2, and

$$M^{\sigma}_{12} = \sum_{\mathbf{pp'}} e^{-i\mathbf{p}\cdot\mathbf{R}_1 + i\mathbf{p'}\cdot\mathbf{R}_2} G^{\sigma}_{\mathbf{pp'}} = L_{12} + W\mathsf{Q}^{-1}[L_{12}L_{11}\mathsf{q} + L_{21}L_{11}\mathsf{q} + WL^2_{21}L_{12}]. \tag{6.11}$$

Till now the calculations were made neglecting the orbital degeneracy of the impurity d states and within the Hartree approximation. We can generalize these calculations using the Hubbard I approximation for the d-electron Green functions (see, e.g., Ref. [84]). We assume also that the three-fold degeneracy of the impurity t_{2g} is not lifted and the relevant physical quantities do not depend on the index μ enumerating these three states. The algebraic structure of the Dyson equation is still the same as in (6.1). Then considering the interaction of two three-fold degenerate states belonging to the two impurities. This leads to the 6×6 matrix

$$\mathsf{B'}_{i\mu,j\mu'} = \begin{pmatrix} a & 0 & 0 & b & b & b \\ 0 & a & 0 & b & b & b \\ 0 & 0 & a & b & b & b \\ b & b & b & a & 0 & 0 \\ b & b & b & 0 & a & 0 \\ b & b & b & 0 & 0 & a \end{pmatrix} \tag{6.12}$$

where

$$a = g_d^{-1}(\varepsilon) - V^2 K M^{\sigma}_{11}(\varepsilon), \quad b = V^2 K M^{\sigma}_{12}(\varepsilon)\,, \tag{6.13}$$

and $K = n_{d^5} + n_{d^4}$. n_{d^5} is the probability that the impurity d-shell is in the nondegenerate d^5 state, whereas n_{d^4} is the probability that the impurity d-shell is in one of the three degenerate d^4 states. Calculating now the determinant of the matrix (6.12) one gets the equation

$$\mathsf{R} \equiv a^{-4} \det \mathsf{B'} = [g_d^{-1}(\varepsilon) - V^2 K M^{\sigma}_{11}(\varepsilon)]^2 - 9V^4 K^2 M^{\sigma}_{12}(\varepsilon) M^{\sigma}_{21}(\varepsilon)\,. \tag{6.14}$$

which should be used instead of Eq. (6.9).

The occupation numbers n_{d5} and n_{d4} for the Hubbard-like states obey non-Fermi statistics, whose specific form in the case considered here is

$$n_{d5} = \frac{f(E_{CFR} - \mu)}{3 - 2f(E_{CFR} - \mu)}, \quad n_{d4} = \frac{1 - f(E_{CFR} - \mu)}{3 - 2f(E_{CFR} - \mu)}\,. \tag{6.15}$$

If the chemical potential lies below the impurity level E_{CFR} of the fifth electron in the d-shell then the Fermi distribution $f(E_{CFR} - \mu)$ is zero at low temperatures and $n_{d5} = 0,\ n_{d4} = 1/3$, meaning that $K = 1/3$. If $E_{CFR} < \mu$ then $n_{d5} = 1,\ n_{d4} = 0$, and $K = 1$.

The energy (2.7) can be found using the general property of the Green functions, connecting their trace and determinant

$$\mathrm{Tr}\ \mathsf{G}(\varepsilon) = \frac{d}{d\varepsilon} \ln \det \mathsf{G}(\varepsilon) \tag{6.16}$$

Then using Eqs. (6.7), (6.9), and (6.16) allows one to rewrite Eq. (2.7) in the following form

$$\Delta E = \mathrm{Im}\int_{-\infty}^{\infty}\frac{d\varepsilon}{2\pi}\varepsilon\frac{d}{d\varepsilon}\left[\ln \mathsf{R}^{\sigma}(\varepsilon)+\ln \mathsf{Q}^{\sigma}(\varepsilon)\right] = -\mathrm{Im}\int_{-\infty}^{\infty}\frac{d\varepsilon}{2\pi}\left[\ln \mathsf{R}^{\sigma}(\varepsilon)+\ln \mathsf{Q}^{\sigma}(\varepsilon)\right]. \tag{6.17}$$

The functions R and Q depend on the combination $\varepsilon - i\mathrm{sign}(\varepsilon-\mu)$, hence the integration contour in (6.17) can be deformed in such a way as to embrace the cut from the band states and all the poles due to the localized levels with the energies below the chemical potential μ, i.e. occupied states. Then equation (6.17) transforms into (2.8).

Next we consider a property of Eq. (6.17), which will simplify the calculation of the energy and provides a better intuition for the results. Our model includes all the levels belonging to the valence band with the addition of the impurity d-levels, which interact with the band levels. Let us assume that at zero temperature the chemical potential lies higher than all these levels, meaning that they are all occupied. Then the total energy of the system is

$$E_{tot} = \mathrm{Tr}\widehat{H}. \tag{6.18}$$

In order to calculate this trace, we may represent the operator $\widehat{H}$ in matrix form using the noninteracting band states with the addition of the atomic d-functions as the basis. Then the hybridization matrix elements will appear only in the off-diagonal positions of this matrix, which do not influence the result. The conclusion is that the energy E_{tot} does not depend on the value of the hybridization.

The potential scattering, $W_{\mathbf{pp}}$, contributes to the diagonal elements of the Hamiltonian and may influence the value of E_{tot}. However, we are interested here only in the indirect exchange between the impurities. It can be found if we consider the energy $\Delta E(R_{ij})$ and subtract from it the energy corresponding to two noninteracting impurities,

$$\Delta E_{ex} = -\frac{1}{\pi}\mathrm{Im}\int_{\varepsilon_{hb}}^{\mu} d\varepsilon\left[\ln\frac{\mathsf{R}^{\sigma}(\varepsilon)}{\mathsf{R}_0^{\sigma}(\varepsilon)}+\ln\frac{\mathsf{Q}^{\sigma}(\varepsilon)}{\mathsf{Q}_0^{\sigma}(\varepsilon)}\right]+\Delta E_{loc}(\varepsilon<\mu)\,. \tag{6.19}$$

where $\mathsf{Q}_0^{\sigma}(\varepsilon)$ and $\mathsf{R}_0^{\sigma}(\varepsilon)$ are obtained from (6.7) and (6.9) under the assumption that $L_{12}=L_{21}=0$. $\Delta E_{loc}(\varepsilon<\mu)$ is the corresponding change of the energies of the occupied localized levels. Now we may conclude that the sum (6.19) over all occupied states is equal to the same sum over all empty states, but with the opposite sign. Hence,

$$\Delta E_{ex} = \frac{1}{\pi}\mathrm{Im}\int_{\mu}^{\varepsilon_{ht}} d\varepsilon\left[\ln\frac{\mathsf{R}^{\sigma}(\varepsilon)}{\mathsf{R}_0^{\sigma}(\varepsilon)}+\ln\frac{\mathsf{Q}^{\sigma}(\varepsilon)}{\mathsf{Q}_0^{\sigma}(\varepsilon)}\right]-\Delta E_{loc}(\varepsilon>\mu). \tag{6.20}$$

Here $\Delta E_{loc}(\varepsilon>\mu)$ includes the empty localized levels (if any) lying above the chemical potential. These levels appear due to the combined action of both

potential (W) and resonance (V) scattering mechanisms. Formally they can be found as zeros of the determinant R (See Eq. (6.9)).

To find the contribution of the localized states to the magnetic energy one should simply calculate the level positions modified by the effective inter-impurity exchange via empty states and their occupation. We consider here two limiting cases.

First, we estimate the contribution of CFR levels, if they happen to lie within the forbidden energy gap. It means that we may expand the function $\mathsf{R}(\varepsilon)$ close to the energy $E^0_{CFR\sigma}$ of the isolated CFR level determined by the equation

$$E^0_{CFR} = E_d + KV^2 P_{11}\left(E^0_{CFR}\right), \tag{6.21}$$

which describes the TM d-levels renormalized by their hybridization with the hh band. Indirect inter-impurity interaction results in splitting of two-impurity states and a shift of localized states relative to the hh band. These levels lie in the discrete part of the spectrum, where the imaginary part of the Green function (2.11) $\Gamma_{ij} = 0$. Neglecting potential scattering, one obtains the equation

$$\mathsf{R} = [\varepsilon - E_d - KV^2 P^\sigma_{11}(\varepsilon)][\varepsilon - E_d - KV^2 P^\sigma_{22}(\varepsilon)] - 9K^2V^4 P^\sigma_{12}(\varepsilon)P^\sigma_{21}(\varepsilon) = 0\,, \tag{6.22}$$

for the two-impurity poles in the energy gap. The solution of Eq. (6.22) is looked for in the form $E_{CFR} = E^0_{CFR} + \delta E_{CFR}$. Now we expand the function $\mathsf{R}(E^0_{CFR} + \delta E_{CFR})$ up to the second order terms with respect to δE_{CFR} and arrive at Eq. (2.17).

Second, we consider the case when the DBH levels lie in the forbidden energy gap. Then the potential scattering W is the leading cause of the creation of the deep level. The energy of an isolated DBH level corresponds to a zero of the function

$$\mathsf{q}(E^0_{DBH}) = 1 - WP_{11}(E^0_{DBH}) = 0\,. \tag{6.23}$$

Then we look for zeros of the function $\mathsf{R}(\varepsilon)$ at the energy $E_{DBH} = E^0_{DBH} + \delta E_{DBH}$. Accounting for the fact that both functions q and Q are small in the vicinity of the energy E^0_{DBH} the equation $\mathsf{R} = 0$ can be approximately rewritten in the form

$$\left\{\mathsf{q}^2 - W^2P^2_{12} - \frac{KV^2}{\Delta E}W[P^2_{11}\mathsf{q} + P^2_{12}\mathsf{q} + 2WP_{11}P^2_{12}]\right\}^2 = \tag{6.24}$$

$$\frac{9K^2V^4}{\Delta E^2}\left\{P_{12} + W[2P_{12}P_{11}\mathsf{q} + WP^2_{12}]\right\}^2 \tag{6.25}$$

with $\Delta E = E^0_{DBH} - E_d - V^2P_{11}$. All the functions P_{ij} are now calculated at $\varepsilon = E^0_{DBH}$. We first neglect the r.h.s term in Eq. (6.24) and solve the quadratic equation

$$\mathsf{q}^2 - \frac{KV^2}{\Delta E}W[P^2_{11} + P^2_{12}]\mathsf{q} - W^2P^2_{12} - \frac{2KV^2W^2}{\Delta E}P_{11}P^2_{12} = 0\,. \tag{6.26}$$

From here we obtain Eq. (2.21) for the energy shifts due to interaction between the two degenerate DBH levels.

When both these levels are empty we obtain a contribution to the kinematic exchange by summing these two energies, extracting from them the part due to the hybridization with the impurity d-states, and changing the sign in the hole representation,

$$\Delta E_{DBH,ex} = \frac{KV^2 P_{12}^2}{\Delta E P'_{11}} \ . \tag{6.27}$$

Accounting for the rhs of Eq. (6.24) will result in higher order corrections, which can be neglected.

7

Summary

In the first chapter of the thesis a general introduction to the emerging field of spintronics is given, with particular attention to diluted magnetic semiconductor materials. One of the most studied DMS material is (Ga,Mn)As, both from an experimental and a theoretical point of view, due to its possible applications in the existing semiconductor technology developed for GaAs. An overview of important properties of (Ga,Mn)As is given based on the contemporary literature and experimental data, such as growth, transport, magnetic properties of (Ga,Mn)As epilayers, electronic structure of Mn acceptor level, etc. Since the subject of the thesis is the theoretical investigation of magnetic and transport properties of DMS, a brief survey of the most important models which have been proposed to explain the ferromagnetism in (Ga,Mn)As is given. These encompass both microscopic and phenomenological theories, as well as *ab initio* calculations.

In the next chapter, a microscopic model of ferromagnetism is presented. It is based on Anderson model of magnetism for two magnetic impurities in metals but here modified for the case of a semiconductor, where the presence of the band gap and impurity levels introduce more features in the model. Since the concentration of Mn in III-V DMS is low, it is sufficiently to consider only two neighbouring impurities to catch the principal physics. According to the model the indirect exchange between the two impurities proceeds via unoccupied valence states, through $p-d$ hybridization characterized by the integral $V_{\mathbf{p}d}$. Since hybridization preserves spin, and the Hund rule forbids hopping on another impurity with the "wrong" spin, exchange is possible only if the d electrons of the two impurities have parallel spin. This mechanism favors ferromagnetism if there are sufficient unoccupied levels in the valence

band, i.e. if there is enough holes present. This is in accordance with the accepted belief that ferromagnetism in III-V DMS is hole mediated. The energy gain during this exchange is connected to the Curie temperature through the mean-field approximation. A very good agreement with experimental data is obtained for the dependance T_C on the hole density p_h for fixed manganese concentration. As far as $T_C(x)$ is concerned, a good agreement with experimental values from different research groups is achieved through a fitting of the hybridization $V_{\mathbf{p}d}$. This is acceptable as the quality and concentration of defects vary from sample to sample.

The remaining part of the thesis is concerned with the theoretical investigation of tunneling through structures made of DMS. This is important in connection with possible application of DMS materials in spin-valve devices, magnetic read heads, magnetic memories. Modern devices employ only metallic ferromagnets, such as Fe, Co or Ni, since their ferromagnetic order persist up to temperatures much higher than room temperature. On other hand, trilayer structures made of (Ga,Mn)As and GaAs (and/or AlAs) exhibits higher magnetoresistance ratio, i.e. modulation of the resistance under an applied external magnetic field. This can be critical in read heads of hard disks since the reliability and speed of reading of data reading may be improved with the usage of DMS instead of metallic ferromagnets, especially given the fact that the storage density of modern hard disks is extended close to their physical limits. However before going to this issue it is important to clarify the hole tunneling in non-magnetic semiconductor structures, since this problem is treated in the literature with insufficient accuracy, from a theoretical point of view in the literature. This is the subject of **chapter 3**. A double barrier resonant structure is chosen that consists of two AlAs layers acting as barriers and one layer of GaAs placed in between. Since the layer thicknesses (barrier and well) are thick enough (more than $2 - 3$nm) the effective mass model for holes, i.e. $\mathbf{k} \cdot \mathbf{p}$ theory is used to evaluate the transmission and reflection coefficients, current, and most importantly polarization. It is found that light holes contribute more to the current since they 'tunnel' easier due to their lighter mass. It is shown that under magnetic field applied perpendicular to the growth axis that both heavy and light holes precess. Normally, heavy holes can not precess since they have well defined spin along the growth axis, but band-mixing lifts this 'selection rule' for $\mathbf{k} \neq 0$. i.e. away from the center of the Brillouin zone. This can be explained by the fact that the expectation value of the angular momentum of heavy holes drops below the nominal value of $3/2$, as a consequence of mixing with light holes. Polarization of the current exhibits oscillatory behavour with the well width W.

The following chapter, **chapter 4** is concerned with spin-dependant tunneling through trilayer structures made of two (Ga,Mn)As layers, where AlAs or GaAs acts as a barrier. As mentioned earlier in the text, these trilayer structures may be used as an ingredient of read heads of hard disks in the future if the Curie temperature of (Ga,Mn)As is raised above room temperature. As in previous chapter, $\mathbf{k} \cdot \mathbf{p}$ theory for holes is used but with inclusion of

the Giant Zeeman Term, that is, the mean field approximation of the $p-d$ exchange integral. As a reference, the experimental data from Higo and Tanaka from 2001, Ref.[132], was used. They achieved tunneling magnetoresistance (TMR) up to 75% in their trilayer structure made of two (Ga,Mn)As and AlAs layers in a wedge shape in order to probe TMR as a function of the barrier width D. The theory predicts the correct order of magnitude but much slower decay of TMR with the barrier D than the experiment. This is expected given the fact that no fitting parameter was present in the model, and that only resonant (coherent) tunneling is taken into account. The reasons for this discrepancy could be due to the negligence of inelastic scattering on the interfaces (Ga,Mn)As/AlAs, possible tunneling through defect states in the band-gap, the presence of Mn atoms in the AlAs barrier as a result of interdiffussion, etc. Furthermore, the interaction between d electrons and hole bands is taken in the mean field approximation, and the change of the density of states due to the presence of an open d-shell is also neglected. Further and a more detailed investigation may be the inclusion of inelastic scattering on the interfaces by allowing violation of the conversion of in-plane momentum conversion. A phenomenological parameter that would characterize the scattering could be determined from experimental data on GaAs/AlAs/GaAs structure without the presence of Mn atoms, serving as a control sample. In this manner, one would avoid a fitting procedure. On the other hand, a more detailed band structure can be taken into account by employing a tight-binding model such as $sp^3s^*d^5$. In the next chapter, chapter 5, the influence of strain on the TMR of trilayer structures is investigated. The structure of interest is (Ga,Mn)As/AlAs/(Ga,Mn)As but now grown on InGaAs that builds in a tensile strain due to the lattice mismatch of GaAs and InGaAs. The tensile strain makes the easy axis of magnetization oriented along the growth axis. It turns out that tensile strain deteriorates TMR. The effect of strain is threefold: the change of easy axis, the change of the Fermi level due to the redistribution of holes in the subbands, and heavy and light hole bands are shifted in opposite manner. For instance, light hole subbands are shifted downwards making them less polarized. As shown in the last two chapters light holes contribute more to the current, and to TMR, and this can explain the lower value of the magnetoresistance ratio of trilayer structures grown on InGaAs. Due to the lack of experimental data on the hole density, it was not possible to give a theoretical estimate for TMR for this particular sample. Actually, the hole density was obtained by fitting the experimental value of the magnetoresistance ratio, and its value is typical for as-grown samples for that particular manganese concentration.

8

Samenvatting

In het eerste hoofdstuk van de thesis wordt een algemene inleiding tot het opkomende veld spintronica, met specifieke aandacht voor verdunde magnetische halfgeleidermaterialen (VMH), gegeven. Eén van de meest bestudeerde VMH materialen is (Ga,Mn)As, zowel vanuit experimenteel als vanuit theoretisch oogpunt, en dit omwille van mogelijke toepassingen in de bestaande halfgeleidertechnologie, ontwikkeld voor GaAs. Op basis van de hedendaagse literatuur en experimentele gegevens wordt een overzicht gegeven van belangrijke eigenschappen van (Ga,Mn)As, zoals groei, transport, magnetische eigenschappen van (Ga,Mn)As epitaxale lagen, electronische structuur van het Mn acceptorniveau etc. Aangezien het onderwerp van de thesis is theoretisch onderzoek over de magnetische- en transporteigenschappen van VMH is, en daarom en verklaring van wordt een kort overzicht gegeven van de belangrijkste gangbare modellen, die werken voorgesteld ter verklaring van het ferromagnetisme in (Ga,Mn)As te verklaren. Deze omvatten zowel microscopische en fenomenologische theorieën, als *ab initio* berekeningen. In het volgende hoofdstuk wordt een microscopisch model over ferromagnetisme voorgesteld. Het is gebaseerd op Andersons' model van magnetisme voor twee magnetische onzuiverheden in metalen, maar hier aangepast voor het geval van een halfgeleider, waar de aanwezigheid van de bandkloof en onzuiverheidsniveaus meer karakteristieke eigenschappen introduceren in het model. Gezien de concentratie van Mn in de III-V VMH klein is, volstaat het om slechts twee naburige onzuiverheden in aanmerking te nemen om de voornaamste fysica te bevatten. Volgens het model verloopt de indirecte wisselwerking tussen de twee onzuiverheden via lege valentietoestanden, door $p-d$ hybridisatie gekarakteriseerd door de $V_{\mathbf{p}d}$ integraal. Gezien de hybridisatie de

spin behoudt en de Hund regel het verspringen naar een andere onzuiverheid met 'foute' spin verbiedt, is de uitwisseling enkel mogelijk als de d elektronen van de twee onzuiverheden een parallelle spin hebben. Dit mechanisme bevordert ferromagnetisme als er genoeg onbezette niveaus in de valentieband zitten, d.w.z. als er voldoende gaten aanwezig zijn. Dit is in overeenstemming met het aanvaarde geloof dat ferromagnetisme in een III-V VMH gemedieerd wordt doormiddel van gaten. De energiewinst gedurende deze uitwisseling is verbonden met de Curie temperatuur door de gemiddeld-veld benadering. Een zeer goede overeenkomst met experimentele gegevens wordt verkregen voor de afhankelijkheid van T_C met de gaten dichtheid p_h voor een vaste mangaanconcentratie (x). Voor zover betreft $T_C(x)$ wordt een goede overeenkomst met experimentele waarden van verschillende onderzoeksgroepen bereikt door het fitten van de hybridisatie $V_{\mathbf{p}d}$. Dit is aanvaardbaar gezien de kwaliteit en de concentratie van defecten wisselen van staal tot staal.

Het resterende deel van de thesis betreft theoretisch onderzoek van tunneling door structuren gemaakt van VMH. Dit is van belang in verband met de toepassing van VMH materialen in spin-klep toestellen, magnetische leeskoppen en magnetische geheugens. Moderne toestellen gebruiken enkel metallische ferromagneten, zoals Fe, Co of Ni, omdat hun ferromagnetische ordening standhoudt tot temperaturen boven kamertemperatuur. Van de andere kant vertonen drielagige structuren gemaakt van (Ga,Mn)As en GaAs (en/of AlAs) een hogere magnetoweerstandverhouding, d.w.z. modulatie van de weerstand onder een aangelegt extern magnetisch veld. Dit kan cruciaal zijn in leeskoppen van voor harde schijven omdat de betrouwbaarheid en de snelheid waarmee gegevens gelezen worden verbeterd zouden kunnen worden met het gebruik van VMH i.p.v. metallische ferromagneten, in het bijzonder gezien het feit dat de opslagdichtheid van moderne harde schijven tot dicht bij de fysische grenzen is gerekt. Hoe dan ook, voor we dit onderwerp behandelen is het van belang de gat tunneling in niet magnetische halfgeleiderstructuren te verduidelijken, aangezien dit probleem vanuit theoretisch oogpunt niet genoeg behandeld is in de literatuur. Dit is het onderwerp van hoofdstuk 3. Er wordt gekozen voor een dubbele resonante structuur, die bestaat uit twee AlAs lagen die zich gedragen als barrière en één laag van GaAs die ertussen geplaatst wordt. Gezien de laagdiktes voldoende dik genoeg zijn (meer dan 2-3 nm) wordt het effectieve massa model, d.w.z. de $\mathbf{k} \cdot \mathbf{p}$ theorie gebruikt om de transmissie- en reflectiecoëfficiënten, stroom, en het allerbelangrijkste, de polarisatie te berekenen. We vonden dat de lichte gaten meer bijdragen aan de stroom omdat ze gemakkelijker 'tunnelen', dankzij hun lichtere massa. Onder een loodrecht magnetisch veld, loodrecht toegepast op de groei as, vertonen zowel zware als lichte gaten precessie. Normaal gezien kunnen zware gaten geen spin precessie ondergaan omdat ze een goed gedefinieerde spin hebben langs de groeirichting, maar band-mixing heft deze 'selectieregel' op voor $\mathbf{k} \neq 0$ d.w.z. weg van het centrum van de Brillouin zone. Dit kan verklaard worden door het feit dat de verwachte waarde van het draaimoment van zware gaten beneden de nominale waarde valt van 3/2, als een gevolg van

de vermenging met lichte gaten. De polarisatie van de stroom vertoont een oscillerend gedrag met de put breedte W.

Het volgende hoofdstuk, hoofdstuk 4, behandelt spin-afhankelijke tunneling door drielagige structuren gemaakt van twee (Ga,Mn)As lagen, waar AlAs of GaAs optreedt als barrière. Zoals eerder vermeld kunnen deze drielagige structuren in de toekomst gebruikt worden als leeskoppen van harde schijven als de Curie temperatuur van (Ga,Mn)As boven kamertemperatuur gebracht kan worden. Zoals in vorige hoofdstuk, wordt de $\mathbf{k}\cdot\mathbf{p}$ theorie voor gaten gebruikt maar met inbegrip van de "Giant Zeeman Term". Dat is de gemiddeld-veld benadering van de p-d exchange integraal. Als referentie werden de experimentele gegevens van Higo en Tanaka van 2001, Ref. [132] gebruikt. Ze bereikten een magnetische tunnelweerstand (TMR) tot 75% in een drie lagen structuur gemaakt van twee (Ga,Mn)As lagen en een AlAs laag in een wigvorm om de TMR als functie van de barrière dikte D te kunnen meten. De theorie voorspeld een correcte grootteorde en een langzamere daling van de TMR in functie van de barrière dikte D in vergelijken met het experiment. Geen fitparameters zijn aanwezig in het model en alleen resonant tunnelen (coherent) werd in rekening is gebracht. De verklaring voor het verschil met het experiment kan zijn dat inelastische verstrooing verwaarloosd werd aan de tussenlakken (Ga,Mn)As/AlAs, mogelijk tunnelen door de defecttoestanden in de bandkloof, zoals de aanwezigheid van Mn atomen in de AlAs barrière als gevolg van inter-diffusie, etc. Verder is de interactie tussen de d elektronen en gaten banden benaderd door de gemiddeld veld benadering (mean field approximation) en is de verandering in toestandsdichtheid door de aanwezigheid van open d-schil verwaarloosd. Verder zal een meer gedetaileerd onderzoek de inelastische verstrooing aan tussenlakken in rekening moeten brengen door het toelaten van niet behoud van in-vlak momemtum conversie. Een fenomenologische parameter die de verstrooing karakteriseerd kon worden bepaald uit de experimentele data van GaAs/AlAs/GaAs structuren zonder de aanwezigheid van Mn atomen, dienend als controle staal. Op deze manier kon men een fitprocedure vermijden. Aan de andere kant kan men een meer gedetaileerde banden structuur in rekening brengen door het gebruiken van een "tight binding" model zoals $sp^3s^*d^5$.

In hoofdstuk 5 is de invloed van spanning op de TMR van drielagen structuren onderzocht. De structuur is (Ga,Mn)As/AlAs/(Ga,Mn)As maar nu gegroeid op InGaAs met een ingebouwde trekspanning ten gevolge van de roosterverschillen tussen GaAs en InGaAs. De trekspanning zorgt er voor dat de gemakkelijke as van magnetisatie georienteerd is in de groeirichting. Het blijkt dat de trekspanning de TMR verslechterd. Het effect is drievoudig: een verandering van gemakkelijke as, de verandering van het Fermi niveau door de herdistributie van gaten in de subbanden van zware en lichte gaten verschuiven op een tegengestelde manier. Bijvoorbeeld, de subbanden van lichte gaten zijn naar beneden opgeschoven waardoor ze minder gepolariseerd zijn. Zoals aangetoond in de vorige twee hoofdstukken dragen lichte gaten meer bij tot de stroom en de TMR. Dit verklaart de lagere waarde van de magneto-

weerstand verhouding van drielagen structuren gegroeid op InGaAs. Door het gebrek aan experimentele data met betrekking tot de gatendichtheid was het niet mogelijk om een theoretische geschatte waarde te bepalen voor de TMR van het betrokken staal. Eigenlijk, was de gatendichtheid gefit aan de experimentele waarde van de magneto-weerstand verhouding. Deze waarde is typische voor zulke stalen voor de beschouwde mangaan concentratie.

References

1. M. N. Baibich, J. M. Broto, A. Fert, F. Nguyen Van Dau, F. Petroff, P. Eitenne, G. Creuzet, A. Friederich, and J. Chazelas, Phys. Rev. Lett. **61**, 2472 (1988).

2. S. A. Wolf, D. D. Awschalom, R. A. Buhrman, J. M. Daughton, S. von Molnar, M. L. Roukes, A. Y. Chtchelkanova, and D. M. Treger, Science **294**, 1448 (2001).

3. S. Datta and B. Das, Appl. Phys. Lett. **56**, 665 (1990).

4. Kasuya, T. and A. Yanase, Rev. Mod. Phys. **40** 684, (1968).

5. Coey, J. M. D., M. Viret and S. von Molnr, Adv. Phys. **48**, 167 (1999).

6. Tokura, Y. and Y. Tomioka, J. Magn. Magn. Matter. **200**, 1 (1999).

7. M. Ilegems, R. Dingle, and L.W. Rupp (Jr.), Appl. Phys. **46**, 3059 (1975), D.G. Andrianov, V.V. Karataev, G.V. Lazarev, Yu.B. Muravlev, and A.S. Savel'ev, Sov. Phys. Semicond. **11**, 738 (1977), T. Hayashi, Y. Hashimoto, S. Katsumoto, and Y. Iye, Appl. Phys. Lett. **78**, 1691 (2001).

8. H. Munekata, H. Ohno, S. von Molnar, A. Segmller, L. L. Chang, and L. Esaki, Phys. Rev. Lett. **63**, 1849 (1989).

9. H. Ohno, H. Munekata, T. Penny, S. von Molnar, and L. L. Chang, Phys. Rev. Lett. **68**, 2664 (1992).

10. F. Matsukura, H. Ohno, A. Shen, and Y. Sugawara, Phys. Rev. B **57**, R2037 (1998).

11. H. Ohno, J. Magn. Magn. Mater. **200**, 110 (1999); Science **281**, 951 (1998).

12. K. Wang, R. Campion, K. Edmonds, M. Sawicki, T. Dietl, C. Foxon, and B. Gallagher, Proceedings of 27^{th} Conference on Physics of Semiconductors, Flagstaff, Arizona, USA **772**, 333 (2005).

13. V. A. Chitta, J. A. H. Coaquira, J. R. L. Fernandez, C. A. Duarte, J. R. Leite, D. Schikora, D. J. As, K. Lischka, and E. Abramof, Appl. Phys. Lett. **85**, 3777, (2004).

14. S. Sonoda, S. Shimizu, T. Sasaki, Y. Yamamoto, and H. Hori, J. Appl. Phys. **91**, 7911 (2002).

15. M. L. Reed, N. A. El-Masry, H. H. Stadelmaier, M. K. Ritums, M. J. Reed, C. A. Parker, J. C. Roberts, and S. M. Bedair, Appl. Phys. Lett. **79**, 3473 (2001). N. Theodoropolou, A. F. Hebard, M. E. Overberg, S. N. G. Chu, and R. G. Wilson, Appl. Phys. Lett. **78**, 3475 (2001); M. E. Overberg, C. R. Abernathy, S. J. Pearton, N. A. Theodoropoulou, K. T. McCarthy, and A. F. Hebard, Appl. Phys. Lett. **79**, 1312 (2001).

16. Schmidt J. Phys. D: Appl. Phys. **38** (2005).

17. J. Mašek, J. Kudrnovksý, and F. Máca, Phys. Rev. B **67**, 153203 (2003).

18. K. M. Yu, W. Walukiewicz, T. Wojtowicz, I. Kuryliszyn, X. Liu, Y. Sasaki, and J. K. Furdyna, Phys. Rev. B **65**, 201303 (2002).

19. A. Van Esch, L. Van Bockstal, J. De Boeck, G. Verbanck, A. S. van Steenbergen, P. J. Wellmann, B. Grietens, R. Bogaerts, F. Herlach, and G. Borghs, Phys. Rev. B **56**, 13103 (1997).

20. K. C. Ku, S. J. Potashnik, R. F. Wang, S. H. Chun, P. Schiffer, and N. Samarth, M. J. Seong and A. Mascarenhas, E. Johnston-Halperin, R. C. Myers, A. C. Gossard, and D. D. Awschalom Appl. Phys. Lett. **82**, 2302 (2003).

21. J. M. Langer, C. Delerue, M. Lannoo, and H. Heinrich Phys. Rev. B **38** 7723 (1988).

22. T. Dietl, Semicond. Sci. Technol. **17** 377 (2002).

23. Z̈utić, J. Fabian and S. Das Sarma, Rev. Mod. Phys. **76**, 323 (2004).

24. T. Kasuya and A. Yanase, Rev. Mod. Phys. **40**, 684 (1968).

25. R. A. Chapman and W. G. Hutchinson, Phys. Rev. Lett. **18**, 443 (1967).

26. M. Malfait, *Magnetic and transport properties of $Ga_{1-x}Mn_xAs$ diluted magnetic semiconductors* Ph.D. thesis, Katholieke Universiteit Leuven (2005).

27. J. Schneider, U. Kaufmann, W. Wilkening, M. Baeumler, and F. Köhl, Phys. Rev. Lett. **59**, 240 (1987).

28. T. Weiers, Phys. Rev. B **73**, 033201 (2006).

29. M. Linnarsson, E. Janzen, and B. Monemar, M. Kleverman, and A. Thilderkvist, Phys. Rev. B **55**, 6938 (1997).

30. J. Szczytko, A. Twardowski, K. S wiatek, M. Palczewska, M. Tanaka T. Hayashi, and K. Ando, Phys. Rev. B **60**, 8304 (1999).

31. S. Sanvito, P. Ordejón, and N.A. Hill, Phys. Rev. B **63**, 165206 (2001).

32. T. Graf, M. Gjukic, L. Görgens, O. Ambacher, M. S. Brandt, and M. Stutzmann, Appl. Phys. Lett. **81**, 5159 (2002).

33. A. Woos, M. Palczewska, M. Zajac, J. Gosk, M. Kaminska, A. Twardowski, M. Bockowski, I. Grzegory, and S. Porowski, Phys. Rev. B **69**, 115210 (2004).

34. A. Titov, X. Biquard, D. Halley, S. Kuroda, E. Bellet-Amalric, H. Mariette, J. Cibert, A. E. Merad, G. Merad, M. B. Kanoun, E. Kulatov, and Yu. A. Uspenskii, Phys. Rev. B **72**, 115209 (2005).

35. M. Zając, R. Doradziński, J. Gosk, J. Szczytko, M. Lefeld-Sosnowska, M. Kamińska, and A. Twardowski, M. Palczewska, E. Grzanka, W. Gębicki, Appl. Phys. **78**, 1276 (2005).

36. P. M. Tedrow and R. Meservey, Phys. Rev. Lett. **26**, 192 (1971).

37. P. M. Tedrow and R. Meservey, Phys. Rev. B **7**, 318 (1971).

38. S. A. Wolf, D. D. Awschalom, R. A. Buhrman, J. M. Daughton, S. von Molnar, M. L. Roukes, A. Y. Chtchelkanova, and D. M. Treger, Science **294**, 1448 (2001).

39. J. M. Kikkawa and D. D. Awschalom, Phys. Rev. Lett. **80**, 4313 (1998).

40. J. M. Kikkawa and D. D. Awschalom, Phys. Rev. Lett. **80**, 4313 (1998).

41. M. Roukes, Nature (London) **411**, 747 (2001).

42. R. Fiederling, Nature (London) **402**, 787 (2000).

43. I. Malajovich, J. J. Berry, N. Samarth and D. D. Awschalom, Nature (London) **411**, 770 (2001).

44. I. Malajovich, J. M. Kikkawa, D. D. Awschalom, J. J. Berry, and N. Samarth, Phys. Rev. Lett. **84**, 1015 (2000).

45. E. Johnston-Halperin, D. Lofgreen, R. K. Kawakami, D. K. Young, L. Coldren, A. C. Gossard, and D. D. Awschalom, Phys. Rev B **65**, 041306 (2002).

46. S. E. Andresen, B. S. Sorensen, F. B. Rasmussen, P. E. Lindelof, J. Sadowski, C. M. Guertler, and J. A. C. Bland, J. Appl. Phys. **94**, 1015 (2000).

47. H. Holmberg, N. Lebedeva, S. Novikov, J. Ikonen, P. Kuivalainen, M. Malfait, and V. V. Moshchalkov, Europhys. Lett. **71**, 811 (2005)

48. Y. Satoh, D. Okazawa, A. Nagashima, and J. Yoshino, Physica E **10**, 196 (2001).

49. N. Theodoropoulou, A. F. Hebard, M. E. Overberg, C. R. Abernathy, and S. J. Pearton, S. N. G. Chu, R. G. Wilson, Phys. Rev. Lett. **89**, 107203 (2002).

50. D. J. Priour, Jr., E. H. Hwang, and S. Das Sarma, Phys. Rev. Lett. **92**, 117201 (2004).

51. P. Krstajić and F. M. Peeters, V. A. Ivanov, V. Fleurov, and K. Kikoin Phys. Rev. B **70**, 195215 (2004).

52. T. Dietl, H. Ohno, and F. Matsukura, Phys. Rev. B **63**, 195205 (2001).

53. S. Hilbert and W. Nolting, Phys. Rev. B **71**, 113204 (2005).

54. T. Jungwirth, J. Maŝek, J. Sinova, and A. H. MacDonald, Phys. Rev. B **68**, 161202 (2003).

55. R. Bouzerar, G. Bouzerar and T. Ziman, Phys. Rev. B **73**, 024411 (2006).

56. W. Heisenberg, Z. Phys. **49**, 613 (1928).

57. S. Hilbert and W. Nolting, Phys. Rev. B **70**, 165203 (2004).

58. K. Sato, W. Schweika, P. H. Dederichs, and H. Katayama-Yoshida, Phys. Rev. B **70**, 201202 (2005).

59. L. Brey and G. Gomez-Santos, Phys. Rev. B **68**, 115205 (2003).

60. N. W. Ashcroft and N. D. Mermin, *Solid State Physics* (Brooks Cole, 1976).

61. T. Jungwirth, W. A. Atkinson, B. H. Lee, and A. H. MacDonald, Phys. Rev. B **59**, 9818 (1999).

62. T. Jungwirth, Jürgen König, Jairo Sinova, J. Kuĉera, and A. H. MacDonald, Phys. Rev. B **66**, 012402 (2002).

63. T. Jungwirth, K. Y. Wang, J. Maek, K. W. Edmonds, Jrgen Knig, Jairo Sinova, M. Polini, N. A. Goncharuk, A. H. MacDonald, M. Sawicki, A. W. Rushforth, R. P. Campion, L. X. Zhao, C. T. Foxon, and B. L. Gallagher Phys. Rev. B **72**, 165204 (2005).

64. C. Zener, Phys. Rev. **81**, 440 (1950).

65. C. Zener, Phys. Rev. **83**, 299 (1951).

66. K. A. Kikoin and V. N. Fleurov, *"Transition Metal Impurities in Semiconductors",* (World Scientific, Singapore, 1994).

67. J. Schneider, U. Kaufmann, W. Wilkening, M. Baeumler, and F. Köhl, Phys. Rev. Lett. **59**, 240 (1987).

68. M. Linnarsson, E. Janzen, B. Monemar, M. Kleverman, and A. Thilderkvist, Phys. Rev. B **55**, 6938 (1997).

69. J. Szczytko, A. Twardowski, K. Swiatek, M. Palczewska, M. Tanaka, and T. Hayashi, and K. Ando, Phys. Rev. B **60**, 8304 (1999).

70. Y. Nagai, T. Kunimoto, K. Nagasaka, H. Nojiri, M. Motokawa, F. Matsukura, T. Dietl, and H. Ohno, Jpn. J. Appl. Phys. **40**, 6231 (2001).

71. A. Zunger, in *Solid State Physics,* Eds. H. Ehrenreich and D. Turnbull (Academic, Orlando, 1986) Vol. **39**, p. 276.

72. K. A. Kikoin and V. N. Fleurov, J. Phys. C: Solid State Phys. **10**, 4295 (1977).

73. E. U. Condon and G. H. Shortley, *The Theory of Atomic Spectra* (Cambridge University Press, Cambridge, 1967).

74. L. A. Hemstreet, Phys. Rev. B **22**, 4590 (1980).

75. G. Picoli, A. Chomette, and M. Lannoo, Phys. Rev. B **30**, 7138 (1984).

76. V. A. Singh and A. Zunger, Phys. Rev. B **31**, 3729 (1985).

77. V. N. Fleurov and K. A. Kikoin, J. Phys. C: Solid State Phys. **19**, 887 (1986).

78. K. A. Kikoin and V. N. Fleurov, J. Phys. C: Solid State Phys. **17**, 2357 (1984).

79. K. Sato and H. Katayama-Yoshida, Jpn. J. Appl. Phys. **40**, L485 (2001); L. Kronik, M. Jain, and J. R. Chelikowsky, Phys. Rev. B **66**, 041203(R) (2002); M. van Schilfgaarde and O. N. Mryasov, Phys. Rev. B **63**, 233205 (2001); E. Kulatov, H. Nakayama, H. Mariette, H. Ohta, and Y. A. Uspenskii, Phys. Rev. B **66**, 045203 (2002).

80. P. W. Anderson, Phys. Rev. **124**, 41 (1961).

81. V. N. Fleurov and K. A. Kikoin, J. Phys. C: Solid State Phys. **9**, 1673 (1976).

82. F. D. M. Haldane and P. W. Anderson, Phys. Rev. B **13**, 2553 (1976).

83. S. Alexander and P. W. Anderson, Phys. Rev. **133**, A1594 (1964).

84. K. A. Kikoin and V. N. Fleurov, Zh. Ekps. Teor. Fiz. **77**, 1062 (1979) [JETP **50**, 535 (1979)].

85. *Data in Science and Technology - Semiconductors: Group IV Elements and III-V Compounds,* edited by O. Madelung (Springer-Verlag, Berlin, 1991).

86. F. Matsukura, H. Ohno, T. Dietl, *III-V Ferromagnetic Semiconductors* in: Handbook of Magnetic Materials **14**, 1, edited by K.H.J. Buschow (Elsevier, Amsterdam, 2002)

87. C. Zener, Phys. Rev. **82**, 403 (1951).

88. K. W. Edmonds, K. Y. Wang, R. P. Campion, A. C. Neumann, C. T. Foxon, B. L. Gallagher, and P. C. Main, Appl. Phys. Lett. **81**, 3010 (2002).

89. K. W. Edmonds, K. Y. Wang, R. P. Campion, A. C. Neumann, N. R. S. Farley, B. L. Gallagher, and C. T. Foxon, Appl. Phys. Lett. **81**, 4991 (2002).

90. H. Asklund, L. Ilver, J. Kanski, J. Sadowski, and R. Mathieu, Phys. Rev. B **66**, 115319 (2002).

91. N. Theodoropoulou, A. F. Hebard, M. E. Overberg, C. R. Abernathy, S. J. Pearton, S. N. G. Chu, and R. G. Wilson, Phys. Rev. Lett. **89**, 107203 (2002).

92. I. Ya. Korenblit and E. F. Shender, Zh. Exp. Teor. Fiz. **62**, 1949 (1972) [Sov. Phys. - JETP **35**, 1017]; S. L. Ginzburg, I. Ya. Korenblit, I. Y. Shender, Zh. Exp. Teor. Fiz. **64**, 2255 (1973) [Sov. Phys. JETP **37**, 1141].

93. I. Ya. Korenblit and E.F. Shender, Usp. Fiz. Nauk **126**, 233 (1978) [Sov. Phys. - Uspekhi **21**, 832 (1978)].

94. I. Ya. Korenblit, E. F. Shender, and B. I. Shklovskii, Phys. Lett. **46**A, 275 (1973).

95. M. J. Reed, F. E. Arkun, E. A. Berkman, and N. A. Elmasry, J. Zavada, M. O. Luen, M. L. Reed, and S. M. Bedaira Appl. Phys. Lett. **86**, 102504 (2005).

96. P. W. Anderson, Phys. Rev. **79**, 350 (1950); J. B. Goodenough, *Magnetism and Chemical Bond* (Interscience Publ., N. Y., 1963).

97. T. Jungwirth, W. A. Atkinson, B. H. Lee, and A. H. MacDonald, Phys. Rev. B **59**, 9818 (1999).

98. T. Dietl, H. Ohno, F. Matsukura, J. Cibert, and D. Ferrand, Science **287**, 139 (1998).

99. S. V. Vonsovskii, Zh. Exp. Teor. Fiz. **16**, 981 (1946).

100. A.A. Abrikosov and L.P. Gorkov, Zh. Eksp. Teor. Fiz. **43**, 2230 (1962) [Sov. Phys. - JETP, **16**, 1575 (1963)].

101. M. Abolfath, T. Jungwirth, J. Brum, and A. MacDonald, Phys. Rev. B **63**, 054418 (2001).

102. W. Shockley, Phys. Rev. **78**, 173 (1950).

103. E. O. Kane, J. Phys. Chem. Solids **1**, 249 (1957).

104. J. M. Luttinger and W. Kohn, Phys. Rev. **97**, 869 (1955).

105. J. M. Luttinger, Phys. Rev. **102**, 1030 (1956).

106. W. Tom Wenckebach, *Essential of Semiconductor Physics* (John Willey & Sons, Toronto, 1999).

107. I. Vurgaftman and J. R. Meyer, Phys. Rev. B **67**, 125209 (2003).

108. R. Wessel and M. Altarelli, Phys. Rev. B **39**, 12802 (1989).

109. E. T. Yu, M. K. Jackson, and T. C. McGill, Appl. Phys. Lett. **55**, 744 (1989).

110. J.-B. Xia, Phys. Rev. B **38**, 8365 (1998).

111. D. Z. -Y. Ting, E. T. Yu, and T. C. McGill, Phys. Rev. B **45**, 3583 (1992).

112. A. Zaslavsky, D. C. Tsui, M. Santos, and M. Shayegan, Phys. Rev. B **40**, 9829 (1989).

113. Y. X. Liu, D. Z. -Y. Ting, and T. C. McGill, Phys. Rev. B **54**, 5675 (1996).

114. G. Y. Wu, K. -M. Hung, and C. -J. Chen, Phys. Rev. B **46**, 1521 (1992).

115. T. -J. Chow, G. Y. Wu, K. -M. Hung, and C. -W. Chen, Phys. Rev. B **55**, 1329 (1997).

116. J.-X. Zhu, Z. D. Wang, and C.-D. Gong, Solid State Comm. **101**, 257 (1997).

117. A. C. Rodrigues Bittencourt, A. M. Cohen, and G. E. Marques, Phys. Rev B **57**, 4525 (1998).

118. G. Bastard, *Wave Mechanics Applied to Semiconductor Heterostructures*, (Les Editions de Physique, Les Ulis, Paris, 1987), p. 45.

119. L. C. Andreani, A. Pasquarello, and F. Bassani, Phys. Rev. B **36**, 5887 (1987).

120. C. Y. Chao and S. L. Chuang, Phys. Rev B **43**, 7027 (1991).

121. W. R. Frensley, Rev. Mod. Phys. B **62**, 745 (1990).

122. F. Sheid, *Numerical Analysis*, (Shaum's Outline Series, McGraw-Hill, New York, 1968), p. 194.

123. M. K. Jackson, M. B. Johnson, D. H. Chow, T. C. McGill, and C. W. Nieh, Appl. Phys. Lett. **54**, 552 (1989).

124. L. D. Landau and E. M. Lifshitz, *Quantum Mechanics*, (Pergamon Press, Oxford, 1977), p. 456.

125. A. G. Petukhov, D. O. Demchenko, and A. N. Chantis, Phys. Rev. B **68**, 125332 (2003); A. G. Petukhov, W. R. L. Lambrecht, and B. Segall, Phys. Rev. B **53**, 3646 (1996).

126. R. Ferreira and G. Bastard, Phys. Rev. B **43**, 9687 (1991).

127. Shiow-Fon Tsay, Jih-Chen Chiang, Z. M. Chau, and Ikai Lo, Phys. Rev B **56**, 13242 (1997).

128. G. Goldoni and A. Fasolino, Phys. Rev. B, **48**, 4948 (1993).

129. G. Edwards, E. C. Valadares, and F. W. Sheard, Phys. Rev. B, **50**, 8493 (1994).

130. Dietl and Y. Ohno, Phys. Rev. B **37**, 026602 (2002).

131. D. Chiba, F. Matsukura, and H. Ohno, Physica E **21**, 966 (2004).

132. M. Tanaka and Y. Higo, Phys. Rev. Lett. **87**, 026602 (2001).

133. Y. Higo, H. Shimizu, and M. Tanaka, Phys. Rev. B **89**, 6745 (2001).

134. R. Mattana, M. Elsen, J. -M. George, H. Jaffrès, F. Nguyen Van Dau, A. Fert, M. F. Wyczisk, J. Olivier, P. Galtier, B. Lépine, A. Guivarc'h, and G. Jézéquel, Phys. Rev. B **71**, 075206 (2005).

135. S. S. Maklera, M. A. Bosellia, J. Weberszpil, X. F. Wanga, and I. C. da Cunha Lima, Physica B **320**, 396 (2002); S. S. Maklera, M. A. Bosellia, J. Weberszpil, X. F. Wanga, and I.C. da Cunha Lima, Physica B **354**, 348 (2004).

136. A. G. Petukhov, A. N. Chantis, and D. O. Demchenko, Phys. Rev. Lett. **89**, 107205 (2002).

137. A. G. Petukhov, D. O. Demchenko, and A. N. Chantis, Phys. Rev. B **68**, 125332 (2003).

138. S. C. P. Rodrigues, L. M. R. Scolfaro, J. R. Leite, and I. C. da Cunha Lima, G. M. Sipahi, and M. A. Boselli, Phys. Rev. B **70**, 165308 (2004).

139. N. Malkova and U. Ekenberg, Phys. Rev. B **66**, 155324 (2002).

140. P. Krstajić and F. Peeters, Phys. Rev. B **71**, 115321 (2005).

141. T. Dietl, A. Haury, and Y. M. d'Aubigne, Phys. Rev. B **55**, R3347 (1997).

142. T. Dietl, J. Phys: Cond. Matt. **16**, S5471 (2004).

143. Y. Ohno, I. Arata, F. Matsukura, and H. Ohno, Physica **13**, 521 (2002).

144. D. Chiba, N. Akiba, F. Matsukura, Y. Ohno, and H. Ohno, Appl. Phys. Lett. **77**, 1873 (2000).

145. H. Ohno, F. Matsukura, and Y. Ohno, Solid State Commun. **119**, 281 (2001).

146. P. Krstajić and F. M. Peeters, Phys. Rev. B **72**, 125350 (2005).

147. S. Ohya, P. N. Hai, and M. Tanaka, Appl. Phys. Lett. **87**, 012105 (2005).

148. I. Vurgaftman, J. R. Meyer, and L. R. Ram-Mohan, Appl. Phys. Lett. **89**, 5815 (2001).

149. L. D. Landau and E. M. Lifshitz, *Theory of elasticity* (Butterworth-Heinemann Ltd, Oxford, 1995).

150. A. E. H. Love, *A treatise on the mathematical theory of elasticity* (Dover publications, New York, 1944).

151. G. L. Bir and G. E. Pikus, *Symmetry and Strain-Induced Effects in Semiconductors* (Wiley, New York, 1974).

152. C. Yi-P Chao and S. L. Chuang, Phys. Rev. B **46**, 4110 (1992).

153. N. N. Beletskii, G. P. Berman, and S. A. Borysenko, Phys. Rev. B **71**, 125321 (2005).

154. J. Yang, J. Wang, Z. M. Zheng, D. Y. Xing, and C. R. Chang, Phys. Rev. B **71**, 214434 (2005).

155. H. Ohno, N. Akiba, F. Matsukura, A. Shen, K. Ohtani, and Y. Ohno, Appl. Phys. Lett. **73** 363 (1998).

156. F. Matsukura, H. Ohno, A. Shen, and Y. Sugawara, Phys. Rev. B **57**, R2037 (1998).

157. C. Rüster, C. Gould, T. Jungwirth, J. Sinova, G. M. Schott, R. Giraud, K. Brunner, G. Schmidt, and L. W. Molenkamp, Phys. Rev. Lett. **94**, 027203 (2005).

158. C. Gould, C. Rüster, T. Jungwirth, E. Girgis, G. M. Schott, R. Giraud, K. Brunner, G. Schmidt, and L. W. Molenkamp Phys. Rev. Lett. **93**, 117203 (2004).

159. H. Saito, S. Yuasa, and K. Ando, Phys. Rev. Lett. **95**, 086604 (2005).

160. B. Caroli, J. Phys. Chem. Solids **28**, 1427 (1967).

9

Curriculum Vitae

Predrag Krstajić
born on January 7, 1976, Belgrade, Serbia and Montenegro

- 1990-1994 Mathematical High School, Belgrade.
- 1998 Summer Undergraduate Research Fellowships (SURF), conducted at Jet Propulsion Laboratory (NASA), California Institute of Technology, United States of America.
- 1994-2000 Studies at the University of Belgrade, School of Electrical Engineering, Department for Physical Electronics (former Technical Physics) Micro- and Optoelectronics and Laser Technics. Diploma thesis: *"Numerical simulation of non-linear response of a PIN photodiode"* under supervision of Prof. dr. Zoran Djurić and Prof. dr. Miloljub Smiljanić.
- 2000-2001 Institute of Chemistry, Technology and Metallurgy, Belgrade, Serbia and Montenegro as a research assistant.
- 2001-2006 Ph.D. studies at the University of Antwerp, Antwerp, Department of Physics under supervision of Prof. dr. François M. Peeters. Ph.D. thesis: *"Magnetism and tunneling in diluted magnetic semiconductor structures".*

List of publications

1. P. M. Krstajić, V. A. Ivanov, F. M. Peeters, V. Fleurov, K. Kikoin *Ferromagnetism in Mn-doped GaAs: The Kinematic Exchange*, Journal of Superconductivity **16**, 111 (2003) (3 pages).

2. P. M. Krstajić, F. M. Peeters, V. A. Ivanov, V. Fleurov, and K. Kikoin, *Double-exchange mechanisms for Mn-doped III-V ferromagnetic semiconductors*, Phys. Rev. B **70**, 195215 (2004) (16 pages).

3. P. M. Krstajić, V. A. Ivanov, F. M. Peeters, V. Fleurov, and K. Kikoin, *On the nature of ferromagnetic exchange in Dilute Magnetic Semiconductors: GaAs:Mn*, Europhys. Lett. **61**, 235 (2003) (7 pages).

4. V. A. Ivanov, P. M. Krstajić, F. M. Peeters, V. Fleurov, K. Kikoin, *On the ferromagnetic exchange in Mn-doped IIIV semiconductors*, Physica B **329**, 1282 (2003) (2 pages).

5. V. A. Ivanov, P. M. Krstajić, F. M. Peeters, V. Fleurov and K. Kikoin *On the Nature of Ferromagnetism in Dilute Magnetic Semiconductors: GaAs:Mn and GaP:Mn* Journal of Magnetism and Magnetic Materials **258**, 237 (2003) (4 pages).

6. P. Krstajić and F. M. Peeters, *Magnetotunneling of holes through single and double barriers using a multiband treatment*, Phys. Rev. B **71**, 115321 (2005) (10 pages).

7. P. Krstajić and F. M. Peeters, *Spin-dependent tunneling in diluted magnetic semiconductor trilayer structures*, Phys. Rev. B **72**, 125350 (2005) (10 pages).

8. P. Krstajić and F. M. Peeters, *Influence of strain on the tunneling magnetoresistance in diluted magnetic semiconductor trilayer and double barrier structures*, submitted to Phys. Rev. B.